Space and Time Resolved Spectroscopy During the Preparation of Hydrogenation Catalyst Bodies

Plaats- en Tijdsafhankelijke Spectroscopie Tijdens de Bereiding van Hydrogeneringskatalysatoren

(met een samenvatting in het Nederlands)

Proefschrift

ter verkrijging van de graad van doctor aan de Universiteit Utrecht
op gezag van de rector magnificus, prof. dr. J. C. Stoof,
ingevolge het besluit van het college voor promoties in het openbaar te verdedigen
op maandag 16 november 2009 des ochtends te 10.30 uur

door

Leticia Espinosa Alonso

geboren op 3 november 1981 te León, Spanje

Promotoren: Prof. dr. ir. B. M. Weckhuysen

Prof. dr. ir. K. P. de Jong

Co-promotor: Dr. A. M. Beale

This thesis was accomplished with financial support from ACTS/ASPECT.

“Aim for the moon. If you miss, you may hit the stars”

W. Clement Stone

ISBN: 978-90-393-5209-0

Printed by Ipskamp Drukkers

Contents

Chapter 1

General Introduction

Supported Metal Catalysts and Their Preparation

A catalytic solid is a material that facilitates a chemical reaction by lowering the activation barrier.[1] It is comprised of a support and the catalytically active phase. The support is a porous solid, such as TiO_2, Al_2O_3, SiO_2 or carbon, usually with a high specific surface area that enables a high dispersion of the active phase at high loadings with unique phase-support interactions that result in the required catalytic efficiency (activity, selectivity and stability). Some examples of active phases include Ni, Pd or Pt, which are typically used in (de-)hydrogenation reactions; Co or Fe common in Fischer-Tropsch catalysis; and Mo involved in hydroprocessing treatments.[2-6]

A large number of industrial catalysts are supported metal (oxide) catalysts that require a high dispersion of the active component. Hence, they must be efficient and stable, but they also require other properties such as being regenerable, mechanically strong and cost effective. In order to achieve high mechanical stability, the support must be pre-shaped into support bodies with sizes from tens of micrometers to millimeters. The shape and the size of these support bodies then depend on the specific application of the catalyst and the type of reactor in which they will be loaded. In this way, spheres in the 20-100 μm range are generally used in fluid bed reactors; whilst other larger bodies, such as rings, beads, pellets or extrudates of millimeter sizes, are used in fixed bed reactors. These larger bodies enable the pressure drop through the bed to be low.[4] Other interesting commercial shapes are trilobes or quadrulobes, which minimize the mass-transfer limitations of the reactants through the catalyst bodies.

The classical preparation method of industrial catalysts includes pore volume impregnation and drying followed by a thermal treatment. In some cases, an additional activation step is required, such as reduction or sulphidation, to arrive at the active catalytic material. In this manner, an impregnation solution that contains the precursor of the active species is contacted with the support. The amount of solution used is just enough to fill the pores of the support and, thus, is equal to its pore volume. During the pore volume impregnation, three phenomena occur: capillary flow of the solution towards the core of the catalyst body, diffusion of the metal-ion in the liquid-solid interface and adsorption of these ions in the pore walls. [7, 8] As a result, depending on the relative importance of each phenomenon, different macro-distributions of the active species along the catalyst bodies can be obtained after impregnation, that can be modified during drying or thermal treatment. For instance, if the adsorption of the precursor of the active component at the support surface is strong, then, it will be retained in the outer rim of the catalyst body; whilst if it is weak, the precursor will be spread out within the body. The first case yields a macro-distribution of the active material generally known as egg-shell, while the latter yields a uniform macro-distribution. There are two other defined macro-distributions known as egg-yolk (the active component concentrated in the core of the body) and egg-white (the active component is enriched in a concentric ring in the body). In order to create these two profiles, competitive adsorption of ions play a role.[8, 9] Figure 1.1 illustrates the four types of macro-distributions of the active phase within cylindrical catalyst bodies.

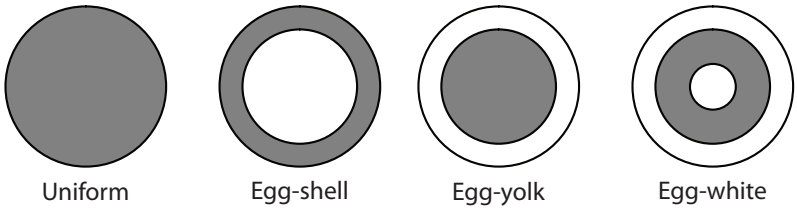

Figure 1.1. Different macro-distributions of the active phase within mm-sized catalyst bodies. The grey color corresponds to the active phase and the white color represents the support.

It is important to realize that a uniform macro-distribution of the active sites is often but not always the optimum catalyst. Each of the above-mentioned macro-distributions has its own applications, which are generally determined by, among others, the reaction kinetics and catalyst poisoning. Uniform macro-distributions are employed if there are no diffusional restrictions, whilst egg-shell profiles are more favorable in the case of fast reactions; i.e. if there are diffusional restrictions.[10] On the other hand, egg-yolk distributions are desired if the external part of the catalyst is exposed to attrition and/ or poisoning, and egg-white can be utilized if the catalyst core suffers diffusional restrictions and the outer rim suffers attrition and/ or poisoning.[11, 12]

Furthermore, the macro-distributions created during the impregnation step might be modified by any of the subsequent preparation steps. The redistribution of the active component during the drying step has been studied both experimentally and theoretically by several groups.[8, 9, 13-16] The general consensus is that if no physicochemical interactions between the active component and the support surface take place during the impregnation step, then redistribution of the active species occurs unless drying is fast enough to avoid it. Thus, redistribution can be avoided if strong interactions between the precursor metal-ion complex and the support surface take place during impregnation. An alternative approach to avoid redistribution during drying is by increasing the viscosity of the impregnation solution for example using aqueous solutions of chelated metal complexes.[17]

The calcination step, additionally, might not only lead to redistribution of the active component within the catalyst bodies, but also to the formation of low dispersions of the active phase and/ or formation of solid solutions with the oxidic support material. As an example, Sietsma *et al*.[18] have reported that the calcination in air of 20 wt% Ni/SiO_2 catalysts, where Ni is impregnated as an aqueous solution of $Ni(NO_3)_2$, leads to sintering and redistribution of the Ni precursor and low NiO dispersions, whilst in the presence of H_2 the dispersion of NiO particles increases substantially. Nitrate salts are widely used as metal-ion precursors due to their beneficial properties such as high solubility allowing high metal loadings and low price. However, they are also known to give rise to low dispersions and solid solutions, e.g. as Ni aluminates if Al_2O_3 is chosen as the support material.[19] As a result, a compromise should be reached between all the experimental parameters (precursor salts and preparation conditions) in order to obtain the optimum catalyst. Hence, since there are a large number of parameters that affect the final macro-

distribution of the active component and its dispersion within support bodies, control on the preparation method is of utmost importance for the rational design of industrial catalysts.

Role of the Metal-Support Interface in the Preparation of Industrial Catalysts

The final macro-distribution and dispersion of the active component in a catalyst body are affected by the interactions that take place between the metal-ion precursor and the support surface already during the impregnation step and thus, are determined by the metal-support interface. A number of research groups have therefore implemented the question: "what is the role of the liquid-solid interface in the preparation of supported catalysts?".[20-24]

As a first approach, one can think of the adsorption model proposed by Brunelle in 1978,[23] known as the *double layer model*. He described that the surface of metal oxides become charged in the presence of an aqueous solution. In this way, the hydroxylic surface of a support may become positively charged in the presence of an acid solution, or negatively charged in the presence of a basic solution. Thus, a layer of counterions appears, known as the diffuse layer, next to the charged surface layer:

$$Al_s\text{-}OH + H^+ A^- \longrightarrow Al_s\text{-}OH^+A^- \quad (1)$$

$$Al_s\text{-}OH + B^+OH^- \longrightarrow Al\text{-}O^-B^+ + H_2O \quad (2)$$

Al_s-OH refers to hydroxyl groups from the support surface, $H^+ A^-$ represents an acid, and B^+OH^- a base. The point of zero charge, pzc, is then defined as the pH at which the surface net charge is zero.

This model serves as a first approximation to understand the interactions as electrostatic interactions between metal-ion complexes and the support surface. However, in reality the support oxide surfaces contain more than one type of adsorption sites, and each of these has its role on the adsorption of metal-ion complexes. For example, it has been reported that the γ-Al_2O_3 surface contains up to nine different types of hydroxyl groups with different acid-base properties and, hence, different reactivity.[25] For this reason, more detailed and specific models have

been developed that take into account the presence of different types of adsorption sites on the support surfaces and describe in a better way the adsorption of the precursors on the support surface. Lycourgiotis *et al.*[22] presented a few years ago a review containing a compilation the solid-liquid interface models developed until now. These comprise usually more than two charged layers and more specific interactions between the species involved; i.e., not only electrostatic interactions.

Since the support surface contains different types of hydroxyl groups with different acid-base properties the adsorption of the metal-ion precursor complexes on the support surface is governed by several parameters. These parameters include the pzc of the support oxide, the pH or ionic strength of the solution containing the precursor complex and the nature of this complex. Therefore, the adsorptive properties of the precursor complex on the support surface can be modified by tuning these factors by, for example, chemically modifying the support surface in order to change its pzc; or by modifying the chemical properties of the impregnation solution. This can be done by changing the solution pH or changing the nature of the metal-ion complex; i.e., modifying the 1st coordination sphere of the complex by using ligands different from water.[26-30] A scheme of the interactions involved in the adsorption of a precursor metal-ion complex on the γ-Al_2O_3 surface is represented in Figure 1.2 where Me refers to the metal, while L and n stands for the ligand and the metal-ion (complex) charge, respectively.

Several research groups have been studying the use of chelating ligands to change the nature of the precursor metal-ion complex in the preparation of supported metal (oxide) catalysts. Seminal examples include the work of Che and co-workers on the uses of Ni-ethylenediamine (*en*) complexes as precursors for the preparation of Ni catalysts.[31-36] They found that *en* increases the Ni dispersion and reducibility if the thermal treatment is carried out in an inert gas atmosphere. Similarly, Ryczkowski has reported that the use of ethylenediaminetetraacetic acid (*edta*) in the preparation of Ni/γ-Al_2O_3 catalysts increases the dispersion of Ni.[37] Other chelating agents that have been used for the preparation of supported metal (oxide) catalysts include acetylacetonate (*acac*), citric acid (*ca*) or nitrilotriacetic acid (*nta*).[17, 38, 39]

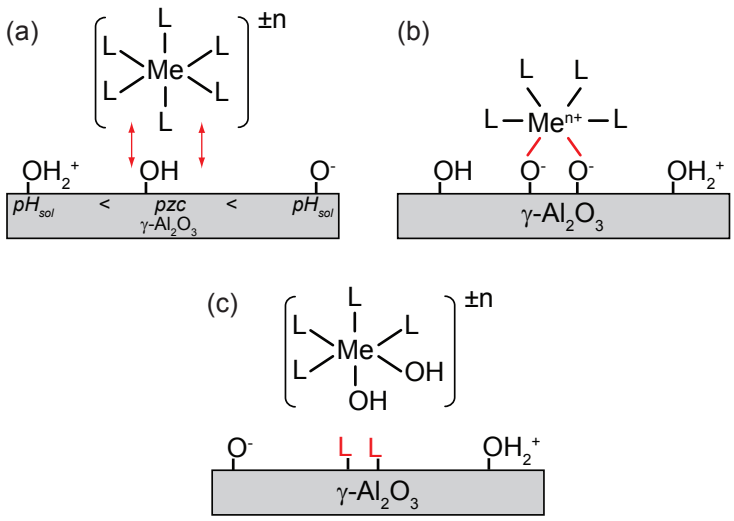

Figure 1.2. Representation of different interactions of a precursor metal-ion complex on a γ-Al_2O_3 surface. (a) Electrostatic interactions between the metal-ion complex and the support surface; (b) Grafting of the metal-ion complex on the support surface, where two oxygen atoms from the support surface enter the 1st coordination sphere of the metal-ion complex; (c) Grafting of the ligands L on the support surface and consequent hydrolysis of the metal-ion complex.

Space and Time Resolved Characterization of Catalyst Bodies

In order to achieve insight in the preparation of industrial catalysts it is of paramount importance to understand the physicochemical processes that the precursor of the active component undergoes during catalyst preparation. This knowledge can be obtained by applying spectroscopic characterization techniques. For a real characterization of the preparation of industrial mm-sized catalysts, the techniques employed must satisfy two requisites. Firstly, they must provide multidimensional information of the structure and composition of a catalyst body, since the size of this material lies in the millimeter range. Secondly, they must be applied in situ; i.e., during the preparation process of the catalyst. Hence, the development of space- and time- resolved spectroscopic methods is of high interest for researchers in the field of industrial catalysis and for the industrial community,

as it will underpin the rational design of industrial catalysts.[40, 41]

The space and time resolved characterization methods explored so far can be divided in two main groups: invasive and noninvasive. Invasive methods that give information on the molecular nature of the metal-ion species include Raman, UV-Vis-NIR and IR micro-spectroscopies. Raman micro-spectroscopy was firstly used by Knozinger and co-workers in 1993.[42] Since then, the experimental method for acquisition of space resolved spectra has become easier mainly due to instrumental developments; but still a prebisection of the samples under study is required in order to collect spatially resolved spectra at different positions along the cross section of the catalyst bodies. The experimental approach is presented in Figure 1.3.

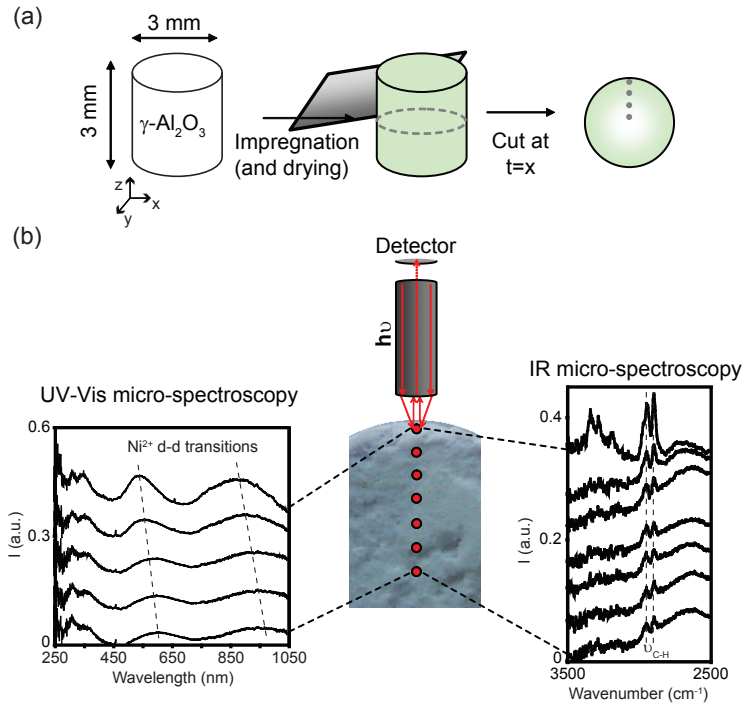

Figure 1.3. (a) Experimental approach that should be followed when invasive techniques are used to characterize impregnated or dried pellets. (b) Example of a bisected pellet together with the spatially resolved UV-Vis-NIR and IR spectra collected on the points of the surface indicated in red.

At different points in time 'x' after pore volume impregnation or after drying, the catalyst body is bisected perpendicular to its *z* axis by using a scalpel. Then, spatially resolved spectra can be measured on the resulting cross section of the catalyst body.

This figure illustrates examples of space resolved UV-Vis-NIR and IR spectra collected along a line scan of a dried catalyst body. The space resolved UV-Vis spectra show among others two Ni^{2+} d-d transition bands, which decrease in intensity and shift to longer wavelengths from the edge to the core of the catalyst body. Additionally, the space resolved IR spectra indicate an egg-shell distribution of the chelating agent *en* as deduced from the decrease in intensity of the C-H stretching vibrations at around 3000 cm^{-1} from the edge to the core of the catalyst body. Even though this illustration only shows examples of UV-Vis-NIR and IR micro-spectroscopies, the same principle is applied in the case of Raman micro-spectroscopy.

Both UV-Vis-NIR and Raman micro-spectroscopic methods can be used to monitor the dynamics of the metal-ion complex precursor after impregnation and during equilibration, and to visualize the molecular changes that this complex may undergo while is moving towards the core of the support body.[43, 44] In the case of UV-Vis-NIR micro-spectroscopy this can be done thanks to an environmental cell designed to keep a wet atmosphere around the bisected catalyst body during the measurements (Appendix A). If one wants to characterize dried and thermally-treated catalyst bodies, besides these two methodologies, IR micro-spectroscopy can also be applied, as illustrated in Figure 1.3.[45-47] Each of these techniques has its own advantages and the combination of the three provide complementary chemical information, which facilitates the understanding of the dynamics and the molecular changes that a metal-ion precursor complex and other ingredients of the impregnation solution undergo during catalyst preparation.

However, since the samples must be pre-bisected, the drying or thermal treatment steps cannot be studied in situ. This brings the desire of the catalyst scientist for the development of noninvasive methods that enable in situ characterization of all the steps involved in catalyst preparation. In this direction one can find techniques, such as Magnetic Resonance Imaging (MRI), which provides input in two dimensions (2D) and has been employed for instance to study the impregnation of different metal-ion precursor complexes or the drying of different support pellets.[48-50] Additionally, noninvasive synchrotron-based techniques, such as Tomographic Energy Dispersive Diffraction Imaging (TEDDI) and X-ray micro-tomography, are

being under investigation in the field of catalyst preparation. For example, TEDDI has been used to characterize in 3D the crystalline and amorphous structure of CoMo/γ-Al_2O_3 extrudates, whilst X-ray micro-tomography has been utilized to profile the structure of different support bodies.[51-53] Figure 1.4 illustrates the experimental approach to follow when the samples are characterized by noninvasive methods, such as MRI or TEDDI.

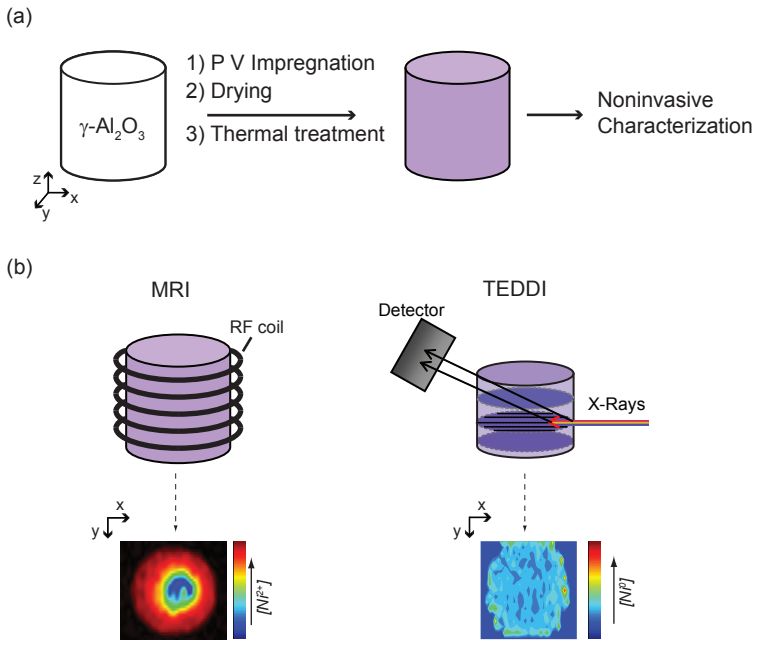

Figure 1.4. (a) Sample preparation to apply noninvasive characterization techniques during the impregnation, drying or thermal treatment steps of a catalyst body; (b) Characterization approach of the MRI and TEDDI techniques together with the typical images obtained from them.

^{1}H-MRI enables to obtain information regarding the dynamics of paramagnetic metal-ion complexes by making use of several magnetic field gradients and a radiofrequency (RF) coil. The MRI image shown in Figure 1.4 (b) represents an *xy* slice of a γ-Al_2O_3 extrudate 5 min after impregnation with a 0.5 M $Ni(H_2O)_6^{2+}$ solution. The red region indicates a high concentration of the complex, whilst the blue core indicates the presence of pure water. The second method, TEDDI, makes use of synchrotron light and by analyzing the diffraction and fluorescence signals recorded in the detector one can obtain information on the chemical distribution as well as on the phase changes taking place in a catalyst body. The TEDDI image in Figure 1.4 (b) represents a XY slice of a Ni/γ-Al_2O_3 pellet after thermal treatment in N_2. A green external ring can be observed, which indicates an egg-shell distribution of the metallic Ni (200) reflection at 57.6 keV.

Scope and Outline of the PhD Thesis

The aim of the research described in this PhD thesis is to obtain knowledge on the physicochemical processes involved during the preparation of catalyst bodies. Thus, the goal is to understand the changes in the molecular structure of the precursor metal-ion complex from the impregnation step until the catalytically active structure is formed, and how the final macro-distribution of the active component is created. For this purpose, the development and application of spatiotemporal spectroscopic techniques, that make it possible to monitor all the structural changes of the precursor metal-ion complex during the different preparation steps, is a must. The techniques that are described in this work comprise both invasive (UV-Vis-NIR and IR micro-spectroscopies) and noninvasive methods (MRI and TEDDI). Attention has been focused on the preparation of Pd and Ni on γ-Al_2O_3 hydrogenation catalyst bodies (pellets and extrudates). However, the analytical methods used in this research and the input obtained from their application can be extended to other catalyst bodies as well. In particular, the influence of various ingredients in the impregnation solution, such as chelating agents and inorganic salts, on the molecular structure and macro-distribution of the metal-ion during the different steps of catalyst preparation has been investigated.

Chapter 2 and Chapter 3 are related to the application of invasive micro-spectroscopic techniques. In **Chapter 2,** UV-Vis-NIR micro-spectroscopy is employed to study the influence of Cl^- (aq) on the formation of different Pd macro-distributions

on γ-Al_2O_3 pellets during the impregnation step. **Chapter 3** describes the use of UV-Vis-NIR and IR micro-spectroscopies to study the impregnation process of $[Ni(en)_x(H_2O)_{6-2x}]^{2+}$ (*en* = ethylenediamine and x = 0 - 3) on γ-Al_2O_3 bodies and reveals the creation of uniform or egg-shell Ni macro-distributions after drying.

Chapter 4 and Chapter 5 are related to the uses of noninvasive techniques to characterize the preparation of Ni/γ-Al_2O_3 catalyst bodies. **Chapter 4** describes the application of MRI to get quantitative and qualitative insight into the impregnation step of Ni^{2+} on γ-Al_2O_3 extrudates. ^{1}H-MRI is introduced as an indirect method to visualize in situ the dynamics of $[Ni(H_2O)_6]^{2+}$ in a quantitative manner by applying T_2-contrast imaging. This method is also used to monitor the transport of other complexes, such as $[Ni(edta)]^{2-}$ (*edta* = ethylenediaminetetraacetic acid), via T_1-contrast imaging. Finally, MRI in combination with UV-Vis-NIR micro-spectroscopy has been used to reveal the presence of electrostatic interactions between $[Ni(H_2O)_6]^{2+}$ and $[Ni(edta)]^{2-}$ when both complexes are co-impregnated. **Chapter 5** is dedicated to the application of TEDDI to monitor in situ the thermal treatment under N_2 of $[Ni(en)_3](NO_3)_2$ or $[Ni(en)(H_2O)_4]Cl_2$ /γ-Al_2O_3 bodies. This approach enables the in situ visualization of the genesis of the active metallic Ni structure in the support bodies, the decomposition of the $[Ni(en)_3](NO_3)_2$ and the formation of two intermediate crystalline phases during the thermal treatment of $[Ni(en)(H_2O)_4]Cl_2$.

Finally, Chapter 6 contains a summary with the main conclusions drawn from the previous chapters, and an outlook and some perspectives are presented in Chapter 7.

References

[1] G. Rothenberg, *Catalysis: Concepts and Green Applications*, Wiley-VCH, Weinheim, **2008**.

[2] *Synthesis of Solid Catalysts*, Ed.: K. P. de Jong, Wiley-VCH, Weinheim, **2009**.

[3] *Preparation of Solid Catalysts*, Eds.: G. Ertl, H. Knozinger, J. Weitkamp, Wiley-VHC, Weinheim, **1999**.

[4] *Supported Metals in Catalysis*, Eds.: J. A. Anderson, M. Fernandez-Garcia, Imperial College Press, London, **2005**

[5] *Catalyst Preparation: Science and Engineering*, Ed.: J. R. Regalbuto, CRC Press, Boca Raton, **2007**.

[6] J. A. Bergwerff, B. M. Weckhuysen, in *Handbook of Heterogeneous Catalysis*, 2nd ed. (Eds.: G. Ertl, H. Knozinger, F. Schuth, J. Weitkamp), **2008**, p. 1188.

[7] E. M. Assaf, L. C. Jesus, J. M. Assaf, *Chem. Eng. J.* **2003**, *94*, 93.

[8] A. V. Neimark, L. I. Kheifets, V. B. Fenelonov, *Ind. Eng. Chem. Prod. Res. Dev.* **1981**, *20*, 439.
[9] R. W. Maatman, C. D. Prater, *Ind. Eng. Chem.* **1957**, *49*, 253.
[10] E. Iglesia, S. L. Soled, J. E. Baumgartner, S. C. Reyes, *J. Catal.* **1995**, *153*, 108.
[11] E. R. Becker, J. Wei, *J. Catal.* **1977**, *46*, 365.
[12] K. Kunimori, I. Nakajima, T. Uchijima, *Chem. Lett.* **1982**, *11*, 1165.
[13] A. Lekhal, B. J. Glasser, J. G. Khinast, *Chem. Eng. Sci.* **2001**, *56*, 4473.
[14] A. Lekhal, B. J. Glasser, J. G. Khinast, *Chem. Eng. Sci.* **2004**, *59*, 1063.
[15] A. Lekhal, J. G. Khinast, B. J. Glasser, *Ind. Eng. Chem. Res.* **2001**, *40*, 3989.
[16] X. Liu, J. G. Khinast, B. J. Glasser, *Chem. Eng. Sci.* **2008**, *63*, 4517.
[17] A. J. van Dillen, R. J. A. M. Terörde, D. J. Lensveld, J. W. Geus, K. P. de Jong, *J. Catal.* **2003**, *216*, 257.
[18] J. R. A. Sietsma, J. D. Meeldijk, M. Versluijs-Helder, A. Broersma, A. J. v. Dillen, P. E. de Jongh, K. P. de Jong, *Chem. Mater.* **2008**, *20*, 2921.
[19] P. Salagre, J. L. G. Fierro, F. Medina, J. E. Sueiras, *J. Mol. Catal. A: Chemical* **1996**, *106*, 125.
[20] K. B. Agashe, J. R. Regalbuto, *J. Colloid Interface Sci.* **1997**, *185*, 174.
[21] K. Bourikas, C. Kordulis, A. Lycourghiotis, *Adv. Colloid Interfac.* **2006**, *121*, 111.
[22] K. Bourikas, C. Kordulis, A. Lycourghiotis, *Catal. Rev. Sci. Eng.* **2006**, *48*, 363.
[23] J. P. Brunelle, *Pure Appl. Chem.* **1978**, *50*, 1211.
[24] J. F. Lambert, M. Che, *J. Mol. Catal. A: Chemical* **2000**, *162*, 5.
[25] A. A. Tsyganenko, P. P. Mardilovich, *J. Chem. Soc. Faraday Trans.* **1996**, *92*, 4843.
[26] M. S. Heise, J. A. Schwarz, *J. Colloid Interface Sci.* **1985**, *107*, 237.
[27] M. S. Heise, J. A. Schwarz, *J. Colloid Interface Sci.* **1986**, *113*, 55.
[28] M. S. Heise, J. A. Schwarz, *J. Colloid Interface Sci.* **1988**, *123*, 51.
[29] M. S. Heise, J. A. Schwarz, *Stud. Surf. Sci. Catal.* **1987**, *31*, 1.
[30] J. A. Schwarz, M. S. Heise, *J. Colloid Interface Sci.* **1990**, *135*, 461.
[31] J.-F. Lambert, M. Hoogland, M. Che, *J. Phys. Chem. B* **1997**, *101*, 10347.
[32] F. Negrier, E. Marceau, M. Che, *Chem. Comm.* **2002**, 1194.
[33] F. Negrier, É. Marceau, M. Che, D. de Caro, *C. R. Chimie* **2003**, *6*, 231.
[34] F. Negrier, E. Marceau, M. Che, J. M. Giraudon, L. Gengembre, A. Lofberg, *J. Phys. Chem. B* **2005**, *109*, 2836.
[35] F. Négrier, E. Marceau, M. Che, J.-M. Giraudon, L. Gengembre, A. Löfberg, *Catal. Lett.* **2008**, *124*, 18.
[36] K.-Q. Sun, E. Marceau, M. Che, *Phys. Chem. Chem. Phys.* **2006**, *8*, 1731.
[37] J. Ryczkowski, *React. Kinet. Catal. Lett.* **1989**, *40*, 189.
[38] K. Al-Dalama, A. Stanislaus, *Energy & Fuels* **2006**, *20*, 1777.
[39] M. Baltes, P. V. D. Voort, B. M. Weckhuysen, R. R. Rao, G. Catana, R. A. Schoonheydt, E. F. Vansant, *Phys. Chem. Chem. Phys.* **2000**, *2*, 2673.
[40] B. M. Weckhuysen, *Angew. Chem. Int. Ed.* **2009**, *48*, 4910.
[41] B. M. Weckhuysen, in *Synthesis of Solid Catalysts*, 1st ed. (Ed.: K. P. de Jong), Wiley-VCH, Weinheim, **2009**, p. 201.
[42] T. Mang, B. Breitscheidel, P. Polanek, H. Knözinger, *Appl. Catal. A: General* **1993**, *106*, 239.

[43] J. A. Bergwerff, T. Visser, G. Leliveld, B. D. Rossenaar, K. P. de Jong, B. M. Weckhuysen, *J. Am. Chem. Soc.* **2004**, *126*, 14548.

[44] L. G. van de Water, J. A. Bergwerff, T. A. Nijhuis, K. P. de Jong, B. M. Weckhuysen, *J. Am. Chem. Soc.* **2005**, *127*, 5024.

[45] J. A. Bergwerff, M. Jansen, B. G. Leliveld, T. Visser, K. P. de Jong, B. M. Weckhuysen, *J. Catal.* **2006**, *243*, 292.

[46] L. G. A. van de Water, G. L. Bezemer, J. A. Bergwerff, M. Versluijs-Helder, B. M. Weckhuysen, K. P. de Jong, *J. Catal.* **2006**, *242*, 287.

[47] L. Espinosa-Alonso, K. P. de Jong, B. M. Weckhuysen, *J. Phys. Chem. C* **2008**, *112*, 7201; *Chapter 3 in this PhD thesis*.

[48] J. A. Bergwerff, A. A. Lysova, L. Espinosa Alonso, I. V. Koptyug, B. M. Weckhuysen, *Angew. Chem. Int. Ed.* **2007**, *46*, 7224.

[49] J. A. Bergwerff, A. A. Lysova, L. Espinosa-Alonso, I. V. Koptyug, B. M. Weckhuysen, *Chem. Eur. J.* **2008**, *14*, 2363.

[50] I. V. Koptyug, V. B. Fenelonov, L. Y. Khitrina, R. Z. Sagdeev, V. N. Parmon, *J. Phys. Chem. B* **1998**, *102*, 3090.

[51] A. M. Beale, S. D. M. Jacques, J. A. Bergwerff, P. Barnes, B. M. Weckhuysen, *Angew. Chem. Int. Ed.* **2007**, *46*, 8832.

[52] J.-D. Grunwaldt, B. Kimmerle, A. Baiker, P. Boye, C. G. Schroer, P. Glatzel, C. N. Borca, F. Beckmann, *Catal. Today* **2009**, *145*, 267.

[53] L. Ruffino, R. Mann, R. Oldman, E. H. Stitt, E. Boller, P. Cloetens, M. DiMichiel, J. Merino, *Can. J. Chem. Eng.* **2005**, *83*, 132.

Chapter 2

A UV-Vis-NIR Micro-spectroscopic Study to Rationalize the Influence of Cl^- (aq) on the Formation of Different Pd Macro-distributions on γ-Al_2O_3 Catalyst Bodies

Reproduced by permission of the PCCP Owner Societies.
L. Espinosa-Alonso, K. P de Jong, B. M. Weckhuysen, *A UV-Vis Micro-spectroscopic Study to Rationalize the Influence of Cl^- (aq) on the Formation of Different Pd Macro-distributions on γ-Al_2O_3 Catalyst Bodies* , Phys. Chem. Chem. Phys. **2009**, doi: 10.1039/B915753K.

Abstract

UV-Vis-NIR micro-spectroscopy has been applied to study the influence of the Cl^-(aq) concentration, solution pH and equilibration time on the $[PdCl_4]^{2-}$(aq) dynamics and molecular structure after impregnation of γ-Al_2O_3 support bodies. To do so, 0.2 wt% Pd catalysts have been prepared from acidic solutions (pH 1 and 5) of the Na_2PdCl_4 precursor salt containing different amounts of NaCl. It has been found that egg-shell catalysts are obtained in less than 24 h of equilibration when a less acidic pH (pH 5) is combined with $[Cl^-(aq)] < 0.6$ M, while to achieve egg-white catalysts the solution pH should be 1. Moreover, by increasing the equilibration time up to 96 h, the egg-shell profiles vanish to provide a uniform Pd distribution and the egg-white distribution becomes egg-yolk. Additionally, Pd complexes appear with different molecular structures depending on the solution pH, the equilibration time and the macro-distribution achieved. The protocol designed to prepare different Pd macro-distributions has been applied to prepare two Pd catalysts closer to commercial use; i.e., 1 wt% Pd concentrations, with egg-shell and egg-white profiles. The Pd dynamics and molecular structure was followed after impregnation, drying and calcination, demonstrating that the profiles created after impregnation are retained. Furthermore, UV-Vis-NIR micro-spectroscopy has proven that the initial Pd^{II} complexes in solution undergo hydrolysis after contacting the support and $[PdCl_2(OH)_2]^{2-}$ is formed. However, ligand exchange reactions of the $[PdCl_2(OH)_2]^{2-}$ complex take place during drying and $[PdCl_3(OH)]^-$ and $[PdCl_4]^{2-}$ complexes are obtained, which are retained after calcination.

Introduction

As described in Chapter 1, the efficiency of an industrial catalyst is determined by, among others, the macro-distribution of the active component within the support body, which is dependent on the interactions that take place between the metal-ion precursor and the support surface already during the impregnation step. It was also explained that one way of altering the interactions between the metal-ion precursor and the support surface is by changing the pH or ionic strength of the impregnation solution. In this way, previous studies have reported that lowering the solution pH or increasing the ionic strength boost the formation of more uniform profiles, when the metal-ion precursor $[PtCl_6]^{2-}$ is impregnated on γ-Al_2O_3 catalyst bodies.[1, 2] Furthermore, the addition of Cl^- (aq) on γ-Al_2O_3 is known to lower its pzc and to favor more uniform profiles of $[PtCl_6]^{2-}$ on γ-Al_2O_3 catalyst bodies.[3-5] A similar influence of the pH, ionic strength and concentration of Cl^- (aq) when the precursor metal ion is $[PdCl_4]^{2-}$ is expected, since both $[PtCl_6]^{2-}$ and $[PdCl_4]^{2-}$ complexes are anionic and stable in acidic solutions.

This brought us to investigate how Cl^- (aq) can affect the preparation of Pd/γ-Al_2O_3 pellets from the precursor Na_2PdCl_4. In this Chapter, it is demonstrated by means of UV-Vis-NIR micro-spectroscopy that additional Cl^- (aq) ions in the impregnation solution affect the Pd macro-distribution boosting more uniform profiles. Furthermore, it is shown that the final profiles depend on the solution pH, and that the concentration of Cl^- (aq) ions have an important role on the $[PdCl_{4-x}(HO)_x]^{2-}$ speciation within γ-Al_2O_3 catalyst bodies. Based on this study, an experimental protocol is proposed to prepare different Pd catalysts, which can be applied to prepare highly loaded catalysts.

Experimental Section

1. Catalyst Preparation

Two series of impregnation solutions containing sodium tetrachloropalladate (Na_2PdCl_4, ca. 36.4 wt% Pd, Acros) in a final 20 mM Pd concentration were prepared in order to yield 0.2 wt% Pd on the catalysts. These series have been labeled as Series A and Series B. Series A was prepared by dissolving Na_2PdCl_4 in an aqueous 112 mM HCl solution (from conc. HCl, Acros). Six solutions were prepared from Series A containing increasing amounts of NaCl (Acros p.a.) to a final chloride concentration ranging from 112 to 1000 mM. The chloride concentration is referred to the sum of HCl and NaCl, and not to that from the precursor Na_2PdCl_4 salt. Seven solutions in Series B were prepared by dissolving Na_2PdCl_4 in water and adding increasing amounts of NaCl (Acros p.a.) to the same final concentration of Cl^- (aq) as in Series A. The concentration of Cl^- (aq) (as the sum of HCl and NaCl) and the experimental pH of the solutions are summarized in Table 2.1.

Table 2.1. Overview of the 20 mM Pd impregnation solutions used in this work.

Series A	pH	Series B	pH	Cl^- (aq) /M*
-	-	**B0**	3.8	0
A1	0.9	**B1**	4.9	0.112
A2	0.9	**B2**	5.2	0.300
A3	0.9	**B3**	5.5	0.500
A4	0.8	**B4**	5.5	0.750
A5	0.7	**B5**	5.6	1.000
A6	0.9	**B6**	5.6	1.112

* $[Cl^-\ (aq)] = [Cl^-]_{NaCl} + [Cl^-]_{HCl}$

Additionally, two solutions were prepared by dissolving the required amounts of Na_2PdCl_4 (ca. 36.4 wt% Pd, Acros) to a final 94 mM Pd concentration to yield 1 wt% Pd on the catalysts. The solution labeled as 1wt%Pd-A1 was prepared by dissolving the Pd salt in a 112 mM HCl aqueous solution (from conc. HCl, Acros). The solution labeled as 1wt%Pd-B4 was prepared by dissolving the Pd salt in water and adding NaCl (Acros p.a.) to a final NaCl concentration of 750 mM. The experimental pH of the solutions was 1.1 (solution 1wt%Pd-A1) and 5.3 (solution 1wt%Pd-B4).

Cylindrical γ-Al_2O_3 pellets (Engelhard, 3 mm in height and diameter) were used. The support had a pore volume of 1.0 ml/g and a surface area of 200 m^2/g. The point of zero charge (pzc) was determined to be 7.8 by mass titration.[6] The γ-Al_2O_3 pellets were calcined at 450 °C for 8 h and stored at 120 °C until used.

The supported catalyst materials were prepared via pore volume impregnation on γ-Al_2O_3 pellets with all the Pd solutions prepared. The solutions were added drop-wise to the support bodies making sure that all the pellets in each batch (0.9 g) were wettened. The amount of solution added was equal to the pore volume plus 10 %. After adding the impregnation solution, manual shaking was applied during 2 min to obtain an even distribution of the solution on the pellets and the extra solution added (10 % of the pore volume) was removed with a pipette. After impregnation, the pellets were kept in a closed vessel with a wet tissue to avoid drying.

Two batches of pellets impregnated with solutions 1wt%Pd-A1 and 1wt%Pd-B4 were dried and calcined. The pellets were dried 3 h after impregnation (equilibration time). Drying was performed in a static air oven at 120 °C (5 °C/min) during 4 h. For calcination, the temperature was increased up to 500 °C (5 °C/min) and the pellets were held at this temperature for 4 h.

2. UV-Vis Spectroscopic Characterization

The impregnation solutions were characterized with UV-Vis spectroscopy. The UV-Vis spectra were recorded using a Cary 50 UV-Vis spectrophotometer working in the range of 300 to 700 nm. Table 2.2 summarizes the position of the Pd absorption bands measured in this range together with the Pd species present in all the solutions, calculated from deconvolution of the UV-Vis spectra measured. To do the deconvolution, the UV-Vis spectra collected on solution B0 ($PdCl_4^{2-}$) and B6 ($PdCl_3(H_2O)^-$) were used as single components and linear combinations of the two spectra were made in order to achieve the best fit.

The catalytic materials were measured after impregnation, drying or calcination with UV-Vis-NIR micro-spectroscopy, making use of a home-built set-up previously described in literature (Appendix A).[7] All measurements on the catalyst bodies were performed applying a line scan on the resulting surface of bisected pellets, as illustrated in Figure 1.3 of Chapter 1. The pellets were bisected by inserting them inside a silicon tube and the system tube-pellet was cut with a scalpel. Nine spectra were collected along the cross section of the bisected pellets with a spatial resolution of around 330 μm, for which 5 min were required. Sometimes, the UV-Vis-NIR spectra showed a spike at around 460 nm, this spike is due to interference from ambient light during the measurements.

Table 2.2. Pd^{II} speciation* and position of the Pd^{II} d-d transition band as a function of the impregnation solution.

		% Species				% Species	
Series A	Pd^{II} band /nm	$PdCl_4^{2-}$	$PdCl_3(H_2O)^-$	Series B	Pd^{II} band /nm	$PdCl_4^{2-}$	$PdCl_3(H_2O)^-$
-	-	-	-	B0	430	0	100
A1	455	56	44	B1	449	53	47
A2	471	79	21	B2	469	82	18
A3	474	90	10	B3	471	89	11
A4	474	96	4	B4	473	98	2
A5	474	95	5	B5	473	96	4
A6	474	100	0	B6	474	100	0

* Pd^{II} speciation was calculated from the deconvolution of the Pd^{II} d-d transition band.

Results and Discussion

1. UV-Vis-NIR Micro-spectroscopic Study on the Preparation of 0.2 wt% Pd Catalysts

The electronic spectra of $[PdCl_{4-x}(H_2O)_x]^{(x-2)}$ complexes in solution are characterized by, among others, a spin-forbidden d-d transition ($^1A_{2g} \longleftarrow {}^1A_{1g}$) of square-planar Pd^{II} complexes in the region between 350-500 nm.[8] The position of this band in the impregnation solutions is summarized in Table 2.2. The maximum absorption of the band shifts to shorter wavelengths when the chloride ligands are exchanged for water ligands (from solution A6 or B6 to solution A1 or B0), in agreement with the spectrochemical series of the ligands.[9] The band centered at 474 nm has been assigned to the complex $[PdCl_4]^{2-}$ while the band centered at 430 nm has been assigned to the complex $[PdCl_3(H_2O)]^-$.[10] Thus, when the band is in between these two positions it indicates the presence of a mixture of both complexes. Further hydrolysis of $PdCl_3(H_2O)^-$ yields more hydrolyzed complexes, $[PdCl_{4-x}(H_2O)_x]^{(x-2)}$ (x= 0 - 4). These complexes show a larger shift of the Pd^{II} d-d transition band to shorter wavelengths. Table 2.3 summarizes the position of this band, as reported by Elding et al.[10]

Table 2.3. Literature values of the PdII d-d transition band position for the different PdII chloride complexes in aqueous solution.[10]

Pd^{II} chloride complex	λ / nm
$[PdCl_4]^{2-}$	474
$[PdCl_3(H_2O)]^-$	431
$[PdCl_2(H_2O)_2]$	420
$[PdCl(H_2O)_3]^+$	406
$[Pd(H_2O)_4]^{2+}$	378

1.1. Immediately after Impregnation

After impregnation and 5 min of equilibration of any of the solutions from Series A or B, UV-Vis-NIR micro-spectroscopy indicated the presence of two bands at around 290 and 424 nm in the outer rim of the pellets. This is illustrated in Figure 2.1. According to literature, these two bands can be assigned to a ligand-to-metal charge transfer transition (LMCT, Cl^- to Pd^{II}) and a Pd^{II} d-d transition, respectively, of a similar structure to the square planar $[PdCl_2(H_2O)_2]$ complex in solution.[8] The maximum absorption of the Pd^{II} d-d transition band in the impregnation solutions (Table 2.2) has shifted to shorter wavelengths after impregnation. Thus, the alumina support caused a partial hydrolysis of the initial $[PdCl_4]^{2-}$ or $[PdCl_3(H_2O)]^-$. A similar phenomenon was already reported by Shelimov *et al.*[11] in the system $[PtCl_6]^{2-}$/Al_2O_3. In general, a shift to shorter wavelengths indicates an exchange of ligands by stronger ligands in the spectrochemical series. Therefore, the shift of the Pd^{II} d-d transition band to 424 nm after impregnation can be due to the exchange of two Cl^- ligands by H_2O, OH^- or Al-O^- (which stands for the hydroxyl groups from the alumina surface) ligands and formation of $[PdCl_2(H_2O)_2]$ or $[PdCl_2(X\text{-}O)_2]^{2-}$, where X = H or Al.[9, 12] The spectrochemical series of these ligands is known to be, on the one hand: Al-O^- < H_2O; and, on the other hand, OH^- < H_2O. However, no references have been found with respect to the spectrochemical series of Al-O^- and OH^-, and they are expected to be very close to each other in the spectrochemical series, making it hard to distinguish between $[PdCl_2(Al\text{-}O)_2]^{2-}$ and $[PdCl_2(OH)_2]^{2-}$. Since the Pd^{II} d-d transition band appeared at a slightly longer wavelength compared to that of the $[PdCl_2(H_2O)_2]$ complex in solution (424 nm instead of 420 nm), this new d-d transition band can be assigned to $[PdCl_2(X\text{-}O)_2]^{2-}$, where X = H or Al. Even though no clear distinction can be made between these two species based on the spectrochemical series of the ligands, this band has been assigned to the $[PdCl_2(OH)_2]^{2-}$ complex, as explained hereafter.

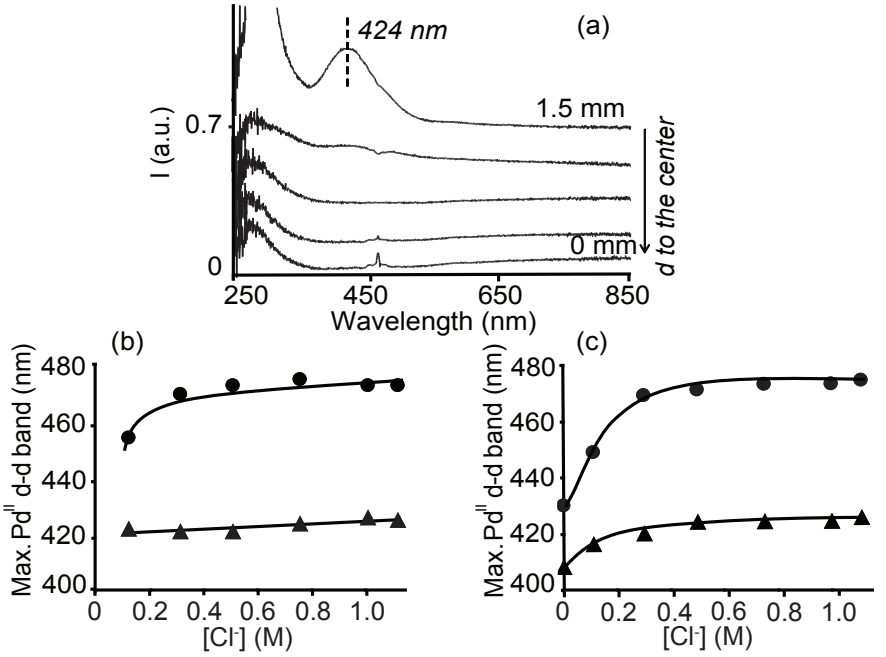

Figure 2.1. (a) Space resolved UV-Vis-NIR spectra measured on a γ-Al_2O_3 pellet, from the edge to the center, 5 min after impregnation with any of the prepared Pd^{II} impregnation solutions; (b) and (c) show the position of the Pd^{II} d-d transition band as a function of the Cl^- concentration in the impregnation solutions (-●-) and measured in the edge of the impregnated pellets 5 min after impregnation (-▲-), from Series A (b) and Series B (c).

It is known that the $[PdCl_4]^{2-}$ complex undergoes the following equilibria in solution in the absence of NaCl as a supporting electrolyte:[13, 14]

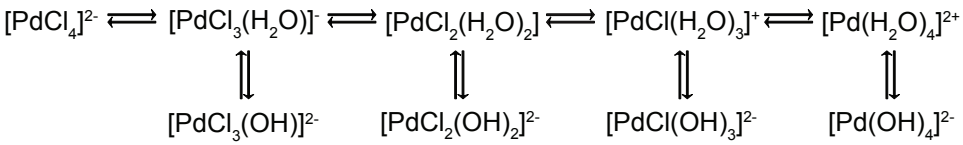

Scheme 2.1. Equilibria of aqueous Pd chloride complexes.[13, 14]

The formation of the aqueous species, top line in Scheme 2.1, is due to autohydrolysis, while the formation of the basic species (bottom line in the scheme) is generally due to alkaline hydrolysis. Moreover, autohydrolysis is dependent on the amount of additional Cl^- ions in the solution.[13] Hence, when Pd chloride complexes contact the alumina surface (Al-OH), which acts as an alkaline medium due to its higher pzc compared to the solution pH, they suffer alkaline hydrolysis and they become $[PdCl_2(OH)_2]^{2-}$, according to eq. (1):

$$[PdCl_4]^{2-} + 4\ Al\text{-}OH + 2\ H_3O^+ \longrightarrow [PdCl_2(OH)_2]^{2-} + 4\ Al\text{-}OH_2^+ + 2\ Cl^- \quad (1)$$

Even though it is not depicted in eq. (1), $[PdCl_3(H_2O)]^-$ undergoes the same alkaline hydrolysis reaction to form the same product, as deduced from the position of the Pd^{II} d-d transition band at around 424 nm, regardless of the components in the impregnation solution. This is illustrated in Figures 2.1 (b) and (c). This large shift of the absorption maximum towards shorter wavelengths clearly demonstrates that even though a strong electrostatic interaction between the initial negatively charged Pd^{II} complexes and the positively charged alumina would be expected, other ligand exchange reactions are taking place. Due to the buffering effect of alumina, $[PdCl_2(OH)_2]^{2-}$ is formed inside the pores of the support. Still, this negatively charged complex also interacts electrostatically with the positively charged alumina surface.

The pellet impregnated with solution B0, which did not contain any additional Cl^- (aq) ions, makes the exception to the formation of $[PdCl_2(OH)_2]^{2-}$. The space resolved UV-Vis-NIR spectra of this pellet showed a band in the edge of the catalyst body with a larger shift to shorter wavelengths. The band appeared centered at 408 nm, which can be assigned to $PdCl(OH)_3^{2-}$ (Figure 2.1 (c)). The formation of a further hydrolyzed complex is due to the absence of additional Cl^- (aq) ions, which are responsible for the stabilization of the chlorinated species.[13]

1.2. 2 h after Impregnation

Figure 2.2 shows the space resolved UV-Vis-NIR spectra from the edge to the center of two pellets after impregnation and 2 h after equilibration with solutions A3 and B3. The impregnated pellet with solution B3 (Figure 2.2 (b)) showed a band centered at 422 nm and a band below 300 nm, which was close to the detection limit of the equipment. These bands were only measured close to the outer rim of the pellets forming an egg-shell Pd distribution. As explained in the previous section, the band at 422 nm is assigned to the spin-forbidden Pd^{II} d-d transition of $[PdCl_2(OH)_2]^{2-}$ complexes, while the band at 300 nm is assigned to a LMCT transition of the same complex.

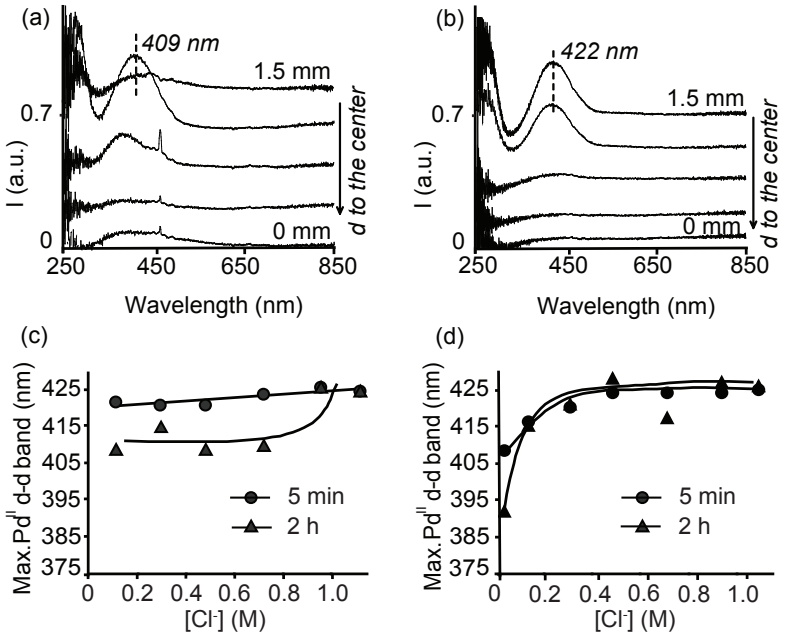

Figure 2.2. Space resolved UV-Vis-NIR spectra measured from the edge to the center of pellets impregnated with solution A3 (a) and B3 (b), 2 h after impregnation; and position of the Pd^{II} d-d transition band measured on pellets impregnated with Series A (c) and Series B (d) as a function of the Cl^- concentration 5 min after impregnation at the edge (-●-), and 2 h after impregnation (-▲-) at the edge (Series B) or at 0.4 mm from the edge (Series A).

The impregnated pellet with solution A3 (Figure 2.2 (a)) showed a band centered at 409 nm, this band was only measured at 1.1 mm from the center; i.e., not in the outer region but slightly deeper in the pellet in an egg-white distribution. This band, which shifted toward shorter wavelengths with time after impregnation, suggests the hydrolysis of $[PdCl_2(OH)_2]^{2-}$ to form a structure similar to $[PdCl(OH)_3]^{2-}$ (Table 2.3).

The space resolved UV-Vis-NIR spectra in Figure 2.2 indicate that the egg-shell distributions created 5 min after impregnation remained after 2 h when the pellets were impregnated with solution B3 (Figure 2.2 (b)), while impregnated pellets with solution A3 yielded Pd egg-white profiles (Figure 2.2 (a)). Moreover, a Pd egg-shell profile was obtained 2 h after impregnation of any solution from Series B, whereas a Pd egg-white profile was obtained 2 h after impregnation with any solution from Series A.

The Pd egg-white distribution after impregnation with Series A is formed due to the acidity of the impregnation solutions. As depicted in eq. (1), immediately after impregnation with an acidic solution mainly the alumina surface (Al-OH) becomes protonated and $[PdCl_2(OH)_2]^{2-}$ is formed. Protonation of the alumina surface occurs mainly on the basic hydroxyl groups (Al_B-OH) and it yields an acid-base reaction between the protonated hydroxyl species and Cl^-, as described in eq. (2), and, consequently, alumina becomes more acidic (lower pzc):[4, 6, 15]

$$Al_B\text{-}OH + H^+ + Cl^- \longrightarrow Al_B\text{-}OH_2^+ + Cl^- \longleftrightarrow Al_B\text{-}Cl + H_2O \qquad (2)$$

Thus, Cl^- ions in an acidic medium act as a competitor for the adsorption sites of Pd^{II} anionic complexes on the alumina surface. In order to achieve a Pd egg-white distribution the adsorption of Cl^- must be more favorable than that of $[PdCl_2(OH)_2]^{2-}$. The reaction that takes place in the edges of the pellet after 2 h is described as follows:

$$[PdCl_2(OH)_2]^{2-} + 2\ Al_B\text{-}OH_2^+ + 2\ Cl^- \longrightarrow [PdCl_2(OH)_2]^{2-} + 2\ [Al_B\text{-}OH_2^+ \cdots\cdots Cl^-] + 2\ H_2O \qquad (3)$$

According to this reaction, there are no electrostatic interactions between $[PdCl_2(OH)_2]^{2-}$ and the alumina surface. This is because the adsorption sites of alumina in the edges of the pellet are occupied by Cl^-, and $[PdCl_2(OH)_2]^{2-}$ can move

deeper in the catalyst body creating an egg-white distribution. The adsorption of Cl^- (aq) on alumina is more pronounced at the edges, where the protonation of the alumina hydroxyl groups is the strongest. Towards the core of the pellet, the solution in the pores becomes more basic. Thus, the more acidic the solution the more chlorinated the alumina becomes. This fact explains also why when the pellets were impregnated with Series B, uniform distributions of Pd were achieved. At higher pH values (Series B), the reaction in eq. (2) is not so favorable. Adsorption of Cl^- (aq) on the alumina surface does not occur to the same extent as for impregnated pellets with Series A. Hence, $[PdCl_2(OH)_2]^{2-}$ species are partly retained due to electrostatic interactions with the positively charged alumina surface at the edges of the catalyst bodies.

It must be taken into account that alumina is not stable in acidic pH, and it can partially dissolve liberating Al^{3+} ions after impregnation of acidic solutions. These ions can ultimately become part of the active phase influencing the catalyst efficiency. In this work, no influence of the presence of Al^{3+} on the UV-Vis-NIR spectra of Pd chloride species could be observed. Therefore, even though the formation of Al^{3+} ions cannot be ignored, it will not be taken into account in the discussion regarding the UV-Vis-NIR micro-spectroscopic data.

Figures 2.2 (c) and (d), additionally, show that the maximum absorption of the Pd^{II} d-d transition band shifted to shorter wavelengths 2 h after impregnation of the pellets with Series A (Figure 2.2 (c)), while there was no shift of the position of this band 2 h after impregnation with Series B. When the pellets were impregnated with Series A, the Pd^{II} d-d transition band was measured at around 410 nm except for the pellets impregnated with solutions A6 and A7, which contained very high concentrations of Cl^- (aq). In general, $[PdCl_2(OH)_2]^{2-}$ has undergone further hydrolysis forming a structure similar to $[PdCl(OH)_3]^{2-}$. This is a consequence of the adsorption of Cl^- (aq) on the alumina surface. Because of the adsorption of Cl^- (aq), the solution inside the pores lost Cl^- ions, which no longer stabilized $[PdCl_2(OH)_2]^{2-}$ complexes.

When the pellets were impregnated with Series B, $[PdCl_2(OH)_2]^{2-}$ complexes are stabilized (band at around 422 nm) because adsorption of Cl^- (aq) does not occur to a large extent. Hence, the concentration of Cl^- in solution is high and further hydrolysis of the $[PdCl_2(OH)_2]^{2-}$ complex is avoided.

1.3. Effect of Longer Equilibration Times

It is known that different profiles can be obtained just by elongating the equilibration time between impregnation and drying.[16] Moreover, in this work it is also reported that impregnated pellets with Series A yielded egg-white distributions if the equilibration time is increased up to 2 h. The development of an egg-white distribution brought us to investigate what would happen if this equilibration time was increased even further. Even though a longer equilibration time might not be useful for industrial purposes, it will clearly give more fundamental insight in the interfacial chemistry involved in catalyst preparation.

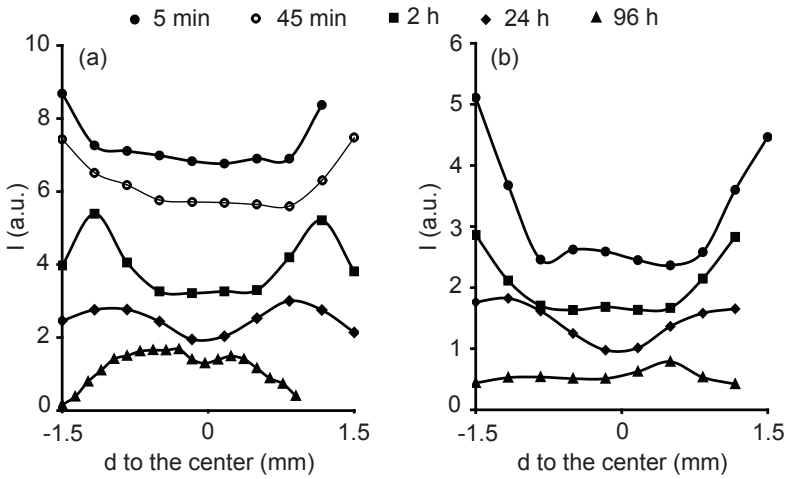

Figure 2.3. Maximum absorption of the Pd^{II} d-d transition band measured with UV-Vis-NIR micro-spectroscopy as a function of position inside the pellet and time after impregnation of solution (a) A6, and (b) B6.

Figure 2.3 shows the intensity of the Pd^{II} d-d transition band measured at different times after impregnation of solutions A6 and B6, and it indicates that longer equilibration times yield different distributions. This figure illustrates the development of egg-yolk and uniform Pd macro-distributions as a function of time after impregnation of pellets with solutions A6 and B6.

Impregnation with solution B6 yielded a uniform profile of Pd after 96 h, while impregnation with solution A6 gave rise to an egg-yolk Pd distribution. These

Pd macro-distributions depended on the solution pH, and, a uniform profile was favorable for solutions with pH 5 (Series B), whereas solutions with pH 1 (Series A) yielded egg-yolk macro-distributions. Moreover, they also depended on the Cl^- concentration, and they were only formed when the impregnation solutions had a very high concentration of Cl^- (aq) ions (data not shown).

Additionally, the position of the maximum absorption of the Pd^{II} d-d transition band depended on the Cl^- (aq) concentration and solution pH. Figure 2.4 shows the position of the maximum absorption of the Pd^{II} d-d transition band in the catalyst bodies measured 2 h after impregnation at the point on the pellet where the intensity of the band was the highest, and in the center of the pellet 96 h after impregnation.

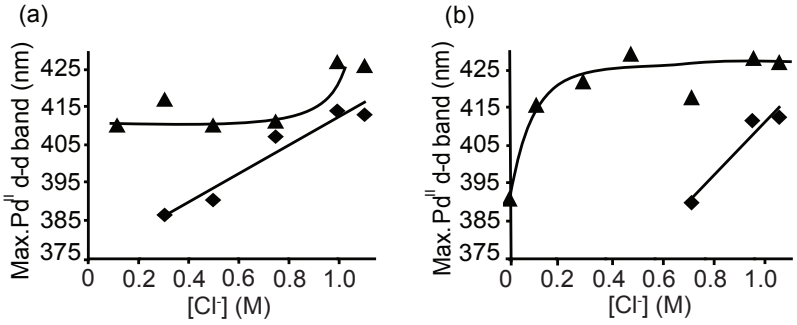

Figure 2.4. Position of the maximum absorption of the Pd^{II} d-d band as a function of Cl^- concentration, 2 h close to the outer rim (-▲-) and 96 h in the center (-■-) of the pellet after impregnation with Series A (a) and Series B (b).

96 h after impregnation, the Pd^{II} d-d transition band was not observed in the center of the catalyst bodies for solutions with low Cl^- concentration, for that reason some points do not appear in the figure. Moreover, when Pd^{II} ions reached the core it was surrounded at maximum by one Cl^- ligand as $[PdCl(OH)_3]^{2-}$, as deduced from the position of the Pd^{II} d-d transition band measured between 385 and 412 nm regardless the solution pH (Table 2.2). As explained earlier in this work, the alkaline hydrolysis of Pd chloride complexes towards the core is a direct consequence of the buffering effect of the alumina support. Thus, the higher the concentration of Cl^- ions in the impregnation solution the more chlorinated the Pd^{II} present in the core.

1.4. Protocol to Create Different Pd Macro-distributions

Figure 2.5 illustrates the Pd macro-distributions and species achieved as a function of pH, concentration of Cl^- ions and equilibration time, as deduced from UV-Vis-NIR micro-spectroscopy, together with the composition of these pellets.

Based on Figure 2.5 we can conclude that in order to achieve uniform or egg-yolk Pd distributions, long equilibration times are required in combination with $[Cl^-(aq)] \geq 0.6$ M.

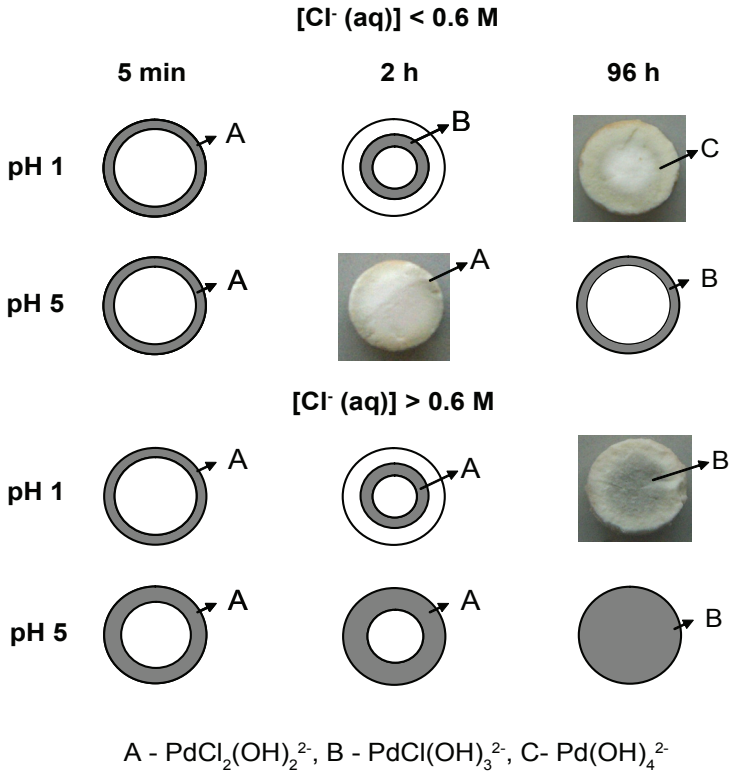

Figure 2.5. Pd macro-distributions developed as a function of the solution pH, Cl^- (aq) concentration, and equilibration time; together with the Pd composition.

As was previously described, Cl^- (aq) act as a competitive anion in acidic environments. At low pH values, adsorption of Cl^- on the alumina surface is preferential and $[PdCl_2(OH)_2]^{2-}$ complexes can move forward in the support body while Cl^- (aq) is retained in the outer rim occupying all the adsorption sites in that area. Consequently, an egg-yolk Pd distribution is created. On the other hand, when the solution pH is around 5, there is no competition between Cl^- (aq) and $[PdCl_2(OH)_2]^{2-}$ and, therefore, the probabilities of adsorption of one or the other anion are the same, yielding a uniform Pd macro-distribution. In any case, the concentration of active component is below the concentration required to saturate the alumina surface. This, combined with the strong electrostatic interactions between the Pd complexes formed in the pores of the alumina results in a slow transport rate of Pd towards the core of the support body, and long equilibration times are required to achieve uniform and egg-yolk Pd catalysts. If higher Pd loadings are required, the equilibration times could be reduced, as it is explained in the next section.

2. UV-Vis-NIR Micro-spectroscopic Study on the Preparation of 1 wt% Pd Catalysts

Sometimes higher Pd loadings are required to have a better performance of the industrial process. For this reason, the developed methodology explained above to tune from egg-shell to egg-white, egg-yolk or uniform profiles was applied to prepare 1 wt% Pd/γ-Al_2O_3 catalyst bodies.

2.1. UV-Vis-NIR Micro-spectroscopy of the Impregnated Pellets

2.1.1. 5 min after Impregnation

Figure 2.6 illustrates the space resolved UV-Vis-NIR spectra of the impregnated pellets with 1 wt% Pd solutions, after 5 min of equilibration. A similar egg-shell distribution of Pd complexes for the two impregnation solutions was deduced. However, the position of the UV-Vis-NIR bands measured indicated that different Pd complexes were present depending on the impregnation solution.

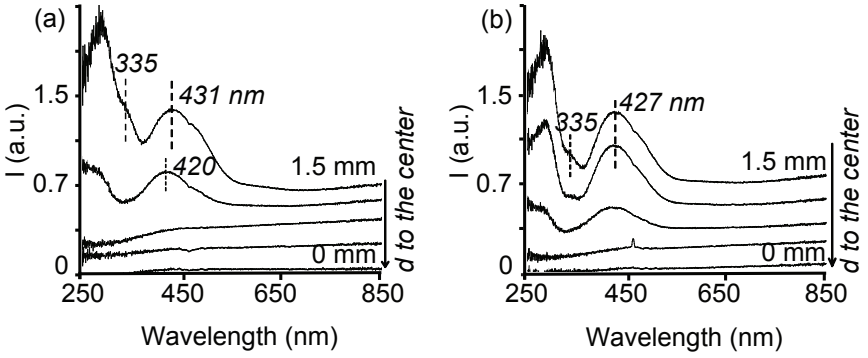

Figure 2.6. Space resolved UV-Vis-NIR spectra from the edge to the center of pellets 5 min after impregnation with solutions (a) 1wt%Pd-A1, and (b) 1wt%Pd-B4.

The UV-Vis-NIR spectra on the pellet impregnated with solution 1wt%Pd-B4 (Figure 2.6 (b)) indicated the presence of Pd in a structure similar to $[PdCl_2(H_2O)_2]$, as suggested by the position of the Pd^{II} d-d transition at 427 nm. Following the same reasoning as for the 0.2 wt% Pd catalysts, Pd is most likely present as $[PdCl_2(OH)_2]^{2-}$ due to hydrolysis. A shoulder at around 335 nm, which is only observed in the edge of the pellet, suggests that together with $[PdCl_2(H_2O)_2]$, a small amount of $[PdCl_4]^{2-}$ is also present.[8, 10] On the other hand, the space resolved UV-Vis-NIR spectra on the pellet impregnated with solution 1wt%Pd-A1 (Figure 2.6 (a)) show a different pattern and indicate that the impregnated $[PdCl_4]^{2-}$ complex underwent hydrolysis while moving towards the core of the pellet. The spectrum in the edge is characterized by a band at 431 nm and a shoulder at 335 nm, which can be assigned respectively to the Pd^{II} d-d transitions of $[PdCl_3(H_2O)]^-$ and $[PdCl_4]^{2-}$. However, 0.4 mm deeper in the pellet the Pd^{II} d-d band at 431 nm shifted to 420 nm, which is assigned to $[PdCl_2(H_2O)_2]$ (Table 2.3). The presence of $[PdCl_4]^{2-}$, regardless of the solution pH, suggests that part of the Pd^{II} ions in the pores of alumina do not interact with the surface of the alumina and remain in the bulk liquid of the pores. Hence, they do not suffer hydrolysis. Still, the dynamics and molecular structure of Pd, 5 min after impregnation with 1 wt% Pd solutions correlates rather well with the findings for 0.2 wt% Pd catalysts described in this Chapter.

2.1.2. 3 h after Impregnation

During the equilibration time, Pd complexes moved deeper in the catalyst bodies. Figure 2.7 shows the space resolved UV-Vis-NIR spectra from the edge to the center of the impregnated pellets after 3 h. The impregnated pellet with solution 1wt%Pd-B4 (Figure 2.7 (b)) showed the maximum absorption of the Pd^{II} d-d band 3 h after impregnation at around 424 nm, which was assigned to the complex $[PdCl_2(OH)_2]^{2-}$, in agreement to what was observed for the 0.2 wt% Pd system (sample B4 with the same concentration of Cl^- ions). Thus, the position of the Pd^{II} d-d transition band shifted towards shorter wavelengths during equilibration time, indicative of hydrolysis of the initial Pd chloride complexes. When the pellet was impregnated with solution 1wt%Pd-A1 and equilibrated for 3 h (Figure 2.7 (a)), the band appeared centered at 419 nm in a uniform distribution. Comparing this profile to the profile obtained after impregnation of solution A1, in which the band appeared centered at around 410 nm, we can conclude that probably $[PdCl(OH)_3]^{2-}$ was present with small amounts of $[PdCl_2(OH)_2]^{2-}$ complex. Hence, the lower concentration in Cl^- ions in the impregnation solutions yielded further hydrolysis of the initial $[PdCl_4]^{2-}$ complex. The bands at 419 nm and 424 nm were measured in any position along the cross section of the catalyst bodies, but with different intensities. The intensity of these bands as a function of the position in the catalyst bodies is also included in Figure 2.7. After 3 h of equilibration time, Pd was somewhat depleted at the edges of the pellet when this was impregnated with the 1wt%Pd-A1 solution (Figure 2.7 (c)). On the other hand, an almost uniform Pd distribution was noted if the impregnation was done with the 1wt%Pd-B4 solution (Figure 2.7 (d)). These profiles were expected according to the solution pH, equilibration time and Cl^- concentration (Figure 2.5). However, these profiles were not as sharp as obtained for the 0.2 wt% Pd samples, and Pd was already detected in the core of the pellets.

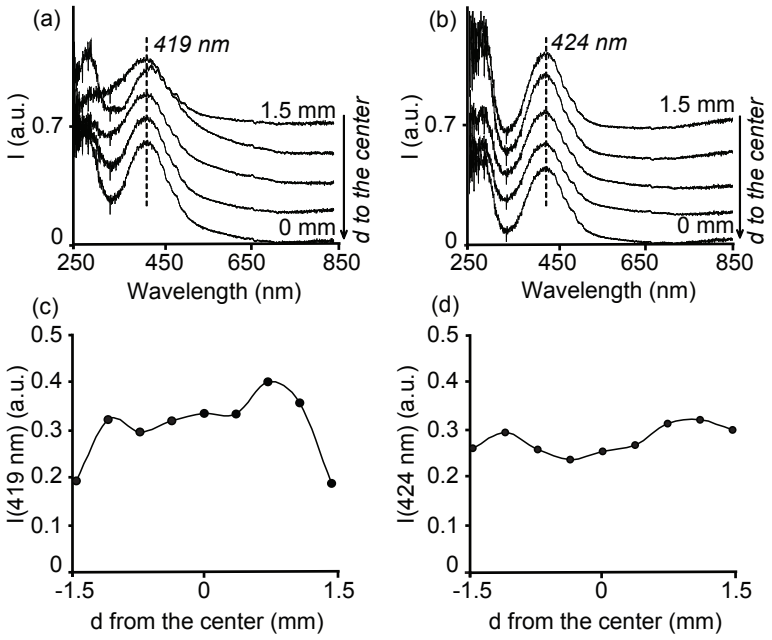

Figure 2.7. Space resolved UV-Vis-NIR spectra from the edge to the center of pellets 3 h after impregnation with solutions (a) 1wt%Pd-A1 (b) 1wt%Pd-B4. The intensity of the corresponding Pd^{II} d-d band is also represented as a function of the position in the catalyst body after impregnation with solution (c) 1wt%Pd-A1, and (d) 1wt%Pd-B4.

2.2. UV-Vis-NIR Micro-spectroscopy of Dried Pellets

Figure 2.8 illustrates the space resolved UV-Vis-NIR spectra measured on the 1wt%Pd pellets after drying. These spectra suggest that the Pd profiles achieved after 3 h of equilibration remained after drying. Thus, grafting of the complexes on the alumina surface has taken place during drying. Moreover, the space resolved UV-Vis-NIR spectra measured on the dried pellets compared to the 3-h-impregnated samples showed a shift of the position of the Pd^{II} d-d transition band to 430, 435 or 459 nm and the appearance of a shoulder a 335 nm. A shift towards longer wavelengths indicates that weaker ligands in the spectrochemical series entered in the 1st coordination sphere of Pd.[9] The dried pellet containing a 1wt%Pd-B4 solution showed a band centered at 435 nm and a shoulder at 335 nm homogeneously distributed (Figure 2.8 (b)). An additional band at around 280 nm was also present,

which is assigned to a LMCT transition from Cl^- to Pd^{II}. Considering that the species present in the pellets 3 h after impregnation are $[PdCl_2(OH)_2]^{2-}$, a shift towards longer wavelengths, to 435 nm, after drying can only be explained by an exchange of OH^- groups with Cl^- ligands forming $[PdCl_3(OH)]^{2-}$. Moreover, taking into account that grafting of the complex took place during drying, it is assumed that the molecular structure of Pd after drying was not $[PdCl_3(OH)]^{2-}$ but $[PdCl_3(O\text{-}Al)]^{2-}$, where the oxygen-like ligand is a deprotonated hydroxyl group from the alumina surface. The formation of the latter grafted complex to the alumina surface would take place with the release of a molecule of water. Still, according to the spectrochemical series of ligands any of the two structures are in agreement with a band at 435 nm. Moreover, the shape of this band suggests that a small contribution above 450 nm is also present, which is indicated in the figure. The shoulder at 335 nm is characteristic of $[PdCl_4]^{2-}$ complexes. This complex also shows a Pd^{II} d-d transition band at 474 nm (see Table 2.3), which corresponds to the asymmetry above 450 nm of the band centered at 435 nm. Therefore, we can conclude that after drying there is a mixture of $[PdCl_4]^{2-}$ and $[PdCl_3(O\text{-}Al)]^{2-}$ along the cross section of the catalyst body.

The dried pellet containing a 1wt%Pd-A1 solution showed a much more chlorinated outer rim, as deduced from the shoulder at 335 nm and the band centered at 459 nm in the edge of the catalyst body (Figure 2.8 (a)). The latter band suggests a mixture of $[PdCl_4]^{2-}$ and $[PdCl_3(Al\text{-}O)]^-$ complexes. The spectra towards the core resembled those measured on the pellet containing a 1wt%Pd-B4 solution. However, no shoulder at 335 nm is observed and the band at 430 nm is more symmetrical (no contribution above 450 nm). Thus, even though there was a mixture of $[PdCl_3(O\text{-}Al)]^{2-}$ and $[PdCl_4]^{2-}$, the location of these two structures depended on the position of the pellet with the outer rim richer in $[PdCl_4]^{2-}$ complexes and the core containing more $[PdCl_3(O\text{-}Al)]^{2-}$ species.

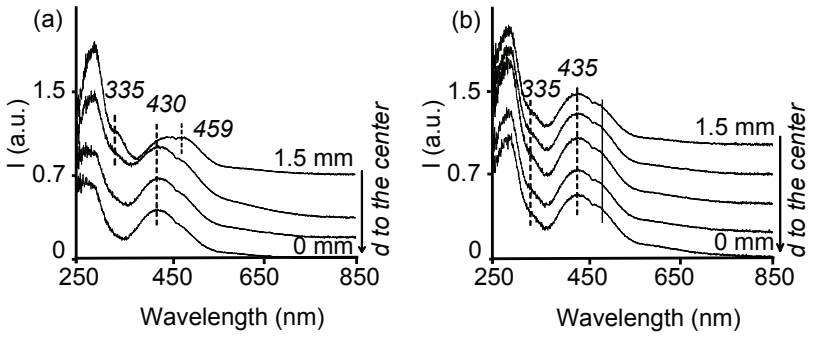

Figure 2.8. Space resolved UV-Vis-NIR spectra from the edge to the center of dried pellets impregnated with solutions (a) 1wt%Pd-A1 (b) 1wt%Pd-B4.

The formation of more chlorinated complexes after drying is in agreement with previous studies reported on the adsorption mechanism of Pd on alumina during catalyst preparation. Bozon-Verduraz *et al*.[17] suggested that after impregnation of an acidic solution which contained $PdCl_2$, the alumina surface becomes chlorinated and a deposit of $PdCl_2$ is formed, while drying yielded the regeneration of $[PdCl_4]^{2-}$ as the chloride ions from the alumina surface enter the coordination sphere of Pd. In this study we have shown that indeed a regeneration of chlorinated Pd complexes after drying takes place. However, the regeneration capacity of $[PdCl_4]^{2-}$ depends on the effect that Cl^- has on the alumina surface after impregnation. The chlorination of the alumina surface is pH dependent and is enhanced at more acidic pHs.[4] Therefore, impregnation with a 1wt%Pd-A1 solution yielded the exchange of alumina hydroxyl groups with Cl^- groups, especially in the outer rim of the pellet. Thus, a ring of chlorinated alumina is formed close to the edges and the formation of a region richer in $[PdCl_4]^{2-}$ complex in that area after drying is expected. On the other hand, alumina is less chlorinated in the core and Pd adsorbs on alumina as $[PdCl_3(O\text{-}Al)]^-$. This is also the case if the pellets are impregnated with a 1wt%Pd-B4 solution.

2.3. UV-Vis-NIR Micro-spectroscopy of Calcined Pellets

Figure 2.9 illustrates the space resolved UV-Vis-NIR spectra of the calcined pellets. These spectra show an absorption band centered at 428 nm, regardless the position in the catalyst body and the impregnation solution used for catalyst preparation. Moreover, a second absorption band was measured at around 260 nm,

very close to the detection limit of the equipment.

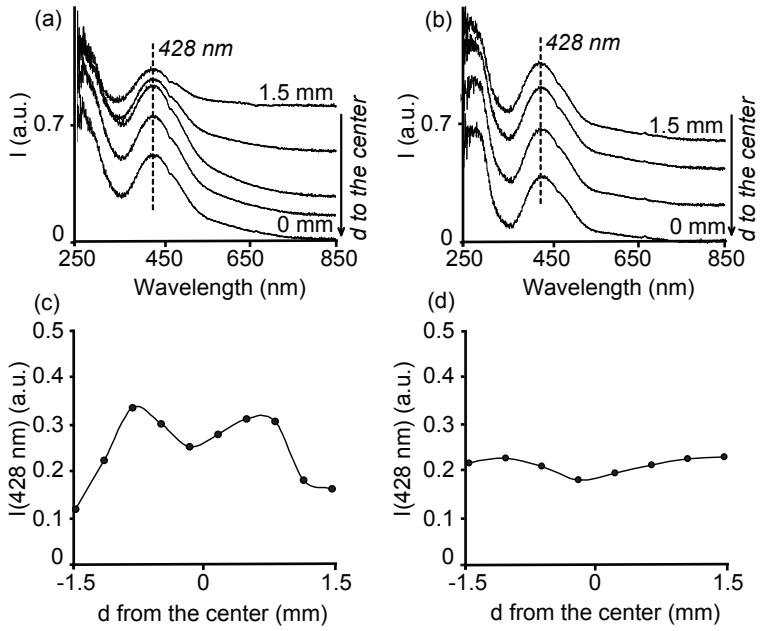

Figure 2.9. Space resolved UV-Vis-NIR spectra from the edge to the center of calcined catalyst bodies after impregnation with solutions (a) 1wt%Pd-A1, (b) 1wt%Pd-B4. The intensity of the band at 428 nm as a function of the position in the catalyst body is also shown (c) 1wt%Pd-A1, and (d) 1wt%Pd-B4.

The presence of this absorption band suggests that only partial loss of Cl^- ligands from the molecular structure of Pd complexes during calcination took place yielding the formation of a structure similar to $[PdCl_2(O\text{-}Al)_2]^{2-}$. The water ligands have been exchanged by the hydroxyl groups from the alumina surface, which are known to be weaker ligands in the spectrochemical series.[12] The presence of Cl^- can also be inferred from the absorption band at around 260 nm, which corresponds to a LMCT from Cl^- to Pd^{II}. No speciation of $[PdCl_{4-x}(H_2O)_x]^{(x-2)}$ complexes was measured along the catalyst body; i.e., the absorption band appeared centered at 428 nm regardless of the position within the pellet. However, this band showed a different intensity depending on its position in the catalyst body, as depicted in Figures 2.9 (b) and (c). These figures show that the Pd macro-distributions achieved 3 h after impregnation were retained after the drying and the calcination process, which indicates that strong interactions between alumina and Pd species took

place from the first step of catalyst preparation. On the other hand, the position of the Pd^{II} d-d transition band after calcination suggests that Cl^- remained in the catalyst since if metallic Pd or PdO was formed during the calcination, this band would be non-existing or would appear at around 410 nm.[18] Residual chlorine blocking the active sites of the Pd surface is known to have a detrimental effect on the catalyst performance.[19-21] In order to remove the Cl^- ions from the catalysts, higher temperatures or additional activation steps are required; and, consequently, a compromise between the desired particle size of Pd and the Cl^- concentration in the catalytic materials should be reached.[20, 21]

Conclusions

UV-Vis-NIR micro-spectroscopy has revealed that, immediately after impregnation, $[PdCl_4]^{2-}$ is not stable in contact with alumina and it undergoes hydrolysis to form $[PdCl_2(HO)_2]^{2-}$ species, which interact electrostatically with the alumina surface. Moreover, the stability and macro-distribution of these species within γ-Al_2O_3 catalyst bodies depend on the concentration of Cl^- (aq) ions, the solution pH and equilibration time; and different non-uniform/uniform catalysts can be prepared by tuning these three parameters. The formation of one or another Pd macro-distribution is caused by a combined effect of the solution pH, acidification of the alumina surface and change in the molecular structure of the Pd precursor complex when this one contacts the alumina support. Still, the adsorption of the Pd complexes on the γ-Al_2O_3 surface during impregnation is strong enough, and no redistribution takes place during drying on thermal treatment. After drying, chlorinated Pd is regenerated and retained after calcination. Thus, even though the use of Cl^- (aq) ions is a successful method to achieve different Pd macro-distributions, these anions, which are poisonous for the Pd active phase, cannot be completely removed from the catalysts during their preparation.

Acknowledgments

Dr. A. Iglesias-Juez (Inorganic Chemistry and Catalysis group, Utrecht University) is thanked for fruitful discussions. Ad Mens (Inorganic Chemistry and Catalysis group, Utrecht University) is thanked for the N_2 physisorption measurements on the γ-Al_2O_3 support.

References

[1] M. S. Heise, J. A. Schwarz, *J. Colloid Interface Sci.* **1985**, *107*, 237.
[2] M. S. Heise, J. A. Schwarz, *J. Colloid Interface Sci.* **1986**, *113*, 55.
[3] R. Maatman, *Ind. Eng. Chem.* **1959**, *51*, 913.
[4] J. A. Mieth, J. A. Schwarz, Y. J. Huang, S. C. Fung, *J. Catal.* **1990**, *122*, 202.
[5] Y.-S. Shyr, W. R. Ernst, *J. Catal.* **1980**, *63*, 425.
[6] A. R. McInroy, D. T. Lundie, J. M. Winfield, C. C. Dudman, P. Jones, S. F. Parker, D. Lennon, *Catal. Today* **2006**, *114*, 403.
[7] L. G. van de Water, J. A. Bergwerff, T. A. Nijhuis, K. P. de Jong, B. M. Weckhuysen, *J. Am. Chem. Soc.* **2005**, *127*, 5024.
[8] L. I. Elding, L. F. Olsson, *J. Phys. Chem.* **1978**, *82*, 69.
[9] A. B. P. Lever, *Inorganic Electronic Spectroscopy*, Elsevier Science B. V., Amsterdam, **1987**.
[10] L. I. Elding, *Inorg. Chim. Acta* **1972**, *6*, 647.
[11] B. N. Shelimov, J. F. Lambert, M. Che, B. Didillon, *J. Mol. Catal. A: Chemical* **2000**, *158*, 91.
[12] J.-F. Lambert, M. Hoogland, M. Che, *J. Phys. Chem. B* **1997**, *101*, 10347.
[13] N. B. Milić, Ž. D. Bugarčić, *Trans. Met. Chem.* **1984**, *9*, 173.
[14] S. Y. Troitskii, M. A. Fedotov, V. A. Likholobov, *Russ. Chem. Bull.* **1993**, *42*, 634.
[15] L. Espinosa-Alonso, K. P. de Jong, B. M. Weckhuysen, *J. Phys. Chem. C* **2008**, *112*, 7201; *Chapter 3 in this PhD thesis*.
[16] R. W. Maatman, C. D. Prater, *Ind. Eng. Chem.* **1957**, *49*, 253.
[17] F. Bozon-Verduraz, A. Omar, J. Escard, B. Pontvianne, *J. Catal.* **1978**, *53*, 126.
[18] A. B. Gaspar, L. C. Dieguez, *Appl. Catal. A: General* **2000**, *201*, 241.
[19] T. Lear, R. Marshall, J. A. Lopez-Sanchez, S. D. Jackson, T. M. Klapotke, M. Baumer, G. Rupprechter, H.-J. Freund, D. Lennon, *J. Chem. Phys.* **2005**, *123*, 174706.
[20] Q. Lin, Y. Ji, Z.-D. Jiang, W.-D. Xiao, *Ind. Eng. Chem. Res.* **2007**, *46*, 7950.
[21] D. Roth, P. Gélin, M. Primet, E. Tena, *Appl. Catal. A: General* **2000**, *203*, 37.

Chapter 3

Combined UV-Vis-NIR and IR Micro-spectroscopies to Study the Effect of the Nickel Precursor on the Impregnation and Drying of γ-Al_2O_3 Catalyst Bodies

Adapted with permission from L. Espinosa-Alonso, K. P de Jong, B. M. Weckhuysen, *Effect of the Nickel Precursor on the Impregnation and Drying of γ-Al_2O_3 Catalyst Bodies: A UV-Vis and IR Microspectroscopic Study*, J. Phys. Chem C **2008**, *112*, 7201-7209.

Abstract

The elemental preparation steps of impregnation and drying of Ni/γ-Al_2O_3 catalyst bodies have been studied by combining UV-Vis-NIR and IR micro-spectroscopy. The influence of the number of chelating ligands in $[Ni(en)_x(H_2O)_{6-2x}]^{2+}$ precursor complexes (with *en* = ethylenediamine and x = 0 - 3) has been investigated. UV-Vis-NIR micro-spectroscopic measurements after impregnation showed that, regardless the molar *en*:Ni^{2+} ratio in the precursor solution, Ni^{2+} was present in the core of the pellets already 5 min after impregnation. The alumina support did bring about, however, gradients in the nature of the Ni^{2+} species upon first contact with the lowest *en*:Ni^{2+} ratio solutions, but these gradients disappeared 30 - 60 min after impregnation. After 60 min, UV-Vis-NIR suggested Ni-O-Al interactions between Ni^{2+} and the support, when water was initially part of the first coordination sphere of Ni^{2+}, which was supported with the results obtained after drying. For dried samples, UV-Vis-NIR indicated a gradient of $[Ni(en)_x(H_2O)_{6-2x}]^{2+}$ inside the pellets, with an *en*-poor region in the core and an *en*-rich region in the edges of the catalyst bodies, when $[Ni(en)_3]^{2+}$ or $[Ni(en)_2(H_2O)_2]^{2+}$ were the starting complexes. IR micro-spectroscopy confirmed these *en* radial profiles, while EDX measurements showed that a Ni^{2+} egg-shell distribution goes hand-in-hand with an egg-shell distribution of *en*. The number of *en* ligands determined the interactions of Ni^{2+} with the support after impregnation and controlled the redistribution of metal-ion species during drying. Moreover, when redistribution of Ni^{2+} occurred during drying, its transport towards the outer rim of the pellets came about together with changes of the local *en*:Ni^{2+} ratio.

Introduction

Chapter 1 adresses that one way of modifying the adsorption/desorption phenomena of the metal-ion precursor species on the support surface can be by changing the nature of the precursor metal-ion complex; namely by adding chelating ligands to the impregnation solution and, thus, changing the 1st coordination sphere of the metal-ion complex. The use of chelating agents in the impregnation solutions can have a large impact in the final catalytic material, as explained in Chapter 1, since these ligands can avoid the redistribution of the active precursor during the drying step and/or they can improve the dispersion and reducibility of the final catalyst.[1-3]

In this Chapter, the influence of the number of *en* ligands on the macro-distribution and molecular speciation of Ni^{2+} in γ-Al_2O_3 catalyst bodies during impregnation and drying has been investigated by means of UV-Vis-NIR and IR micro-spectroscopies. For this purpose, the transport of different $[Ni(en)_x(H_2O)_{6-2x}]^{2+}$ precursor complexes (with x = 0 - 3) towards the core of the catalyst bodies and their interactions with the alumina support surface, after impregnation and drying, have been monitored with UV-Vis-NIR micro-spectroscopy, while the macro-distribution of *en* has been studied after drying with IR micro-spectroscopy. Based on these data the origin of different Ni macro-distributions will be discussed.

Experimental Section

1. Catalyst Preparation

$[Ni(en)_x(H_2O)_{6-2x}]^{2+}$ impregnation solutions were prepared at room temperature by adding ethylenediamine (*en*) (99 %, Acros) to an aqueous solution of $Ni(NO_3)_2{\cdot}6H_2O$ (Acros, p.a.) as to obtain a final Ni^{2+} concentration of 0.5 M and *en*:Ni^{2+} molar ratios = 0, 1, 2 and 3. The name and natural pH of the solutions together with the Ni^{2+}-speciation in the precursor solutions are listed in Table 3.1. EnNi0 corresponds to an aqueous 0.5 M $Ni(NO_3)_2$ solution. One additional solution with an *en*:Ni^{2+} ratio of 3 was prepared with a final pH of 4 by addition of HNO_3 (p.a., Acros).

Cylindrical γ-Al_2O_3 catalyst bodies (Engelhard, 3 mm in height and diameter) were used. The support had a pore volume of 1.0 ml/g and a surface area of 200 m^2/g, as determined by N_2 physisorption. The point of zero charge (pzc) was determined

to be 8 by mass titration.[4] The γ-Al_2O_3 pellets were calcined at 450°C for 8 h and stored at 120 °C until used. In one experiment, HCl treated alumina pellets, labeled as Al_2O_3-AC, were used as support. These pellets were prepared by passing a flow of HCl(g)/He (10 %, 10 ml/min) at 50 °C through a batch of 0.6 g of Al_2O_3 pellets during 5 h.

The supported catalyst materials were prepared by pore volume impregnation on γ-Al_2O_3 (or Al_2O_3-AC) pellets with the Ni^{2+} impregnation solutions (3 wt% Ni). The solutions were added dropwise to the support and the amount added was equal the pore volume plus 10 %. After adding the impregnation solution, manual shaking was applied during 2 min to obtain an even distribution of the solution on the pellets and the extra solution added (10 % of the pore volume) was removed with a pipette. After impregnation, the pellets were kept in a closed vessel for 2 h (equilibration time). The dried pellets were dried in a preheated oven under static air at 100 °C for 8 h after the 2 h of equilibration time.

To study the influence of the drying temperature on the macro-distribution and molecular structure of the Ni^{2+}-complexes along the catalyst body, three batches of pellets were impregnated with EnNi3 solution and dried at 20, 60 and 90 °C.

2. Catalyst Characterization

UV-Vis-NIR spectra of the impregnation solutions were recorded using a Cary 50 UV-Vis spectrophotometer in the range of 240 to 1100 nm. The catalytic materials were measured after impregnation and drying with UV-Vis-NIR micro-spectroscopy, making use of the experimental set-up depicted in Appendix A.[5] All measurements on the catalyst bodies were performed applying a line scan on the resulting surface of bisected pellets, as presented in Figure 1.3 of Chapter 1. The pellets were bisected by inserting them inside a silicon tube; the system tube-pellet was cut with a scalpel. Nine spectra were collected along the cross section of the bisected pellets with a spatial resolution of around 330 μm, for which 5 min were required. IR spectra on dried pellets were recorded with a Perkin Elmer Autoimage IR microscope (reflectance mode) with a spatial resolution of 200 μm (200 scans averaging). Energy dispersive analysis of X-rays (EDX) were performed with an XL30SFEG (FEI, The Netherlands) scanning electron microscope. Analysis of the spectra was done with EDAX software (Tilburg, The Netherlands). Diffuse reflectance near infrared (NIR) spectra were recorded at room temperature on crushed pellets in the range of 1100-

1600 nm using a Varian Cary 500 spectrometer equipped with an integration sphere and a halon white disk as the reference.

Results and Discussion

1. Chemistry of the $[Ni(en)_x(H_2O)_{6-2x}]^{2+}$ Impregnation Solutions

Table 3.1 summarizes the species present in the impregnation solutions under study, calculated based on the formation constants of $[Ni(en)_x(H_2O)_{6-2x}]^{2+}$ (x = 1 - 3) complexes, as a function of the pH of the solutions.[6] The experimental UV-Vis-NIR absorption bands of the solutions are also listed in Table 3.1. Three bands were observed in all solutions at around 350, 600 and 1000 nm. Assuming an octahedral symmetry of the Ni^{2+} complexes, these bands can be assigned to the $^3T_{1g}(P) \leftarrow {}^3A_{2g}$, $^3T_{1g}(F) \leftarrow {}^3A_{2g}$ and $^3T_{2g} \leftarrow {}^3A_{2g}$ d-d spin allowed transitions, respectively.[7] A blue shift of the Ni^{2+} d-d transition bands was observed as the *en*:Ni^{2+} ratio increases from 0 to 3, indicating that *en* ligands, which are stronger ligands in the spectrochemical series than water, entered into the first coordination sphere of Ni^{2+}.[7] The Ni^{2+} d-d transitions were responsible of the characteristic colors of these solutions, from green for solution EnNi0 passing through blue (solution EnNi1) to different shades of purple (solutions EnNi2 and EnNi3). An absorption band at around 300 nm was observed in all the impregnation solutions, which corresponded to a NO_3^- n $\rightarrow \pi^*$ charge transfer transition.[32] Solution EnNi0 showed, in addition, an absorption band at around 730 nm, which can be assigned to a d-d spin forbidden transition of Ni^{2+}.[7] The UV-Vis-NIR spectrum of solution EnNi3pH4 resembled that of solution EnNi0 due to its acidification. Protonation of *en* ligands occurred causing the formation of complex $[Ni(H_2O)_6]^{2+}$ (86 %), as reported in Table 3.1.

Table 3.1. Overview of the Ni^{2+} impregnation solutions and the characteristic absorption bands of the Ni^{2+} complexes.

	Composition			Ni speciation (%)				Absorption Bands		
Solutions	Ni /M	*en* /M	pH	$Ni(H_2O)_6^{2+}$	$Ni(en)(H_2O)_4^{2+}$	$Ni(en)_2(H_2O)_4^{2+}$	$Ni(en)_3^{2+}$	λ_1 /nm	λ_2 /nm	λ_3 /nm
EnNi0	0.5	0.0	4.7	100	0	0	0	391	654	>1100
EnNi1	0.5	0.5	6.5	17	65	17	1	368	615	961
EnNi2	0.5	1.0	7.5	0	9	82	9	352	565	924
EnNi3	0.5	1.5	8.5	0	0	3	97	343	546	893
EnNi3pH4	0.5	1.5	4.0	86	14	0	0	391	654	>1100

2. Near Infrared Spectroscopy of the γ-Al_2O_3 Surface

Figure 3.1 (a) shows the diffuse reflectance near infrared (NIR) spectrum on crushed γ-Al_2O_3 pellets in the region between 1350 and 1600 nm. This region, characteristic for the first overtone of the OH stretching vibrations (2υ), shows a broad band with three maxima at 1384, 1416 and 1446 nm. The maxima indicated the presence of surface OH groups with different basicity: basic OH groups are characteristic of the signal at 1384 nm, neutral groups at 1416 nm and acidic groups at 1446 nm.[8, 9] These basic, neutral and acidic surface OH groups will be referred as Al_B-OH, Al_n-OH and Al_A-OH, respectively. The acid-base properties of alumina surface hydroxyl groups are determined by the coordination of the OH group to Al^{3+} as follows: different coordination to Al^{3+} gives rise to a different net charge on the oxygen: the higher the negative charge on the oxygen, the more basic the hydroxyl groups.[10, 11] It has to be considered, however, that there are more than three different hydroxyl groups on alumina surface.[11]

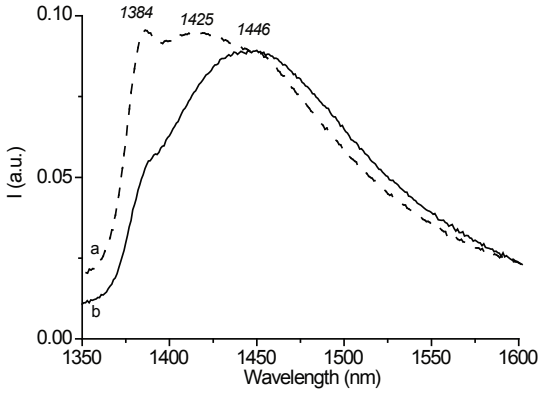

Figure 3.1. Diffuse reflectance NIR spectra measured on (a) crushed Al_2O_3 pellets, and (b) on chlorinated alumina pellets, Al_2O_3-AC.

As explained in Chapter 1, due to the different acid-base properties of alumina surface hydroxyl groups, these can become protonated in the presence of an acidic solution ($pH_{solution}$ < pzc), leading to a bulk pH increase of the solution in the pores and a positively charged alumina surface, or they can become deprotonated in a basic medium ($pH_{solution}$ > pzc).[12] Basic OH groups (Al_B-OH) will become more easily protonated in an acidic medium, whereas Al_A-OH will deprotonate in a basic medium, eq. (1) and (2):

$$Al_B\text{-}OH + H^+ \longrightarrow Al_B\text{-}OH_2^+ \quad (1)$$

$$Al_A\text{-}OH + OH^- \longrightarrow Al_A\text{-}O^- + H_2O \quad (2)$$

The NIR spectrum of HCl-treated alumina, denoted as sample Al_2O_3-AC, in Figure 3.1 (b) shows a broad band centered at 1446 nm and a shoulder at 1384 nm. The lower intensity of the reflection at 1384 nm compared to non-treated alumina (Figure 3.1 (a)) was consistent with the consumption of basic hydroxyl groups due to the chlorination treatment, according to the following reaction:[13]

$$Al_B\text{-}OH + HCl \longrightarrow Al_B\text{-}Cl + H_2O \quad (3)$$

Moreover, the shift of the band maximum to longer wavelengths indicated acidification of alumina, as it is known to occur.[14, 15]

3. Study of the Impregnation Step of $[Ni(en)_x(H_2O)_{6-2x}]^{2+}$ Solutions

3.1. UV-Vis-NIR Micro-spectroscopy after Initial Contact Solution-Support

The space resolved UV-Vis-NIR spectra collected from the edge to the center of the pellets, 5 min after impregnation, with solutions EnNi0 to EnNi3 are shown in Figure 3.2. Ni^{2+} was detected with a rather uniform absorption profile of the d-d transition bands in the four samples and a fast migration rate of Ni^{2+} complexes was apparent.

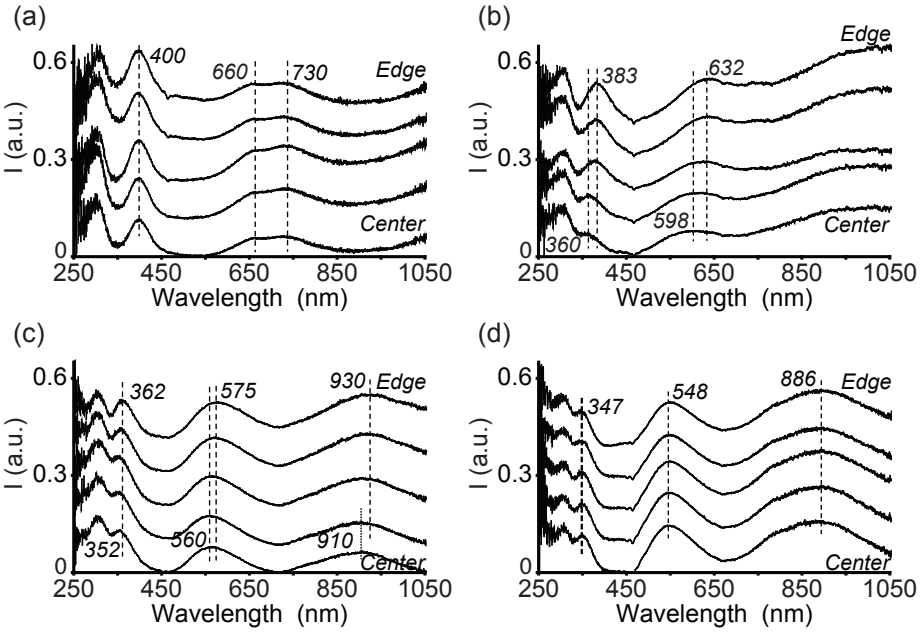

Figure 3.2. Space resolved UV-Vis-NIR spectra collected from the edge to the center of bisected pellets, 5 min after impregnation with solutions: (a) EnNi0, (b) EnNi1, (c) EnNi2 and (d) EnNi3.

Impregnated EnNi0 pellets show a uniform distribution of $[Ni(H_2O)_6]^{2+}$ complexes with the absorption bands λ_1 and λ_2 at 400 and 660 nm, respectively; band λ_3, which maximum absorption in solution appeared at wavelengths longer than 1100 nm, is beyond the detection limits of the set-up (Figure 3.2 (a)). The charge transfer transition band of NO_3^- at 300 nm and the Ni^{2+} d-d spin forbidden transition band at around 730 nm are also observed in the spectra. The Ni^{2+} absorption bands due to the spin allowed d-d transitions show a constant intensity along the cross section of the pellet, suggesting a fast transport of Ni^{2+} towards the core. Thus, weak or no interactions between $[Ni(H_2O)_6]^{2+}$ and alumina surface were taking place 5 min after impregnation. However, they appear slightly shifted to longer wavelengths compared to the bands for the EnNi0 solution, as shown in Table 3.1. This red shift can be explained as follows. The low pH of an aqueous solution of nickel nitrate is brought about by the following equilibrium:[12]

$$[Ni(H_2O)_6]^{2+} + H_2O \longrightarrow [Ni(H_2O)_5(OH)]^{+} + H_3O^{+} \quad (4)$$

When a $[Ni(H_2O)_6]^{2+}$ solution contacts the alumina support, the formation of $[Ni(H_2O)_5(OH)]^{+}$ is enhanced as the alumina basic hydroxyl groups will consume protons (eq. (1)). The UV-Vis-NIR absorption bands of this species appear at slightly longer wavelengths compared to that of $[Ni(H_2O)_6]^{2+}$ since OH^- is a weaker ligand in the spectrochemical series than H_2O.[7]

If γ-Al_2O_3 pellets were impregnated with solutions EnNi1 and EnNi2, a shift of the d-d absorption bands, λ_1, λ_2 and λ_3, to shorter wavelengths was monitored from the edge to the center of the pellets (Figures 3.2 (b) and (c)). In the EnNi1 sample, the Ni^{2+} d-d bands λ_1 and λ_2 at the edges were measured at 383 and 632 nm, respectively; i.e., λ_1 and λ_2 shifted to longer wavelengths compared to the corresponding bands in the precursor EnNi1 solution (Table 3.1). Additionally, in the center of the pellets, λ_1 and λ_2 bands appeared at 360 and 598 nm with band λ_2 being very broad. The maximum absorption position of band λ_3 was difficult to determine because of the broadness of the band and the intrinsic detection limit of the set-up. Visual inspection revealed the interior of the pellet to turn from blue, close to the edges, to purple, close to the core, in correspondence with the blue-shift of the d-d absorption bands towards the core of the pellets.

These observations can be explained by realizing that when the complex $[Ni(en)(H_2O)_4]^{2+}$ contacted the alumina support (the edges), the acidic OH groups of alumina may partly protonate the *en* ligands of $[Ni(en)(H_2O)_4]^{2+}$ complexes, forming enH^+ and enH_2^{2+}, the former not indicated for simplicity:

$$[Ni(en)(H_2O)_4]^{2+} + 2\ Al_A\text{-}OH + 2\ H_2O \longrightarrow [Ni(H_2O)_6]^{2+} + 2\ Al_A\text{-}O^- + enH_2^{2+} \quad (5)$$

When these species were transported towards the core of the pellet, enH_2^{2+} could deprotonate due to its interaction with Al_B-OH, loosing either one (enH^+) or even both protons (*en*). Therefore, increasing the pH of the solution towards the core of the pellets, and deprotonated *en* could react further with the precursor complex to form $[Ni(en)_{1+x}(H_2O)_{(4-2x)}]^{2+}$, $x \geq 0$, (eq. (6) and (7)):

$$enH_2^{2+} + 2\ Al_B\text{-}OH \longrightarrow en + 2\ Al_B\text{-}OH_2^{+} \quad (6)$$

$$[Ni(en)(H_2O)_4]^{2+} + x\ en \longrightarrow [Ni(en)_{1+x}(H_2O)_{(4-2x)}]^{2+} + 2x\ H_2O \quad (7)$$

The gradient of Ni^{2+} species 5 min after impregnation could only develop because after this time there was still not an even distribution of Ni^{2+} concentration inside the pellets and enH_2^{2+}/ *en* moved faster than $[Ni(en)(H_2O)_4]^{2+}$. In the center of the pellets the concentration of Ni^{2+} was lower than the concentration of surface hydroxyl groups making it possible to locally and temporarily create Ni^{2+} complexes which are only stable at high pH.

The space resolved spectra of a pellet impregnated with solution EnNi2 (Figure 3.2 (c)) show a red shift of the Ni^{2+} d-d absorption bands in the edge (362, 575 and 930 nm) compared to the precursor solution (Table 3.1); whereas in the core, the bands were measured at the same positions as in the solution (352, 560 and 910 nm), indicating the presence of $[Ni(en)_2(H_2O)_2]^{2+}$ species. A similar scheme of reactions is proposed to occur in the edges of EnNi2 impregnated pellets as for EnNi1, see eq. (8). Again, towards the core, enH_2^{2+} can partially or totally deprotonate forming enH^+ or *en*, as represented in eq. (6). This equation only shows the total deprotonation of enH_2^{2+} for simplicity.

$$[Ni(en)_2(H_2O)_2]^{2+} + 2x\ Al_A\text{-}OH + 2x\ H_2O \longrightarrow [Ni(en)_{2-x}(H_2O)_{2+2x}]^{2+} + x\ enH_2^{2+} + 2x\ Al_A\text{-}O^- \quad (8)$$

In the core of the pellet, $[Ni(en)_2(H_2O)_2]^{2+}$ was regenerated.

Figure 3.2 (d) shows the space resolved UV-Vis-NIR spectra from the edge to the center on an impregnated pellet with solution EnNi3. The Ni^{2+} d-d bands appear uniformly distributed at 347, 548 and 886 nm, which are the same positions as in the impregnation solution (Table 3.1) indicating that the $[Ni(en)_3]^{2+}$ complex did not interact strongly with the support.

The fast penetration rate of the $[Ni(en)_3]^{2+}$ complex together with the stability of its molecular structure can be explained with the *physical adsorption* model developed by Regalbuto *et al.*[16] which proves that, for some systems, adsorption of metal-ion complexes during impregnation occur primarily by electrostatic interactions. The pH of the EnNi3 solution was very close to the pzc of the support, so the support had an overall zero surface charge and no interactions between the Ni^{2+} complex and alumina took place. Therefore, the pH of the solution inside the pores did not change and so the molecular structure of Ni^{2+}.

3.2. UV-Vis-NIR Micro-spectroscopy after Equilibration for 2 h

After 2 h of equilibration, uniform distributions of the Ni^{2+} complexes were measured in all the impregnated samples, as shown in Figure 3.3.

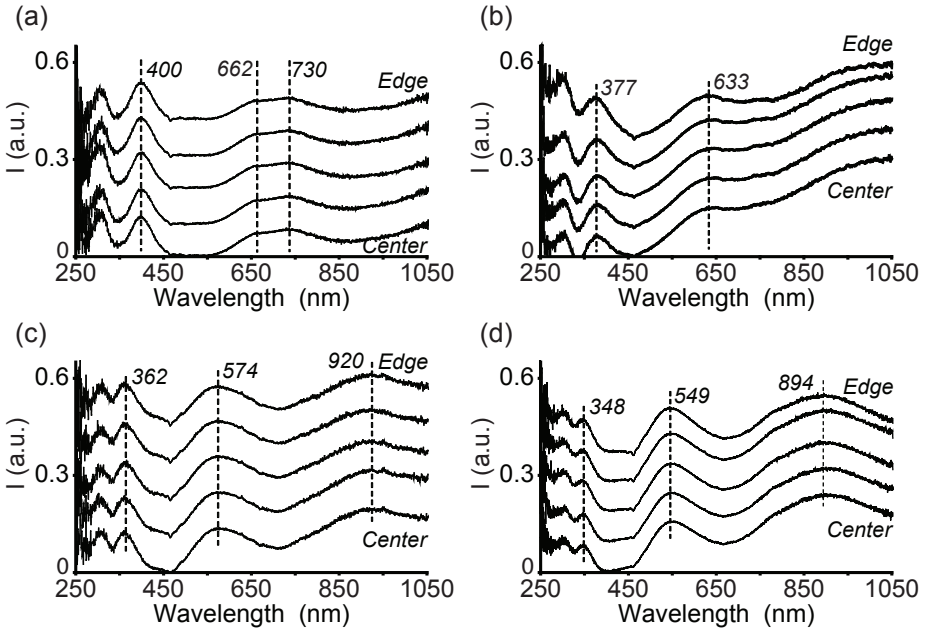

Figure 3.3. Space resolved UV-Vis-NIR spectra measured after equilibration for 2 h on bisected pellets from the edge to the core: (a) EnNi0, (b) EnNi1, (c) EnNi2 and (d) EnNi3.

The 2-hour impregnated EnNi0 pellet shows a uniform distribution of octahedral Ni^{2+} complexes with d-d transition bands λ_1 and λ_2 at 400 and 662 nm; λ_3 was beyond the detection range of the set-up (Figure 3.3 (a)). The spectra collected were identical to those measured 5 min after impregnation (Figure 3.2 (a)). One possible reason to justify the position of the λ_1 and λ_2 bands could be that specific interactions between $[Ni(H_2O)_6]^{2+}$ and hydroxyl groups from alumina took place certain time after impregnation (up to 2 h), eq. (9) and (10):

$$Al\text{-}OH + [Ni(H_2O)_6]^{2+} \longrightarrow [Al\text{-}O\text{-}Ni(H_2O)_5]^{+} + H_3O^{+} \quad (9)$$

$$2\ Al\text{-}OH + [Ni(H_2O)_6]^{2+} \longrightarrow [(Al\text{-}O)_2Ni(H_2O)_4] + 2\ H_3O^{+} \quad (10)$$

The specific adsorption of $[Ni(H_2O)_6]^{2+}$ on γ-Al_2O_3 during the wet step of catalyst preparation was also reported by Geus *et al*.[17] some years ago, and they proposed a similar mechanism of Ni^{2+} interaction with the hydroxyl surface of alumina. However, it should also be considered that, during this time, it was possible that no specific interactions with the support took place, and the bands were shifted due to the presence of the partially hydrolyzed $[Ni(H_2O)_{6-x}(OH)_x]^{2-x}$ complex formed by the influence of the alumina hydroxyl surface, as mentioned to occur immediately after impregnation. In any case, as proposed by Lambert *et al*.[18], the exchange of water ligands by OH groups due to hydrolysis or by hydroxyl groups from the alumina surface (Al-OH) yields a shift of the Ni^{2+} d-d transition bands to longer wavelengths since both OH^- and Al-OH are weaker ligands in the spectrochemical series than water.[7, 18]

Along the cross section of impregnated EnNi1 pellets after 2 h of equilibration, two d-d absorption bands centered at 377 and 633 nm were measured with a constant intensity (Figure 3.3 (b)). Again, the maximum absorption of band λ_3 was difficult to determine. The gradient of species $[Ni(en)_{1+x}(H_2O)_{6-2x}]^{2+}$ ($x \geq 0$) created after initial contact of the solution with the support disappeared 30 - 60 min after impregnation. However, the red shift of the Ni^{2+}d-d bands with respect to those of the impregnation solution indicates that weaker ligands in the spectrochemical series entered the Ni^{2+} 1st coordination sphere of Ni^{2+} and grafting to the alumina surface could be a possible mechanism to it:

$$[Ni(en)(H_2O)_4]^{2+} + \text{Al-OH} \longrightarrow [\text{Al-O-Ni}(en)(H_2O)_3]^{+} + H_3O^{+} \quad (11)$$

$$[Ni(en)(H_2O)_4]^{2+} + 2\ \text{Al-OH} \longrightarrow [(\text{Al-O})_2\text{Ni}(en)(H_2O)_2] + 2\ H_3O^{+} \quad (12)$$

The space resolved UV-Vis-NIR spectra of the EnNi2 pellet after 2 h of equilibration show the Ni^{2+} d-d bands at 362, 574 and 920 nm evenly distributed along the cross section of the pellet (Figure 3.3 (c)). These bands appear shifted to longer wavelengths compared to those measured in the EnNi2 impregnation solution (Table 3.1), or in the pellet 5 min after impregnation (Figure 3.2 (c)). As in the EnNi1 sample, a change in the Ni^{2+} coordination sphere occurred with time after impregnation, where possibly water ligands were partially substituted by surface hydroxyl groups from the alumina:

$$[Ni(en)_2(H_2O)_2]^{2+} + Al\text{-}OH \longrightarrow [Al\text{-}O\text{-}Ni(en)_2(H_2O)]^{+} + H_3O^{+} \quad (13)$$

$$[Ni(en)_2(H_2O)_2]^{2+} + 2\ Al\text{-}OH \longrightarrow [(Al\text{-}O)_2Ni(en)_2] + 2\ H_3O^{+} \quad (14)$$

Finally, the space resolved UV-Vis-NIR spectra measured on the EnNi3 impregnated pellet, after 2 h, shown in Figure 3.3 (d), is the same as in the solution or 5 min after impregnation (Figure 3.2 (d)). The Ni^{2+} d-d bands were measured at 348, 549 and 894 nm indicating that $[Ni(en)_3]^{2+}$ species were present uniformly distributed inside the pellets without interacting with the alumina hydroxyl surface.

In summary, the strength of adsorption of Ni^{2+} on the alumina surface during the equilibration period depends on the number of *en* molecules in the 1st coordination sphere of Ni^{2+}, in such a way that the more *en* molecules surrounding Ni^{2+} the weaker the interactions between this complex and the alumina surface. Figure 3.4 shows a two-dimensional (2D) plot in which the position of the λ_2 band in the edge of a pellet is depicted in the *x* axis, while the position of the λ_2 band in the core of the pellet is depicted in the *y* axis, both of them 2 h after impregnation. If no interactions would take place between the Ni^{2+} complexes and the alumina surface, then this band would appear at the same position as in the impregnation solutions regardless the location on the pellet, which corresponds to the points represented as green triangles. On the other hand, the purple diamonds represent the real position of the λ_2 band measured 2 h after impregnation.

Thus, the distance between the green triangle and purple diamond for each sample represents the shift of the band λ_2 2 h after impregnation, and can be translated into the interaction strength between the complex and the alumina surface, as follows:

EnNi3 < EnNi2 ~ EnNi0 < EnNi1

It is still under debate which are the OH groups involved in these interactions. After impregnation, only a very small amount of basic hydroxyl groups would become protonated, since the concentration of H^+ coming from the solution inside alumina pores is very low, and can be negligible. Therefore, most probably the interactions between the support surface and $[Ni(en)_x(H_2O)_{6-2x}]^{2+}$ (x = 0 - 3) occurs through the neutral form of basic OH groups or through the neutral or acidic OH groups. Most likely, it occurs through the neutral form of basic OH groups, since

these have the higher negative charge.[11]

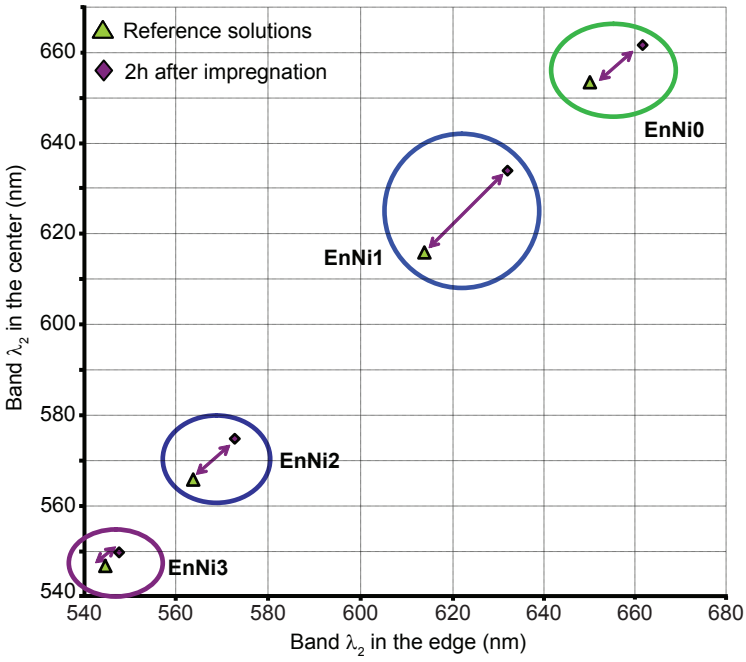

Figure 3.4. 2D plot showing the shift of the λ_2 band 2 h after impregnation for all the impregnated pellets with respect to the position of that band in the impregnation solutions; i.e., the position of the λ_2 band on the impregnated pellets if no interactions between the Ni^{2+} complexes and the alumina surface were taking place.

3.3. UV-Vis-NIR Micro-spectroscopy after Impregnation of γ-Al_2O_3 Pellets with Solution EnNi3pH4

The space resolved UV-Vis-NIR spectra measured from the edge to the center of the EnNi3pH4 pellet 5 min after impregnation is shown in Figure 3.5 (a).

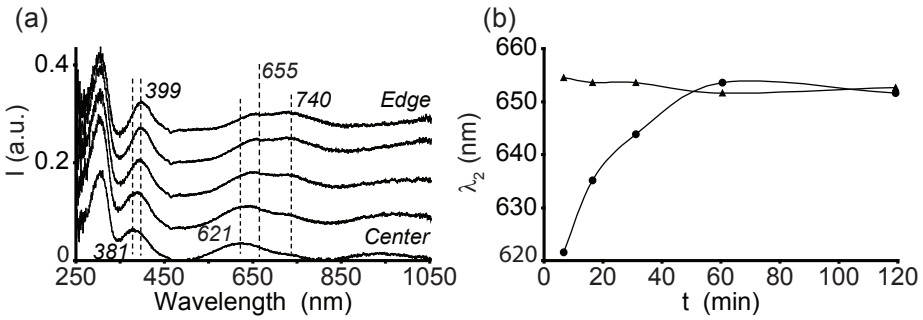

Figure 3.5. (a) Space resolved UV-Vis-NIR spectra measured on a EnNi3pH4 bisected pellet, from the edge to the core, 5 min after impregnation. (b) Position of band λ_2 at the edge (▲) and in the core (●) as a function of the time after impregnation on pellet EnNi3pH4.

These spectra changed drastically from the edge to the core of the pellet. The typical UV-Vis-NIR spectrum of $[Ni(H_2O)_6]^{2+}$ complex was observed in the edges, with the characteristic Ni^{2+} absorption bands at 399, 655 and 740 nm; whereas, in the core, a marked shift of the bands to shorter wavelengths was observed, with the Ni^{2+} d-d bands λ_1 and λ_2 at 381 and 621 nm, respectively. The spectrum in the core was close to that of $[Ni(en)(H_2O)_4]^{2+}$. The band shift came along with a change of color inside the pellets from green, in the outer area, to purple, in the center. The blue shift of the absorption bands towards the core of the pellets indicated a pH increase of the solution in that direction and, consequently, a change in the Ni^{2+} coordination sphere. Towards the core, enH_2^{2+} became partially (enH^+) or totally deprotonated (*en*) due to its interaction with the basic Al_B-OH groups (eq. (6)). The deprotononated *en* species could then interact with Ni^{2+} to form $[Ni(en)_x(H_2O)_{6-2x}]^{2+}$ (eq. (15)):

$$[Ni(H_2O)_6]^{2+} + x\ en \longrightarrow [Ni(en)_x(H_2O)_{6-2x}]^{2+} + 2x\ H_2O \qquad (15)$$

Figure 3.5 (b) represents the position of the λ_2 band measured in the edge and in the center of the impregnated EnNi3pH4 pellet at certain times after impregnation.

After approximately 60 min of equilibration, bands λ_1 and λ_2 were measured at the same positions (397 and 654 nm) in the edges and in the core of the pellet, indicating the presence of $[Ni(H_2O)_6]^{2+}$, without interacting substantially with the support.

The impregnation process of sample EnNi3pH4 on γ-Al_2O_3 pellets followed the same trend observed in samples EnNi1 and EnNi2 (Figures 3.2 (a), (b) and 3.3 (a), (b)). Most likely, the impregnation of $[Ni(en)_x(H_2O)_{6-2x}]^{2+}$ (x = 1, 2) on γ-Al_2O_3 pellets occurs in two steps:

1) Imbibition: Ni^{2+} complexes move fast towards the core of the pellets due to capillary forces. It was measured that the Ni^{2+} molecular structure changed strongly during its transport towards the core because of the effect that both Al_B-OH and Al_A-OH have on the formation/cleavage of $[Ni(en)_x(H_2O)_{6-2x}]^{2+}$. However, grafting is not taking place since Ni^{2+} transport towards the core is very fast.

2) Equilibration: After 30 to 60 min, Ni^{2+} was uniformly distributed on the pellets with a different Ni^{2+} first coordination sphere compared to that of the solution, probably because labile H_2O ligands in $[Ni(en)(H_2O)_4]^{2+}$ or $[Ni(en)_2(H_2O)_2]^{2+}$ have been exchanged by one or two hydroxyl groups from alumina surface.

3.4. UV-Vis-NIR Micro-spectroscopy after Impregnation of Chlorinated Alumina Pellets

Figure 3.6 shows the space resolved UV-Vis-NIR spectra from the edge to the center of an Al_2O_3-AC pellet impregnated with solution EnNi1, 5 min after impregnation and 2 h of equilibration. 5 min after impregnation (Figure 3.6 (a)), Ni^{2+} was already present in the center of the pellet. The intensity of the absorption bands was lower in the core than in the edges and Ni^{2+} transport was slower than on non-treated alumina pellets. A change in the molecular structure of Ni^{2+} along the cross section of the pellet was also measured. In the edge, Ni^{2+} d-d bands λ_1 and λ_2 were measured at 385 and 633 nm. Band λ_3 was centered above 1100 nm with a shoulder at around 950 nm. This spectrum indicates the presence of mainly $[Ni(en)(H_2O)_4]^{2+}$ complexes; as if EnNi1 solution was impregnated on non treated alumina (Figure 3.2 (b)). In the center, the spectrum resembles that of $[Ni(H_2O)_6]^{2+}$ with bands λ_1 and λ_2 centered at 398 and 661 nm and the very characteristic spin forbidden band at around 730 nm with a similar intensity as λ_2. Band λ_3 was beyond the energy detection range.

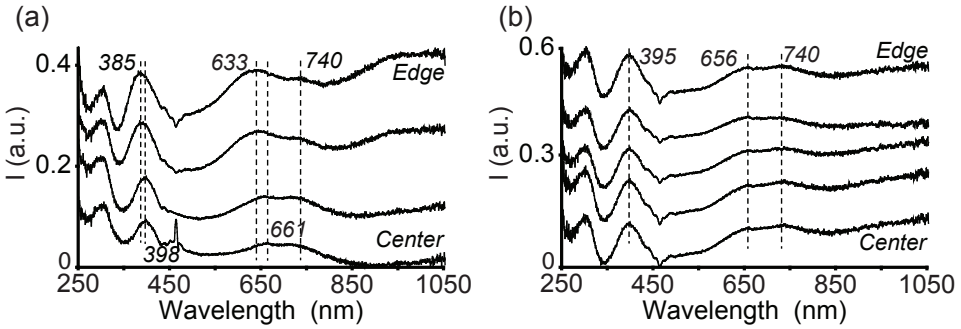

Figure 3.6. Space resolved UV-Vis-NIR spectra measured (a) 5 min after impregnation, and (b) 2 h after equilibration of EnNi1 solution on Al_2O_3-AC pellets.

The change in the Ni^{2+} molecular structure towards the core of the catalyst body was due to a decrease in the pH of the solution in that direction caused by fact that Al_2O_3-AC was an acidic support and the concentration of basic hydroxyl sites (Al_B-OH) was negligible (Figure 3.1). Towards the core, $[Ni(en)(H_2O)_4]^{2+}$ fell apart because of protonation of *en* molecules by Al_A-OH groups to form enH^+ and enH_2^{2+}, as shown in eq. (5). Since no Al_B-OH groups were present on the alumina surface, deprotonated *en* molecules could not be formed and the precursor complex could not be regenerated; i.e., the equilibria in eq. (6) and (7) did not occur.

The slow transport of Ni^{2+} towards the core, compared to its dynamics on non treated alumina, was also caused by the negative alumina surface charge compared to non treated alumina, where the surface charge was slightly positive at the pH of EnNi1 solution. After 2 h of equilibration (Figure 3.6 (b)), Ni^{2+} was measured along the cross section of Al_2O_3-AC pellets with a uniform concentration of $[Ni(H_2O)_6]^{2+}$ species (bands λ_1 and λ_2 at 395 and 656 nm). Clearly, $[Ni(H_2O)_6]^{2+}$ remained as the stable species throughout the support body.

4. Study of the Drying Step of $[Ni(en)_x(H_2O)_{6-2x}]^{2+}$/γ-$Al_2O_3$ Pellets

4.1. UV-Vis-NIR Micro-spectroscopy after Drying of the $[Ni(en)_x(H_2O)_{6-2x}]^{2+}$ /γ-Al_2O_3 Pellets

Figure 3.7 shows the space resolved UV-Vis-NIR spectra collected on the pellets impregnated with solutions EnNi0-EnNi3 after drying at 100 °C for 8 h. Different species were detected along the cross section of the alumina pellets as a function of the ratio *en*:Ni^{2+}. EnNi0 and EnNi1 dried pellets showed a uniform distribution of a single Ni^{2+} complex (Figures 3.7 (a) and (b)); whereas, EnNi2 and EnNi3 dried pellets presented a gradient of $[Ni(en)_x(H_2O)_{6-2x}]^{2+}$ species with the core of the pellets showing Ni-*en* species poorer in *en* than the edges (Figures 3.7 (c) and (d)).

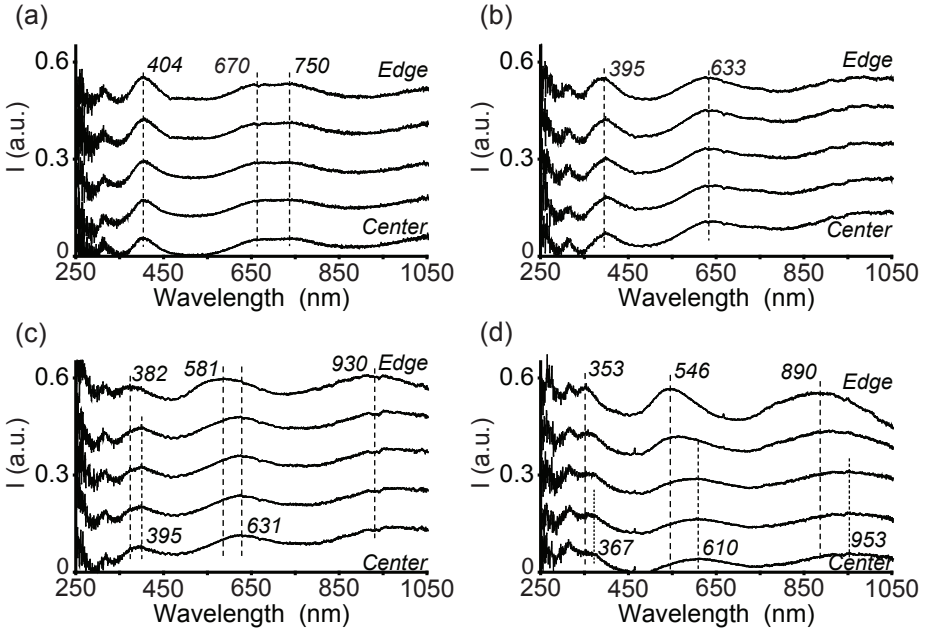

Figure 3.7. Space resolved UV-Vis-NIR spectra from the edge to the center of bisected pellets after drying: (a) EnNi0, (b) EnNi1, (c) EnNi2 and (d) EnNi3.

The EnNi0 dried pellet shows three bands at 404, 670 and 750 nm, the latter corresponds to the Ni^{2+} d-d spin forbidden band (Figure 3.7 (a)). These bands, which shifted to longer wavelengths compared to the solution and to the impregnated pellets, indicate an octahedral symmetry of Ni^{2+} where H_2O ligands most probably exchanged by surface hydroxyl groups. Moreover, Ni^{2+} was uniformly distributed inside the pellets. The EnNi1 dried pellet shows the Ni^{2+} d-d bands λ_1 and λ_2 at the same positions as 2 h after impregnation (Figure 3.7 (b)). These bands are probably due to the inner-sphere complexes $[(Al\text{-}O)_2Ni(en)(H_2O)_2]$ or $[Al\text{-}O\text{-}Ni(en)(H_2O)_3]^+$ that form during the impregnation step. In both samples, band λ_3 was beyond the energy detection limit of the set-up.

The EnNi2 and EnNi3 dried pellets show a gradual red-shift of the Ni^{2+} d-d bands from the edge to the center of the pellets (Figure 3.7 (c) and (d)). The Ni^{2+} d-d bands λ_1, λ_2 and λ_3 of the EnNi2 dried pellet were measured at 382, 581 and 930 nm close to the edge; and at 395, 631 and 980 nm in the core (Figure 3.7 (c)). Hence, drying induced Ni^{2+} speciation, and the core of the pellets contained Ni^{2+} complexed to less than two *en* molecules, as deduced from the position of Ni^{2+} d-d bands. The spectrum at this position was identical to that measured on the center of EnNi1 dried sample; i.e., Ni^{2+} contained in its coordination sphere one molecule of *en* and 1 or 2 oxygens from alumina hydroxyl groups. Moreover, the intensity of the absorption bands was very similar along the cross section of the pellets. Thus, it is difficult to say whether Ni^{2+} followed the same trend as *en* molecules or it was uniformly distributed inside the pellets.

On the dried EnNi3 sample (Figure 3.7 (d)), the Ni^{2+} d-d bands λ_1, λ_2 and λ_3 were measured at 353, 546 and 890 nm in the edges (indicative of the presence of $[Ni(en)_3]^{2+}$ complex) and at 367, 610 and 953 nm, in the core of the pellets. Hence, the core contained Ni^{2+} species complexed to less than three *en* molecules, where *en* was exchanged with hydroxyl groups of alumina. An important decrease in the intensity of the Ni^{2+} d-d transition bands was observed from edge to core. However, because of the different absorption coefficients of the $[Ni(en)_x(H_2O)_{6-2x}]^{2+}$ complexes it was difficult to quantitatively link the difference in intensity to a difference in Ni^{2+} concentration.

Figure 3.8 shows the distribution of Ni along a line scan on the pellets EnNi1 - EnNi3 measured with SEM-EDX. This measurement was not performed in EnNi0 dried pellets because the space resolved UV-Vis-NIR spectra on this sample (Figure 3.7 (a)) already show a uniform distribution of the metal-ion. In the three line scans,

the points obtained were rather scattered due to the roughness of the cross sections. The overall Ni^{2+} content measured was around the intake of 3 % wt. A rather uniform Ni concentration was measured on the EnNi1 dried pellet (Figure 3.8 (a)). In the samples EnNi2 and EnNi3 (Figure 3.8 (b) and (c)), the Ni^{2+} content was above 3 % wt at the edges and, in the center, below this value. Thus, there was a tendency towards Ni^{2+} egg-shell distributions with increasing the *en*:Ni^{2+} ratio.

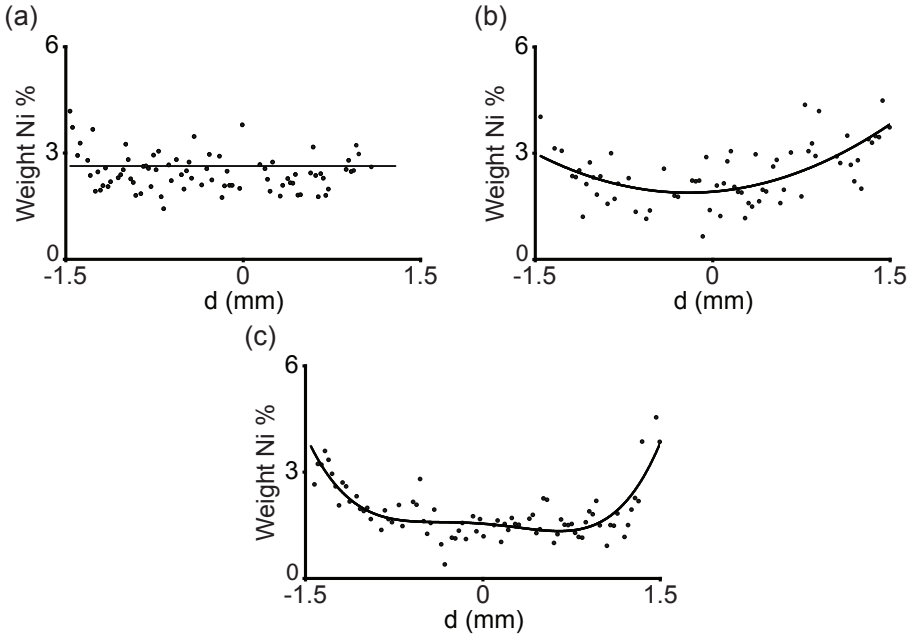

Figure 3.8. Ni profiles after drying measured by SEM-EDX: (a) EnNi1, (b) EnNi2 and (c) EnNi3.

Combining the UV-Vis-NIR data after drying (Figure 3.7) with the Ni^{2+} profiles measured with EDX (Figure 3.8), it can already be claimed that the different profiles of the Ni precursor complexes observed after drying can only be explained by assuming a specific interaction between alumina surface and the Ni complexes which contained H_2O as part of their 1st coordination sphere, via grafting (exchange of water ligands with surface OH groups) before drying. During drying $[Ni(en)_3]^{2+}$ complex is transported together with the solvent, towards the outer surface of the pellets due to the absence of interactions between this complex and alumina in

the impregnation step (Figure 3.3 (d)). On the other hand, when the impregnation solution contains $[Ni(H_2O)_6]^{2+}$ or $[Ni(en)(H_2O)_4]^{2+}$ the transport of Ni^{2+} towards the outer surface during the drying step is not possible (Figures 3.3 and 3.7, (a) and (b)), due to the stronger interactions between these complexes and the support that started taking place after impregnation, as proposed in eq. (9) – (14).

4.2. IR Micro-spectroscopy after Drying of the $[Ni(en)_x(H_2O)_{6-2x}]^{2+}/\gamma$-$Al_2O_3$ Pellets

The distribution of the chelating ligand, *en*, was monitored with IR micro-spectroscopy. Figure 3.9 shows the space resolved IR spectra between 3500 and 2500 cm^{-1} measured from the edge to the core of the EnNi1-EnNi3 dried pellets. In this region, all the samples show several absorption bands, more or less intense: a doublet at around 2940 and 2890 cm^{-1} typical of C-H stretching vibrations and two bands at around 3330 and 3284 cm^{-1} characteristic of N-H_2 stretching vibrations (the latter observed only in sample EnNi3, Figure 3.9 (c)) from the *en* ligands complexing Ni^{2+} in an octahedral symmetry.[19]

The dried EnNi1 sample (Figure 3.9 (a)) shows the two bands at 2944 and 2894 cm^{-1} characteristic of C-H stretching vibrations in a rather even distribution along the cross-section of the pellet. These bands indicate a uniform profile of the *en* groups on the support agreeing with the uniform distribution of $[Ni(en)(H_2O)_{4-x}(Al\text{-}O)_x]^{+2-x}$ (x = 1 or 2) species proposed from the UV-Vis-NIR data (Figure 3.7 (b)).

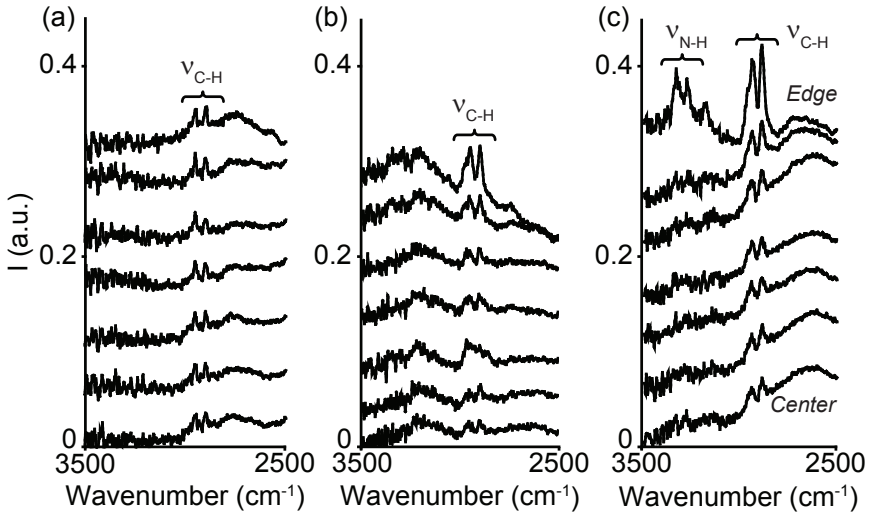

Figure 3.9. Space resolved IR spectra collected from the edge to the center of dried bisected pellets in the 3500-2500 cm^{-1} region: (a) EnNi1, (b) EnNi2 and (c) EnNi3.

An egg-shell distribution of *en*, as deduced from the intensity the C-H stretching vibrations at 2940 and 2892 cm^{-1}, was measured in the dried EnNi2 pellets (Figure 3.9 (b)). The similar intensity of the bands in the dried EnNi1 and EnNi2 samples suggests that the concentration of *en* species in the core of the pellets was the same in both samples, in line with what was observed with UV-Vis-NIR (Figure 3.7 (b) and (c)). The EnNi3 dried pellet (Figure 3.9 (c)) also exhibits an egg-shell distribution of *en* ligands with the C-H stretching vibrations at 2936 and 2892 cm^{-1} and the N-H stretching vibrations at 3338 and 3282 cm^{-1} being more intense in the edges than towards the core of the pellet. The latter bands were not observed in samples EnNi1 and EnNi2 probably because of the lower concentration of *en* ligands compared to sample EnNi3.

4.3. Diffuse Reflectance NIR on Crushed $[Ni(en)_x(H_2O)_{6-2x}]^{2+}$/γ-$Al_2O_3$ Pellets

Figure 3.10 shows the NIR spectra in the region between 1300 and 1600 nm on crushed EnNi0-EnNi3 pellets after drying. The spectra in this region consisted of several bands due to: (i) first υ(OH) overtones of basic, neutral and acidic surface

hydroxyl groups at 1388, 1425 and 1446 nm, respectively and (ii) first υ(NH) overtones of *en* molecules at around 1531 and 1542 nm.[8, 9]

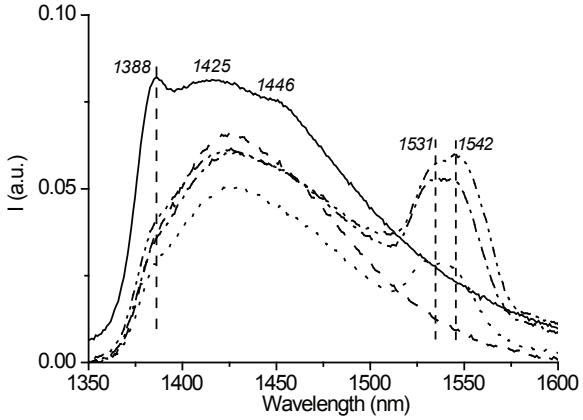

Figure 3.10. NIR spectra of dried and crushed pellets: EnNi0 (– –), EnNi1 (·····), EnNi2 (— · —) and EnNi3(— · · —). The NIR spectrum of γ-Al_2O_3 is shown as a reference (—).

These spectra show an increase in intensity of the NH_2 overtone band from *en*, with increasing ratio *en*:Ni^{2+}. Thus, the overall molar ratios from the precursor solutions were kept after drying at 100 °C. Moreover, a consumption of mainly the basic alumina surface hydroxyl groups in all the samples can be observed, with respect to the γ-Al_2O_3 support. This information supports the proposed grafting mechanism of interaction, 2 h after impregnation, between $[Ni(en)_x(H_2O)_{6-2x}]^{2+}$ (x = 0 - 2) precursor complexes and the alumina hydroxyl surface.

4.4. Effect of the Drying Temperature on the EnNi3/γ-Al_2O_3 Pellets

The effect of the drying temperature on the EnNi3 pellets was studied and the dried pellets were characterized by UV-Vis-NIR micro-spectroscopy. Figure 3.11 (a) represents the difference (in wavelengths) between the position of the λ_2 band measured in the center and in the edge of the pellets ($\Delta\lambda_2 = \lambda_2^{center} - \lambda_2^{edge}$) as a function of the drying temperature.

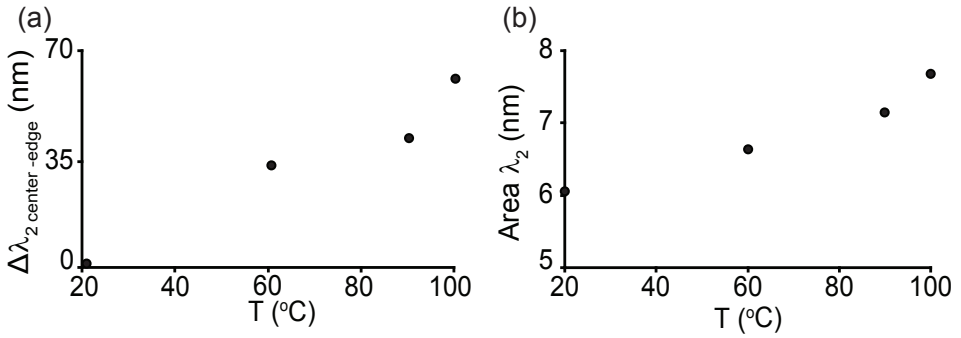

Figure 3.11. (a) Difference in the position of band λ_2, between the center and the edge, in the dried EnNi3 pellets as a function of the drying temperature. (b) Area of band λ_2 measured at the edges of the impregnated EnNi3 pellets dried at different temperatures.

The pellets dried at RT showed a uniform purple color along the scanned area with the three Ni^{2+} d-d absorption bands at the same positions as for the impregnated EnNi3 pellets after 2 h, denoting that the complex $[Ni(en)_3]^{2+}$ remained unchanged and uniformly distributed inside the pellet; i.e., the drying step did not have an influence on the nature or distribution of the active component.

When the drying temperature was increased to 60 °C or above, the space resolved UV-Vis-NIR spectra along the cross section of the dried pellets showed a gradual change of the bands. The spectra measured in the edge of the pellets dried at 60, 90 and 100 °C were very similar to that of the impregnated pellets after 2 h, with the three Ni^{2+} d-d bands characteristic of $[Ni(en)_3]^{2+}$ species. In the center of the pellet, the spectra suffered a red shift of the bands, indicative of the presence of species with lower concentration of *en* groups bonded to the Ni^{2+} ion. As it is concluded from Figure 3.11 (a), the red shift of the λ_2 band in the center of the pellets increased with the drying temperature; i.e., the higher the drying temperature, the poorer the core in *en* molecules.

A semi-quantitative analysis of the amount of $[Ni(en)_3]^{2+}$ complex at the edges of the pellets as a function of the drying temperature was performed and represented in Figure 3.11 (b). In this figure, the area under the λ_2 band measured in the edge of the dried pellets is given versus the drying temperature. The plot shows that the concentration of $[Ni(en)_3]^{2+}$ in the edges increases with increasing drying temperature; i.e., higher drying temperatures induce a more substantial transport of $[Ni(en)_3]^{2+}$ towards the external surface of the pellets. However, $[Ni(en)_3]^{2+}$ that

remained behind decomposed and *en* molecules were partially substituted by surface OH groups.

Conclusions

Even though no interactions are expected between the $[Ni(en)_x(H_2O)_{6-2x}]^{2+}$ (x = 0 - 3) complexes and the positively charged alumina surface at pH values of the solutions below or close to the pzc of the support, UV-Vis-NIR micro-spectroscopy has revealed a strong influence of the alumina surface on the molecular structure of Ni^{2+} during the first hour after impregnation, when *en*:Ni^{2+} = 1 or 2. The experiments described in this Chapter prove that the different alumina surface hydroxyl groups play a role on the dynamics and interactions of the precursor metal-ion complexes within the support surface. In particular, even though the acidic hydroxyl groups of alumina enhance the breakdown of the precursor complexes, these can be regenerated by the action of basic hydroxyls from the support surface.

Furthermore, the number of *en* ligands surrounding Ni^{2+} determines the strength of interactions between this and the support surface; in this way, the higher the molar ratio *en*:Ni^{2+}, the weaker the interactions of the metal-ion complex with the alumina surface during the impregnation step. Hence, the adsorption of $[Ni(en)_x(H_2O)_{6-2x}]^{2+}$ onto alumina surface, before drying, was responsible for the Ni^{2+} macro-distribution (and molecular structure) in the pellets after drying; i.e., the stronger the adsorption to the surface after impregnation, the more uniform the Ni^{2+} distribution appeared to be after drying. Therefore, the use of chelating ligands such as ethylenediamine in pre-shaped catalyst preparation not only influences the molecular interactions with the support, but also the final macro-distribution of the active species. This additional ingredient enables the preparation of either uniform or egg-shell Ni catalysts by controlling the *en*:Ni^{2+} ratios used in the precursor solutions.

Acknowledgments

Marjan Versluijs-Helder, Dr. Tom Visser and Dr. Alwies van der Heijden (Inorganic Chemistry and Catalysis group, Utrecht University) are kindly thanked for their help in carrying out SEM-EDX analyses, IR micro-spectroscopy and the preparation of modified alumina, respectively. Ad Mens (Inorganic Chemistry

and Catalysis group, Utrecht University) is thanked for the N_2 physisorption measurements on the γ-Al_2O_3 support.

References

[1] F. Negrier, E. Marceau, M. Che, *Chem. Comm.* **2002**, 1194.
[2] J. Ryczkowski, *React. Kinet. Catal. Lett.* **1989**, *40*, 189.
[3] A. J. van Dillen, R. J. A. M. Terörde, D. J. Lensveld, J. W. Geus, K. P. de Jong, *J. Catal.* **2003**, *216*, 257.
[4] J. Park, J. R. Regalbuto, *J. Colloid Interface Sci.* **1995**, *175*, 239.
[5] L. G. van de Water, J. A. Bergwerff, T. A. Nijhuis, K. P. de Jong, B. M. Weckhuysen, *J. Am. Chem. Soc.* **2005**, *127*, 5024.
[6] P. Paoletti, *Pure Appl. Chem.* **1984**, *56*, 491.
[7] A. B. P. Lever, *Inorganic Electronic Spectroscopy*, Elsevier Science B. V., Amsterdam, **1987**.
[8] K. Elkabouss, M. Kacimi, M. Ziyad, S. Ammar, F. Bozon-Verduraz, *J. Catal.* **2004**, *226*, 16.
[9] C. Flego, W. O. N. ParkerJr, *Appl. Catal. A: General* **1999**, *185*, 137.
[10] K. Bourikas, C. Kordulis, A. Lycourghiotis, *Catal. Rev. Sci. Eng.* **2006**, *48*, 363.
[11] M. Sun, D. Nicosia, R. Prins, *Catal. Today* **2003**, *86*, 173.
[12] J.-P. Jolivet, *Metal Oxide Chemistry and Synthesis*, John Wiley & Sons Ltd., Chichester, **2000**.
[13] H. Vigué, P. Quintard, T. Merle-Méjean, V. Lorenzelli, *J. Eur. Cer. Soc.* **1998**, *18*, 305.
[14] J. Korah, W. A. Spieker, J. R. Regalbuto, *Catal. Lett.* **2003**, *85*, 123.
[15] J. A. Mieth, J. A. Schwarz, Y. J. Huang, S. C. Fung, *J. Catal.* **1990**, *122*, 202.
[16] J. R. Regalbuto, A. Navada, S. Shadid, M. L. Bricker, Q. Chen, *J. Catal.* **1999**, *184*, 335.
[17] P. K. de Bokx, W. B. A. Wassenberg, J. W. Geus, *J. Catal.* **1987**, *104*, 86.
[18] J.-F. Lambert, M. Hoogland, M. Che, *J. Phys. Chem. B* **1997**, *101*, 10347.
[19] S. P. Roe, J. O. Hill, R. J. Magee, *Monatsh. Chem.* **1991**, *122*, 467.

Chapter 4

Magnetic Resonance Imaging to Study the Impregnation Step of Paramagnetic Ni^{2+} Complexes on γ-Al_2O_3 Support Bodies

Abstract

Magnetic Resonance Imaging (MRI) has been used to study the impregnation step during the preparation of Ni/γ-Al_2O_3 hydrogenation catalysts with Ni^{2+} metal-ions present in different coordinations. The precursor complexes were $[Ni(H_2O)_6]^{2+}$ and $[Ni(edtaH_x)]^{(2-x)-}$ (where x = 0, 1, 2 and *edta* = ethylenediaminetetraacetic acid), representing a non-shielded and a shielded paramagnetic complex, respectively. Due to the different shielding effect of the ligands, the dynamics of $[Ni(H_2O)_6]^{2+}$ or $[Ni(edtaH_x)]^{(2-x)-}$ were visualized applying T_2 or T_1 image contrast, respectively. MRI was applied in a quantitative manner to calculate the $[Ni(H_2O)_6]^{2+}$ concentration distribution after impregnation when it was present alone in the impregnation solution, or together with the $[Ni(edtaH_x)]^{(2-x)-}$ species. Moreover, the combination of MRI with UV-Vis-NIR micro-spectroscopy allowed the visualization of both species with complementary information on the dynamics and adsorption/desorption phenomena within γ-Al_2O_3 support bodies. These phenomena yielded non-uniform Ni distributions after impregnation, which are interesting for certain industrial applications.

Introduction

Chapters 2 and 3 have demonstrated some applications of invasive techniques such as UV-Vis-NIR and IR micro-spectroscopies to study the impregnation and drying steps of γ-Al_2O_3 catalyst bodies. More specifically, they have been used to monitor the dynamics of Ni^{2+} and Pd^{II} precursor complexes, and to gain insight into the influence that additional ingredients such as chelating agents or inorganic salts have on both the molecular structure and dynamics of these metal-ions.

As mentioned in Chapter 1, the development of noninvasive techniques which allow to study the samples in situ; i.e. during the different preparation steps, is of particular interest; and Magnetic Resonance Imaging (MRI) serves as an example of such noninvasive techniques.[1-5] The contrast or brightness in an NMR (nuclear magnetic resonance) image is a direct measure of the NMR signal intensity of water protons. This signal intensity can be made to depend on the proton nuclear spin relaxation times.[6-9] With the aid of MRI, the distribution and transport of complexes of paramagnetic transition metal-ions inside a catalyst body upon their impregnation can be deduced by monitoring the ^1H NMR signal of the water solvent inside the catalyst body.[1, 2, 10]

In the experiments described in this Chapter, the ^1H MRI-based method reported earlier[1] is applied to monitor and quantify the transport of $[Ni(H_2O)_6]^{2+}$ on γ-Al_2O_3 support bodies. This investigation illustrates the general validity of the method. Moreover, MRI has also been used to follow the transport of other Ni^{2+} complexes, *viz*. $[Ni(edtaH_x)]^{(2-x)-}$ (x = 0, 1, 2 *edta* = ethylenediaminetetraacetic acid). The bulky *edta* ligand shields the paramagnetic effect of Ni^{2+} on the ^1H NMR signal and in this case a different experimental protocol is required to visualize Ni^{2+}. In this way, the combination of MRI with UV-Vis-NIR micro-spectroscopy enables us to discriminate $[Ni(H_2O)_6]^{2+}$ from $[Ni(edtaH_x)]^{(2-x)-}$ when both complexes are present in the impregnation solution, and $[Ni(H_2O)_6]^{2+}$ transport can then be monitored in the presence of $[Ni(edtaH_x)]^{(2-x)-}$.

Experimental Section

1. Preparation of the Impregnation Solutions

To quantify the dynamics of $[Ni(H_2O)_6]^{2+}$ inside a support body after its impregnation, several $[Ni(H_2O)_6]^{2+}$ solutions were prepared with concentrations ranging from 0.1 M to 1.0 M by dissolving the required amounts of $Ni(NO_3)_2 \cdot 6\ H_2O$ (Acros, p.a.) in de-ionized water.

Ni-*edta* solutions in a 1:1 molar ratio were prepared with 0.1 M $Ni(NO_3)_2 \cdot 6\ H_2O$ (Acros, p.a.) and 0.1 M *edta* precursor (*edta* = ethylenediaminetetraacetic acid, Acros, p.a.) at pH 1 and 7. *Edta*-disodium precursor salt was used to achieve pH 1, and *edta*-tetrasodium precursor salt was used to obtain pH 7. These Ni-*edta* solutions will be referred to as Ni*edta*1:1pH1 and Ni*edta*1:1pH7. Two other Ni-*edta* solutions with a molar ratio Ni^{2+}:*edta* = 6:1 were prepared by slowly adding *edta*-disodium salt or *edta*-tetrasodium salt to an aqueous solution of $Ni(NO_3)_2 \cdot 6\ H_2O$. The final pH of these solutions were 1 (solution Ni*edta*6:1pH1) and 6 (solution Ni*edta*6:1pH6), respectively. The latter solution was not stable with time and a fresh solution was prepared for each experiment. Table 4.1 summarizes the composition and speciation of the Ni-*edta* solutions. The speciation of the Ni-*edta* complexes in solution, as a function of pH, was determined by using multivariate curve resolution analysis (MCR) of the UV-Vis spectra of the solutions. Information on the procedure followed to determine the speciation can be found in Appendix B.

UV-Vis spectra of the impregnation solutions were recorded between 450 and 850 nm with a Varian Cary 50 UV-Vis spectrophotometer. Diffuse reflectance UV-Vis-NIR spectra of impregnated catalyst bodies were acquired between 250 and 1050 nm using the home-built set-up illustrated in Appendix A.[13] All UV-Vis-NIR measurements of the impregnated catalyst bodies were performed along a scan-line through the resulting surface of the extrudates after bisection with a scalpel, as illustrated in Figure 1.3 in Chapter 1. Twelve spectra were collected along the diameter of the bisected extrudates. The spatial resolution was 320 μm and 5 min were required to collect the spectra along the line scan.

Table 4.1. Composition of the Ni-*edta* impregnation solutions and speciation of the Ni^{2+} complexes (as determined from UV-Vis spectroscopy, Appendix B).

Solution	[Ni] /M	[*edta*] /M	Calculated concentrations of the species present*
Ni*edta*1:1pH1	0.1	0.1	0.05 M $[Ni(edtaH)]^-$ 0.05 M $[Ni(edtaH_2)]$
Ni*edta*1:1pH7	0.1	0.1	0.1 M $[Ni(edta)]^{2-}$
Ni*edta*6:1pH1	0.6	0.1	0.50 M $[Ni(H_2O)_6]^{2+}$ 0.07 M $[Ni(edtaH)]^-$ 0.03 M $[Ni(edtaH_2)]$
Ni*edta*6:1pH6	0.6	0.1	0.49 M $[Ni(H_2O)_6]^{2+}$ 0.11 M $[Ni(edta)]^{2-}$

* The protons in $[Ni(edtaH_x)]^{(2-x)-}$ (x = 1, 2) are forming carboxyl groups.[11, 12]

2. Catalyst Preparation

γ-Al_2O_3 extrudates (12 mm long and 3.85 mm in diameter) with a BET surface area of 145 $m^2 \cdot g^{-1}$ and a pore volume of 0.36 mL $\cdot$ g^{-1}, as determined from N_2 physisorption, were used. The point of zero charge (pzc) of the γ-Al_2O_3 extrudates was 7.9, as determined by mass titration.[14] Pore volume impregnation of single γ-Al_2O_3 extrudates was done drop-wise along the extrudate, making sure that the entire extrudate was wetted. The volume added for impregnation of a single extrudate was equal to the pore volume plus 10 %. Thus, the average volume used for a single extrudate was 90-100µl, depending on the weight of the extrudate. This volume was added in drops of approximately 30 µl. After adding all the drops, the vial with the extrudate was shaken for 30 s and the remaining liquid (10 % of the volume added) was removed with a pipette. The volume inside the extrudate was, therefore, equal to the pore volume of the support. This means that the average concentration of Ni^{2+} inside the extrudate was constant during each MRI experiment and directly determined by the Ni^{2+} concentration of the impregnation solution.

3. MRI Experiments

Immediately after pore volume impregnation, the extrudates were placed inside an NMR tube. A wet tissue was inserted in the NMR tube to avoid drying of the extrudates during the measurements.

The NMR/MRI experiments were performed using a Bruker Avance DRX 300 (300 MHz) wide-bore spectrometer equipped with imaging accessories. The acquisition of two-dimensional (2D) cross-sectional images was based on the detection of the ^{1}H NMR signal of water in the impregnated extrudates with a two-pulse spin-echo sequence shown schematically in Figure 4.1. Two radiofrequency (RF) pulses with 90° and 180° flip angles were applied during the sequence. G_f and G_ϕ refer to the magnetic field gradients applied in the *x* direction (G_f, frequency encoding) and in the *y* direction (G_ϕ, phase encoding). In the *z* direction, slice selection was applied (G_s), and the signal recorded corresponded to a 2-mm slice in the center of the extrudates detected transverse to the sample axis. The echo time (TE) and repetition time (TR) are also shown in Figure 4.1. A detailed description on the fundamentals of MRI can be found elsewhere.[7, 15, 16]

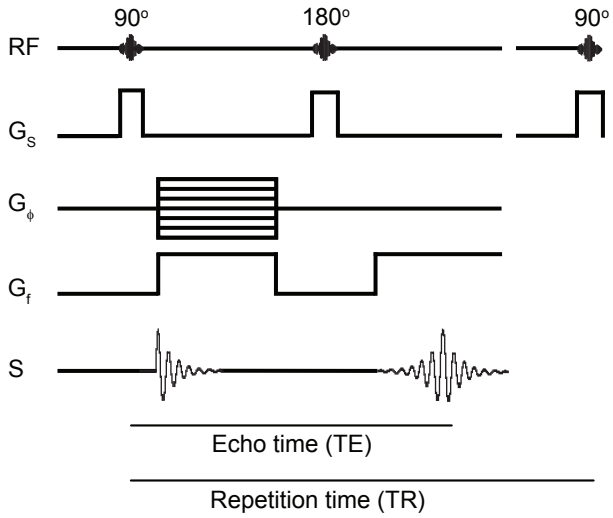

Figure 4.1. Timing diagram of a two-pulse spin-echo sequence. The echo time and the repetition time are also indicated. S indicates when the signal appears in the sequence.

Images were collected imposing either T_1 contrast or T_2 contrast. The echo time was fixed at TE = 1 ms. To obtain T_1-weighted images (T_1 contrast), TR was set to 100 ms. This value is in between the T_1 values of the two aqueous components in

the sample (pure water and water in the presence of the Ni^{2+} complex). To obtain T_2-weighted images (T_2 contrast), the TR was 1 s, which was longer than the T_1 values of the two components. Table 4.2 summarizes the experimental parameters, TR and TE, and the contrast obtained in all the MRI experiments. Acquisition time of an image was 4.5 min (TR = 1 s) or 30 s (TR = 100 ms) and the spatial resolution in the image plane was 140 μm by 230 μm.

Table 4.2. Summary of the experimental parameters used for detection of the NMR images and type of image contrast obtained.

Solution	[Ni] /M	[Ni]:[*edta*]	TR /ms	TE /ms	Contrast
$[Ni(H_2O)_6]^{2+}$	0.1-1.0	0	1000	1	T_2
Ni*edta*1:1	0.1	1	100	1	T_1
Ni*edta*6:1	0.6	6	1000	1	T_2

4. NMR Relaxation Time Experiments

Relaxation time measurements for all Ni^{2+} solutions saturating the pores of alumina extrudates were performed to determine the spin-lattice (T_1) and the spin-spin (T_2) relaxation times of water protons in the presence of Ni^{2+}. Inversion-recovery experiments were carried out to measure T_1, and Carr-Purcell-Meiboom-Gill (CPMG) experiments were conducted to measure T_2.[15] The relaxation times relevant to the following discussion are summarized in Table 4.3.

Table 4.3. Relaxation times T_1 and T_2 of water in the pores of alumina extrudates in the presence of different Ni^{2+} complexes, and magnetization values*:

Solution	T_1 /ms	T_2 /ms	M_{T1}^{1s}	M_{T1}^{100ms}	M_{T2}	I/I_o^{1s}	$I/I_o^{100\ ms}$
H_2O	216.9	3.86	0.99	0.37	0.77	0.76	0.28
Ni*edta*1:1pH7	15.98	2.67	1.00	1.00	0.69	0.69	0.69
$[Ni(H_2O)_6]^{2+}$ 0.1 M	11.05	2.11	1.00	1.00	0.62	0.62	0.62

* $I/I_o = M_{T1} * M_{T2}$, where $M_{T1} = [1-\exp(-TR/T_1)]$ and $M_{T2} = [\exp(-TE/T_2)]$.

Results and Discussion

1. Dynamics of $[Ni(H_2O)_6]^{2+}$ within γ-Al_2O_3 Support Bodies Based on T_2 Contrast

Figure 4.2 (a) shows the T_2-weighted images of extrudates impregnated with aqueous solutions with various Ni^{2+} concentrations after equilibration for 12 h. An image of an extrudate impregnated with water is also shown. In all cases, the images show a spatially uniform NMR signal and, therefore, a uniform macro-distribution of $[Ni(H_2O)_6]^{2+}$ in the extrudates. The relaxation of water protons is progressively enhanced with increasing concentration of paramagnetic species. In other words, a low NMR signal intensity corresponds to a high Ni^{2+} concentration (red color); whereas a high NMR signal intensity indicates a low Ni^{2+} concentration (blue color). This is because an increase in the T_2 time corresponds to an increase in the NMR signal intensity (see expression for M_{T2} in the footnote of Table 4.3).

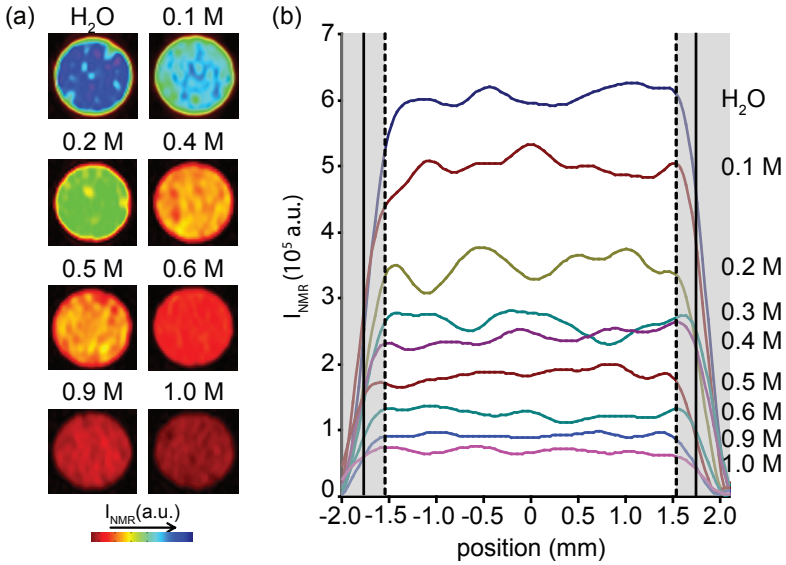

Figure 4.2. (a) T_2-weighted images of the extrudates 12 h after impregnation with aqueous Ni^{2+} solutions containing different concentrations of $[Ni(H_2O)_6]^{2+}$. (b) 1D signal intensity profiles in arbitrary units (a.u.), as a function of the position inside the extrudates for different $[Ni(H_2O)_6]^{2+}$ concentrations. The grey areas indicate the regions excluded from quantitative data analysis.

One-dimensional (1D) ^1H NMR signal intensity profiles (in arbitrary units, a.u.), along a scan-line of the catalyst body, are shown in Figure 4.2 (b). The edges of the extrudates are marked as thick black vertical lines in the figure. The NMR signal in the edges does not show an abrupt signal change from a maximum value (inside the extrudates) to zero (outside the extrudates). This is due to the limited spatial resolution and smoothing of the NMR images for a better presentation. Consequently, extrudates boundaries appear smooth, with a gradual signal variation at the extrudates edges. This gradual signal variation corresponds to the grey regions in the figure. Moreover, smoothing of the inner extrudates regions does not lead to signal variations as the signal intensity is independent of position in the inner regions, but helps to average out noise and sample heterogeneities. Due to smoothing, the boundaries of the extrudates represented in grey color are excluded from data analysis, and only the data points from position -1.58 mm to 1.58 mm will be considered for data analysis, and depicted in the subsequent 1D profiles in Figures 4.3 – 4.7 (NMR signal profiles or concentration profiles).

The 1D signal intensity profiles show how the ^{1}H NMR signal decreases with increasing Ni^{2+} concentration. These profiles are not totally flat due to noise in the experimental measurements and the heterogeneities in alumina structure.[17] To have an idea of the uncertainty of the measurements, an additional experiment was performed. In this experiment, four different extrudates were impregnated with water and the measured 1D signal intensity profiles were averaged. The resulting relative standard deviation was calculated to be 4 %. This value was taken as a basis for the measurement error.

The average NMR signal intensity along a scan-line of the Ni^{2+}-impregnated extrudates, calculated from the 1D profiles illustrated in Figure 4.2, versus the Ni^{2+} concentration in the impregnation solution yielded the following exponential dependence ($R^2 = 0.99$):

$$I_{NMR} = 50270 + 569106 \cdot \exp(-[Ni^{2+}]/0.332) \quad (1)$$

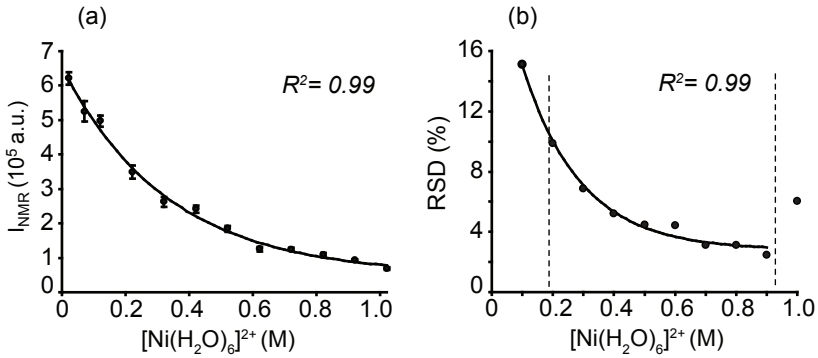

Figure 4.3. (a) Calibration curve that relates the $[Ni(H_2O)_6]^{2+}$ concentration in the impregnation solutions and the ^{1}H NMR signal intensity of water protons (in arbitrary units, a.u.) in the catalyst bodies; and (b) relative standard deviation of the calculated $[Ni(H_2O)_6]^{2+}$ concentrations as a function of the concentration in the impregnation solutions.

This exponential dependence is represented in Figure 4.3 (a). The average NMR signal values in the plot are represented together with their standard deviation (SD), which give an idea of the experimental uncertainty associated with the measurement procedure and the heterogeneities of the alumina pore structure.

The exponential decrease of the NMR signal intensity with increasing Ni^{2+} concentrations can be explained as follows. It is known that the NMR signal intensity

of protons measured in an MRI experiment using a two-pulse spin-echo sequence is described by the following equation:[9]

$$I_{NMR} = I_o [1-\exp(-TR/T_1)] [\exp(-TE/T_2)] \quad (2)$$

The repetition time, TR, used to measure the average I_{NMR} in the equilibrated extrudates with different $[Ni(H_2O)_6]^{2+}$ concentrations was long enough (1 s) and the multiplier related to T_1 relaxation processes was approximately 1 in all cases. Therefore, the NMR signal, I_{NMR}, was only dependent on the T_2 relaxation time:

$$I_{NMR} = I_o [\exp(-TE/T_2)] \quad (3)$$

In pure liquids, the relaxation rates (T_i^{-1}, i = 1, 2) of water protons are linearly dependent on the concentration of paramagnetic species ([M]):[8]

$$(1/T_i)_{obs} = (1/T_i)_d + R_i[M] \quad (4)$$

The combination of eq. (3) and (4) yields an exponential dependence between the NMR signal intensity and the concentration of paramagnetic species ($[Ni(H_2O)_6]^{2+}$). There is an extra constant term on the right-hand side of eq. (1) as compared to eq. (3); i.e., the constant value "50270". This term characterizes the detection limit of the NMR experiment: the relaxation times of protons when Ni^{2+} concentration is above 0.9 M are very low, and NMR signals have such a low intensity that they cannot be detected reliably in the presence of the measurement noise.

Figure 4.4 shows the linear dependence between the relaxation rates (T_2^{-1}) of the water protons in the catalyst bodies and the Ni^{2+} concentrations in the impregnation solutions (eq. (4)). This linear dependence points out that Ni^{2+} paramagnetic species had a qualitatively similar effect on the relaxation times of protons inside the pores of alumina as in pure liquids.

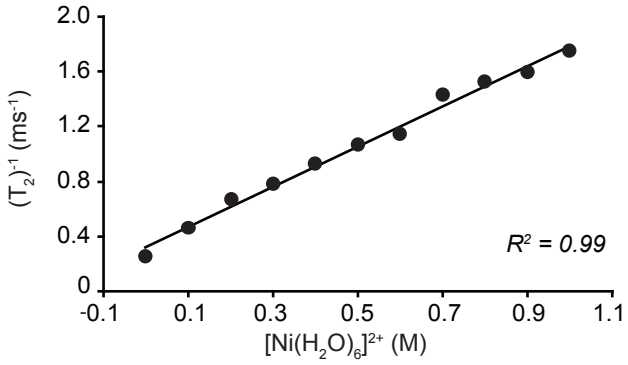

Figure 4.4. Linear dependence of the spin-spin relaxation rate (T_2^{-1}) of water protons within the equilibrated catalyst bodies on the $[Ni(H_2O)_6]^{2+}$ concentration in the impregnation solutions.

The slope of the line depicted in Figure 4.4 indicates the relaxivity (R_i) of water protons in the presence of $Ni(H_2O)_6^{2+}$ paramagnetic complex and characterizes the efficiency of the relaxation enhancement of water protons by a certain metal-ion complex. The *y*-intercept represents the solvent relaxation rate in the absence of paramagnetic ions ($(1/T_i)_d$).

Figure 4.5 illustrates the 1D $[Ni(H_2O)_6]^{2+}$ concentration profiles inside an extrudate as a function of time after pore volume impregnation obtained after applying the calibration curve, eq. (1), to the 1D signal intensity profiles measured. The impregnation solution contained 0.5 M $Ni(NO_3)_2$. The T_2-weighted images of the extrudate after impregnation with this solution are also depicted in this figure. The red regions indicate high Ni^{2+} concentrations and the blue regions correspond to low Ni^{2+} concentrations.

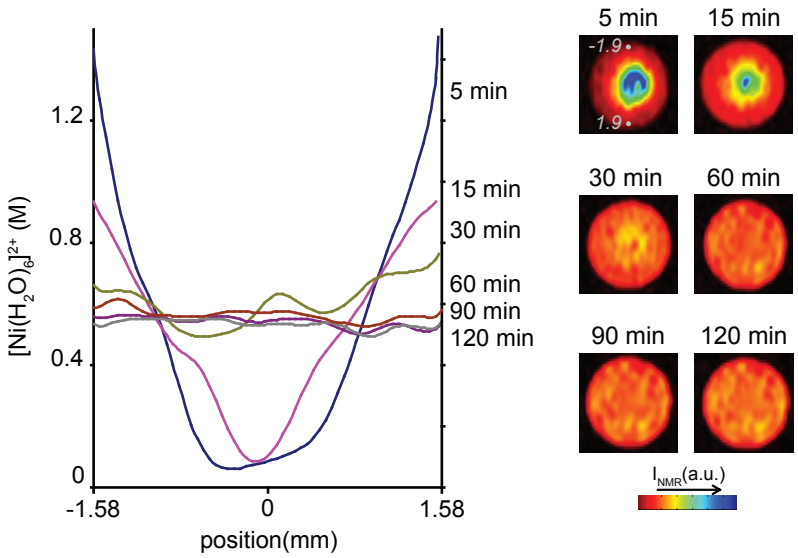

Figure 4.5. 1D profiles of the $[Ni(H_2O)_6]^{2+}$ concentration as a function of the position inside the extrudates at certain times after impregnation, together with the recorded T_2-weighted images.

As illustrated in Figure 4.5, at the edges of the extrudate 5 min after impregnation, the $[Ni(H_2O)_6]^{2+}$ concentration was higher than 0.5 M, while in the center there was no Ni present. During the pore volume impregnation, three main phenomena occur: capillary flow of the solution towards the core of the extrudate, diffusion of the metal-ion in the pores filled with water, and its adsorption on the walls of the pores.[18, 19] The fact that $[Ni(H_2O)_6]^{2+}$ ions do not move towards the core of the catalyst body together with the capillary flow of water molecules, and that a concentration gradient is observed 5 min after impregnation, suggests that there are interactions of this complex with the pore walls of the alumina extrudate. Moreover, these interactions cannot be electrostatic since the slightly acidic pH of the $[Ni(H_2O)_6]^{2+}$ solution below the pzc of γ-Al_2O_3 creates a positively charged alumina surface. These interactions are responsible for the $[Ni(H_2O)_6]^{2+}$ concentration gradient, and, therefore, the transport of $[Ni(H_2O)_6]^{2+}$ towards the core takes place according to liquid phase diffusion and adsorption/desorption phenomena on the pore walls. A uniform distribution of 0.53 M $[Ni(H_2O)_6]^{2+}$ was achieved 60 min after impregnation, which agreed with the concentration of the impregnation solution. This calculated concentration was within the range of the expected uncertainty (4 - 10 %, see Figure

4.3). Moreover, the time needed to get a uniform distribution of $[Ni(H_2O)_6]^{2+}$ was in line with liquid phase diffusion of the $Ni(NO_3)_2$ salt in bulk solution for a distance of 1.93 mm (radius of the γ-Al_2O_3 extrudate) which indicates that the adsorption of $[Ni(H_2O)_6]^{2+}$ on alumina surface is limited.[19, 20]

Recently, an MRI study was performed on the quantification of $[Co(H_2O)_6]^{2+}$ transport after impregnation of similar γ-Al_2O_3 extrudates.[1] The range of concentrations that could be calibrated for $[Co(H_2O)_6]^{2+}$ was limited to a maximum value of 0.5 M, while $[Ni(H_2O)_6]^{2+}$ was calibrated up to 0.9 M, with 10 % uncertainty. This difference is due to the paramagnetic properties of the two ions, with $[Co(H_2O)_6]^{2+}$ having a stronger paramagnetic effect on water protons and enhancing their relaxation rate to a larger extent than $[Ni(H_2O)_6]^{2+}$.

2. Dynamics of $[Ni(\textit{edta}H_x)]^{(2-x)-}$ within γ-Al_2O_3 Support Bodies Based on T_1 Contrast

While a shorter T_2 time leads to a lower NMR signal intensity in T_2-weighted images, a shorter T_1 time leads to higher signal intensity in T_1-weighted images (see expressions for M_{T2} and M_{T1}, respectively, in the footnote of Table 4.3). Table 4.3 shows the T_1 and T_2 relaxation times of water protons inside a catalyst body impregnated with 0.1 M $[Ni(H_2O)_6]^{2+}$ or with 0.1 M $[Ni(\textit{edta})]^{2-}$ (solution Ni*edta*1:1pH7). The relaxation times of pure water in a catalyst body are also presented as a reference. The relaxation times of protons decreased in the presence of Ni^{2+} ions in all cases. Yet, when Ni^{2+} was present as $[Ni(\textit{edta})]^{2-}$, the relaxation times were longer than when Ni^{2+} was totally coordinated to water molecules. The spin-lattice and spin-spin relaxation rates (T_i^{-1}, i = 1, 2) of water protons are affected by various interactions between the paramagnetic complex and the solvent molecules. Usually, the relaxation rate is described as the sum of the contributions due to inner-sphere interactions and outer-sphere interactions between the metal-ion and water molecules. It has been shown previously that the latter may have an important contribution to the total relaxation rate in the particular case of metal-ion complexes with a low water coordination number.[8, 21] *Edta* is a bulky ligand and the number of coordinated water molecules when Ni^{2+} is complexed to *edta* depends on the solution pH; at pH 7 the number of coordinated water molecules is essentially zero, and at pH 1 is 1, as determined by MCR analysis (see Appendix B). In these cases, *edta* impedes the

strong paramagnetic effect of Ni^{2+} on water protons and the main contribution to the relaxation rates is due to outer-sphere interactions with water. Conversely, in the case of $[Ni(H_2O)_6]^{2+}$, the relaxation of protons is caused by both inner-sphere and outer-sphere interactions with the water molecules, thus, the relaxation rates are faster.

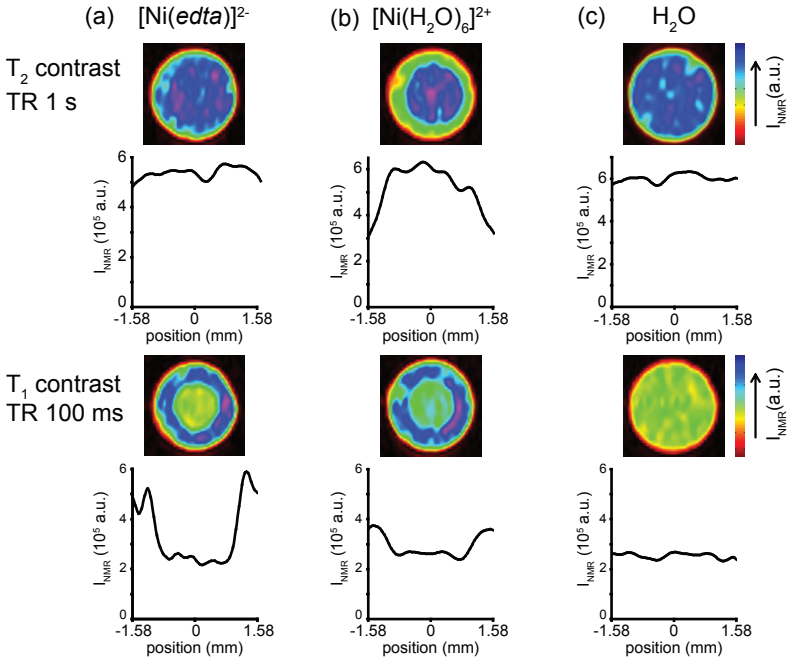

Figure 4.6. Images of catalyst bodies 5 min after impregnation with the solutions containing the complexes (a) $[Ni(edta)]^{2-}$ (0.1 M), (b) $[Ni(H_2O)_6]^{2+}$ (0.1 M), and (c) pure water. The images were recorded with TR = 1 s (top) and TR = 100 ms (bottom). The 1D signal intensity profiles as a function of the position inside the catalyst bodies are also shown.

Figure 4.6 shows the images and the corresponding 1D signal intensity profiles of extrudates impregnated with pure water and with 0.1 M $[Ni(H_2O)_6]^{2+}$ or 0.1 M Ni*edta*1:1pH7 solutions 5 min after impregnation. Two sets of images were collected with TR = 100 ms or 1 s.

When the repetition time was 1 s (Figure 4.6 top), the T_2-weighted image of an extrudate containing water showed a uniform NMR signal intensity around $6{\cdot}10^5$ a.u. The NMR image of an extrudate containing 0.1 M $[Ni(H_2O)_6]^{2+}$ showed T_2 contrast, with an outer green ring indicating the presence of Ni^{2+} (lower NMR signal

intensity) and the blue core representing the presence of pure water (NMR signal ~ $6{\cdot}10^5$ a.u.). With these working conditions (TR = 1 s), the NMR signal is low where Ni^{2+} is present since the relaxation rate T_2^{-1} of water protons in the presence of Ni^{2+} is very fast (relaxation time T_2 is short); i.e., when the NMR signal is collected, the protons in the presence of Ni^{2+} have relaxed giving a small NMR signal, see Table 4.3 (I/I_o^{1s}). The NMR image and the corresponding 1D signal intensity profile of an extrudate containing solution Ni*edta*1:1pH7 (complex $[Ni(edta)]^{2-}$) were almost identical to those of pure water; thus, under these experimental conditions the NMR signal of water protons was insensitive to the presence of $[Ni(edta)]^{2-}$ and the transport of Ni^{2+} could not be visualized. In other words, the NMR signals of water in the presence and in the absence of $[Ni(edta)]^{2-}$ were too close to be distinguished from each other. For the repetition time of 100 ms (T_1-weighted images at the bottom of Figure 4.6), the NMR image of a water-impregnated extrudate showed a uniform color and the corresponding 1D signal intensity profile indicated an average signal of $2{\cdot}10^5$ a.u. The NMR image of an extrudate containing $[Ni(H_2O)_6]^{2+}$ showed a mixed T_1-T_2 contrast, with a dominating contribution of T_1 contrast. The signal was the lowest in the core of the extrudate (green core), where pure water was present and its signal was suppressed (T_1 contrast). On the other hand, in the edges the NMR signal is low (blue ring) compared to that of pure water in the T_2-weighted image (see Figure 4.6 (c) top), but is higher than in the core. Thus, both T_1 and T_2 affect the signal intensity profile (mixed T_1 - T_2 contrast). The NMR image of the extrudate impregnated with solution Ni*edta*1:1pH7 exhibited pure T_1 contrast. The core of the extrudate, with an NMR signal of $2{\cdot}10^5$ a.u. and a green color, indicated the presence of pure water. The outer ring in blue color was assigned to the presence of $[Ni(edta)]^{2-}$, as expected. At these working conditions (TR = 100 ms), water protons which are not in contact with Ni^{2+} complexes have long T_1 relaxation rates (longer than TR). This means that these protons do not have enough time to relax and their NMR signal is suppressed. In the edges, the NMR signal intensity is high due to the presence of Ni^{2+} complexes. The T_1 relaxation time of water protons decreases in the presence of Ni^{2+} complexes, and water protons have enough time to relax giving a high NMR signal. The images were measured 5 min after impregnation and Ni^{2+} had not yet reached the core of the extrudate, in any case.

Table 4.3 summarizes all these NMR signal intensity profiles in numbers. The NMR signal intensity of the 1D profiles measured is represented as I_{NMR} (or I/I_o) in eq. (2). If the known values of T_1, T_2, TR and TE are substituted in eq. (2), the

quantities I/I_o^{1s} and I/I_o^{100ms} are obtained. The large TR values in comparison to the T_1 values in the presence of $[Ni(H_2O)_6]^{2+}$ or Ni*edta*1:1pH7 solutions are responsible for the absence of any influence of the spin-lattice relaxation on the total NMR signal ($M_{T1}^{100ms} \sim M_{T1}^{1s} \sim 1$ for these cases). On the other hand, a decrease in TR when the extrudates contained pure water induced a decrease in the NMR signal intensity ($M_{T1}^{100ms} = 0.37$).

In short, in order to visualize the transport of a shielded paramagnetic metal-ion complex (e.g., $[Ni(edta)]^{2-}$), T_1 contrast should be created by choosing an adequate repetition time in the two-pulse spin-echo sequence. However, T_1 contrast can also be used to monitor the transport of a non-shielded metal-ion complex ($[Ni(H_2O)_6]^{2+}$). Measuring T_1 contrast provides an increase in time resolution, which is advantageous if the transport of the metal-ion under study is very fast. In this study, the use of TR = 100 ms decreases the acquisition time of one NMR image by a factor of ten.

Figure 4.7 shows the T_1-weighted images collected on an extrudate at several points in time after its impregnation with solution Niedta1:1pH7 (complex $[Ni(edta)]^{2-}$). The blue external ring represents high NMR signal intensity values, and as explained above, it corresponds to the region where $[Ni(edta)]^{2-}$ is present. The green core indicates the presence of pure water (low NMR signal intensity).

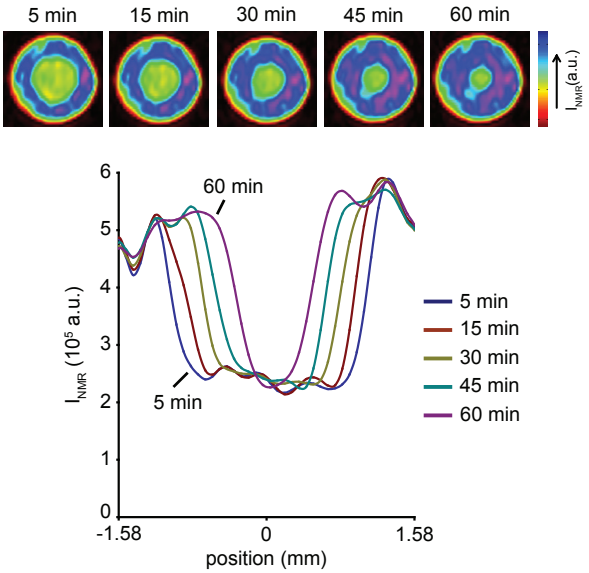

Figure 4.7. T_1-weighted images after impregnation of an extrudate with solution Ni*edta*1:1pH7, and the corresponding 1D signal intensity profiles as a function of the position inside the catalyst body.

One hour after impregnation [Ni(*edta*)]$^{2-}$ still showed an egg-shell distribution inside the extrudate (blue external ring). It took 90 to 120 min (images not shown) to get a uniform distribution of this complex. This time was expected according to a liquid phase diffusion transport of [Ni(*edta*)]$^{2-}$ when limited interactions between the complex and the support surface take place. Namely, it is assumed that [Ni(*edta*)]$^{2-}$ has a smaller diffusion coefficient than $[Ni(H_2O)_6]^{2+}$ since it is a bulkier complex. Moreover, electrostatic interactions between the complex and alumina surface are not very strong when the solution pH is close to the pzc of the support. The 1D signal intensity profiles as a function of the position inside the extrudate are also presented. In the edges, the NMR signal intensity remains constant with time after impregnation, since at these working conditions (TR = 100 ms) relaxation of water protons in the presence of [Ni(*edta*)]$^{2-}$ is fast enough. On the other hand, in the core, where no [Ni(*edta*)]$^{2-}$ is present after 5 min, water protons do not have time to relax and their signal is suppressed. As [Ni(*edta*)]$^{2-}$ diffuses to the core, water protons in that region relax faster, and ultimately have enough time to relax recovering the maximum signal. Since these 1D profiles show NMR signal intensities and not concentrations, no conservation of the area under the curves of Figure 4.7 is expected.

The transport of Ni^{2+} was also monitored after impregnating a catalyst body with solution Ni*edta*1:1pH1. It has to be mentioned that alumina is not stable at very low pH values and it can dissolve forming $[Al(H_2O)_6]^{3+}$. An MRI experiment on a similar extrudate after its impregnation with an aqueous solution of 0.1 M HCl showed the same T_2-weighted image or 1D NMR signal intensity profile as if it was impregnated with water. Moreover, the stability of [Ni(*edta*H_x)]$^{(2-x)-}$ (x = 1, 2) in the catalyst body was proven with UV-Vis-NIR micro-spectroscopy, as illustrated in Figure 4.8.

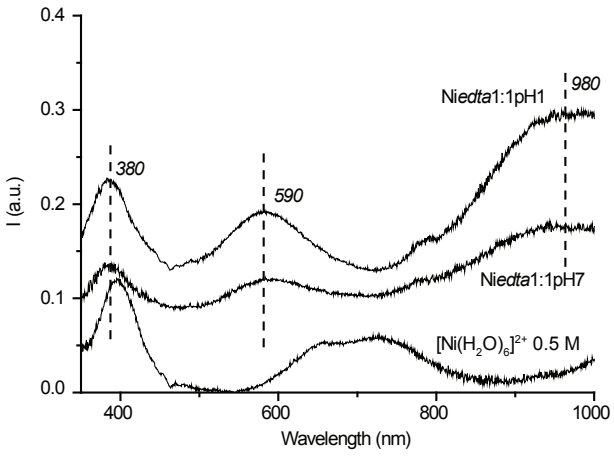

Figure 4.8. UV-Vis-NIR spectra measured on extrudates 5 min after impregnation with solutions Ni*edta*1:1pH1, Ni*edta*1:1pH7 and 0.5 M $[Ni(H_2O)_6]^{2+}$, close to the edges.

Figure 4.8 shows the UV-Vis-NIR spectra measured on two extrudates 5 min after impregnation with solutions Ni*edta*1:1pH1 and Niedta1:1pH7 close to the edges of the bodies. These spectra show the three typical absorption bands of Ni^{2+} in an octahedral environment surrounded by the *edta* ligand at 380, 590 and 980 nm, in solution. It is known that the protonation degree of the *edta* ligand, which is responsible for the formation of the complexes $[Ni(edtaH_x)]^{(2-x)-}$ (x = 0 - 2), does not affect substantially the position or absorption coefficient of the Ni^{2+} absorption bands. Still, the lower intensity measured on the impregnated extrudate with solution Ni*edta*1:1pH7 matches with a lower absorption coefficient of the $[Ni(edta)]^{2-}$ complex compared to the protonated ones.[22]

These UV-Vis-NIR spectra, which did not change with time after impregnation, evidence the stability of the $[Ni(edtaH_x)]^{(2-x)-}$ inside the pores of alumina and proves that dissolved Al^{3+} ions did not interact with Ni^{2+} to form other type of structures. This suggests that even though the possible dissolution of alumina cannot be excluded, it does not influence the NMR signal of the water protons. The Ni*edta*1:1pH1 solution contained the complexes $[Ni(edtaH)]^-$ and $[Ni(edtaH_2)]$, as summarized in Table 4.1. During the MRI experiments, it was not possible to distinguish the effect of $[Ni(edtaH)]^-$ or $[Ni(edtaH_2)]$ on the ^1H NMR signal of water, and they were treated as a whole. At pH 1, Ni^{2+} was penta- or tetra-coordinated to *edta*, and to one or two water molecules. Yet, Ni^{2+} did not show a strong paramagnetic effect on the relaxation of proton nuclei and its transport could not be visualized using T_2 contrast under our experimental conditions. T_1-weighted images collected during the dynamics of Ni^{2+}

after impregnation of a catalyst body with the Ni*edta*1:1pH1 solution indicated a slower transport of $[Ni(edtaH_x)]^{(2-x)-}$ (x = 1, 2) compared to that of $[Ni(edta)]^{2-}$ (solution at pH 7) meaning that at pH 1, the adsorption of Ni^{2+} complexes on alumina surface was stronger. This was also observed, at pH 3, by Bowers *et al.*[23] At pH 1, alumina net surface charge was positive facilitating the electrostatic interactions with negatively charged $[Ni(edtaH)]^-$ species. Moreover, the transport of $[Ni(edtaH_2)]$ towards the core induced the deprotonation of this species, due to an increase of the solution pH inside the pores, and the protonation of alumina surface. This acid-base reactions between $[Ni(edtaH_2)]$ and alumina surface provoked the formation of $[Ni(edtaH)]^-$ and $[Ni(edta)]^{2-}$ which, at the same time, also adsorbed electrostatically on the surface of alumina.

3. Dynamics of $[Ni(H_2O)_6]^{2+}$ and $[Ni(edtaH_x)]^{(2-x)-}$ within γ-Al_2O_3 Support Bodies Based on T_2 Contrast

As can be inferred from the previous section, when T_2 contrast (TR = 1 s) is applied to an extrudate impregnated with a solution containing both $[Ni(edtaH_x)]^{(2-x)-}$ and $[Ni(H_2O)_6]^{2+}$ (solutions Ni*edta*6:1pH1 or Ni*edta*6:1pH6), only the $[Ni(H_2O)_6]^{2+}$ complex should be visualized, see Figure 4.6 (a) and (b) top. This is true if there are no interactions between the two complexes or, in other words, if they behave independently inside the catalyst body. Assuming that this is the case, and only the complex $[Ni(H_2O)_6]^{2+}$ is visualized, the diffusion of this complex can be deduced from the NMR images and the 1D NMR signal intensity profiles shown in Figure 4.9. Figure 4.9 (a) shows the T_2-weighted images of two catalyst bodies after impregnation with solutions Ni*edta*6:1pH1 and Ni*edta*6:1pH6. The images measured 5 min after impregnation indicated a dark red outer rim with a low NMR signal (strong paramagnetic influence and high $[Ni(H_2O)_6]^{2+}$ concentration) and a blue core with a high NMR signal (weak paramagnetic influence and low $[Ni(H_2O)_6]^{2+}$ concentration) in both cases. After 2 h, the images showed an internal ring with a dark red color for the Ni*edta*6:1pH1 impregnated extrudate or an outer ring with a dark red color for the Ni*edta*6:1pH6 impregnated extrudate.

These images suggested an egg-white and an egg-shell Ni^{2+} macro-distribution, respectively. According to the reasoning presented at the beginning of this section, these egg-white and egg-shell distributions should reflect the distribution of $[Ni(H_2O)_6]^{2+}$, while no influence of the complex $[Ni(edtaH_x)]^{(2-x)-}$ on the ^1H NMR signal

is expected.

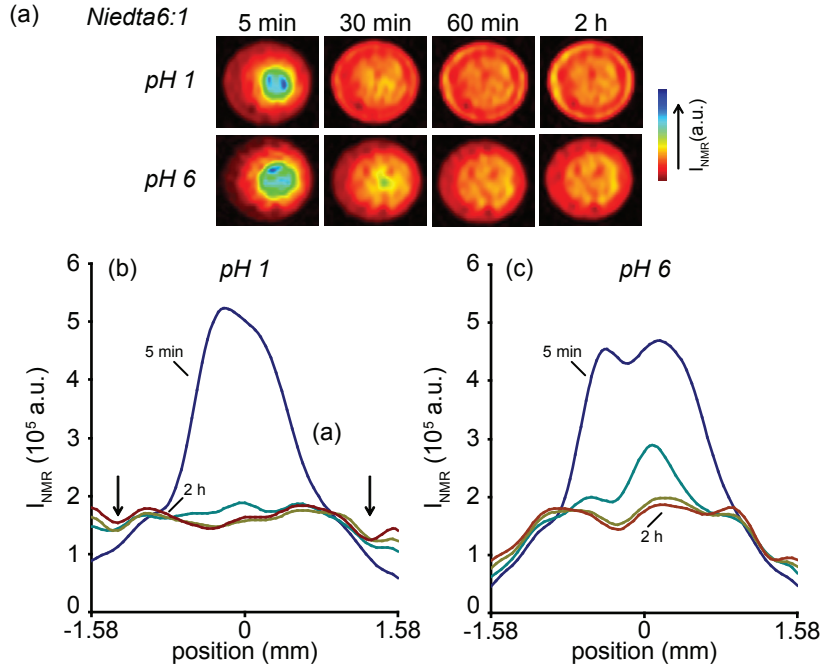

Figure 4.9. (a) T_2-weighted images at several times after impregnation of extrudates with solutions Ni*edta*6:1pH1 and Ni*edta*6:1pH6, and the corresponding 1D signal intensity profiles: (b) Ni*edta*6:1pH1, (c) Ni*edta*6:1pH6, as a function of the position inside the catalyst bodies.

Similarly, the 1D signal intensity profiles (Figure 4.9 (b) and (c)) pointed out a decrease in $[Ni(H_2O)_6]^{2+}$ concentration at the outer rim of the extrudate with time after impregnation, indicated by an increase of the NMR signal; and an increase in $[Ni(H_2O)_6]^{2+}$ concentration in the center, indicated by a decrease of the NMR signal. Thus, diffusion of $[Ni(H_2O)_6]^{2+}$ towards the core of the catalyst bodies took place. After 5 min, the center of the extrudates contained almost no $[Ni(H_2O)_6]^{2+}$, as deduced from the NMR signal intensity value, which was close to that of pure water ($6{\cdot}10^5$ a.u.). These signal intensity profiles indicated that $[Ni(H_2O)_6]^{2+}$ moved faster at pH 1 than at pH 6, due to the electrostatic repulsion between the positively charged alumina surface and $[Ni(H_2O)_6]^{2+}$. The inner ring that was formed when the catalyst body was impregnated with solution Ni*edta*6:1pH1 is not so easily visible in the 1D signal intensity profiles, and is indicated with arrows in the figure. This is because for $[Ni(H_2O)_6]^{2+}$ concentrations above 0.5 M, large variations in the concentration

give small variations of the NMR signal, as can be seen from the calibration curve depicted in Figure 4.3 (a).

An attempt to analyze the results was made under the assumption that the calibration curve (eq. (1)) constructed for the quantification of $[Ni(H_2O)_6]^{2+}$ transport is applicable in the presence of $[Ni(edtaH_x)]^{(2-x)-}$; i.e., when solutions Ni*edta*6:1pH1 and Ni*edta*6:1pH6 are used for impregnation. The resulting $[Ni(H_2O)_6]^{2+}$ concentration profiles obtained after 2 h and the corresponding T_2-weighted images of the impregnated extrudates are depicted in Figure 4.10.

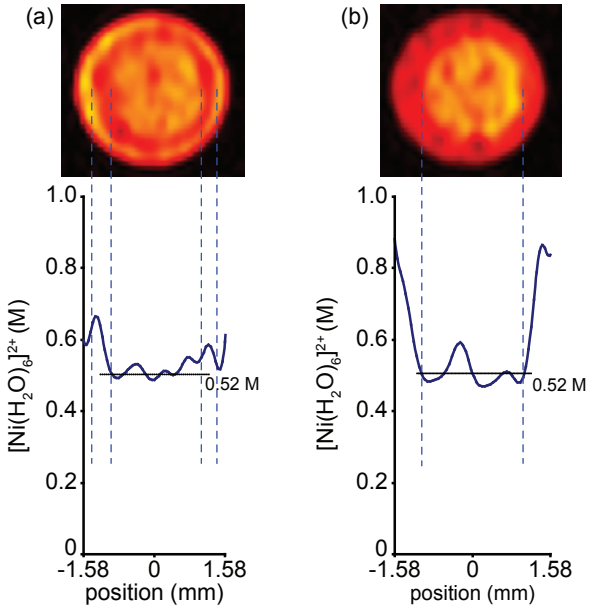

Figure 4.10. T_2-weighted images of extrudates 2 h after impregnation with solutions (a) Ni*edta*6:1pH1, and (b) Ni*edta*6:1pH6; and the corresponding $[Ni(H_2O)_6]^{2+}$ concentration profiles as a function of the position inside the extrudate constructed under the assumption that eq. (1) is valid when $[Ni(edtaH_x)]^{(2-x)-}$ complexes are present along with $[Ni(H_2O)_6]^{2+}$.

The apparent egg-white and egg-shell macro-distributions are clearly visualized in the 1D concentration profiles of Figure 4.10. The average $[Ni(H_2O)_6]^{2+}$ concentration in the core of the extrudates, regardless of the solution pH, was 0.52 M, which is in agreement with the concentration of $[Ni(H_2O)_6]^{2+}$ in the impregnation solution. However, the calculated concentrations of $[Ni(H_2O)_6]^{2+}$ in the positions where the NMR signal was the lowest were significantly higher (0.6 – 0.8 M, Figure 4.10). As a result, the average $[Ni(H_2O)_6]^{2+}$ concentrations over the entire cross section of the catalyst bodies impregnated with Ni*edta*6:1pH1 and Ni*edta*6:1pH6 solutions were calculated to be 0.56 M and 0.60 M, respectively. Both values are higher than the 0.5 M $[Ni(H_2O)_6]^{2+}$ concentration of the impregnation solutions and outside

the expected uncertainty. Therefore, the assumption about the applicability of the calibration curve (eq. (1)) for the quantification of the $[Ni(H_2O)_6]^{2+}$ concentration in the presence of other Ni^{2+} complexes may not be valid. This clearly indicates that $[Ni(edtaH_x)]^{(2-x)-}$ ions have an influence on the paramagnetic properties of $[Ni(H_2O)_6]^{2+}$, and consequently on the relaxation times of water protons when both complexes are present.

4. Dynamics of $[Ni(H_2O)_6]^{2+}$ and $[Ni(edtaH_x)]^{(2-x)-}$ within γ-Al_2O_3 Support Bodies Based on UV-Vis-NIR Micro-spectroscopy

Figure 4.11 shows the space resolved UV-Vis-NIR spectra of the catalyst bodies after impregnation with solutions Ni*edta*6:1pH1 and Ni*edta*6:1pH6. Figures 4.11 (a) and (b) show clear changes in the UV-Vis-NIR spectra measured from the edge (spectrum 6) to the core (spectrum 1) of the extrudates, after 5 min, regardless of the solution pH. Spectrum 1, in the core of the extrudate, suggests the only presence of NO_3^- ions ($n \longrightarrow \pi^*$ charge transfer transition at around 300 nm).[24] This observation corroborates the MRI data, which suggested the presence of pure water (Figure 4.9). The characteristic d-d absorption bands of $[Ni(H_2O)_6]^{2+}$ at 391, 654 and 730 nm were detected in spectra 2 - 4; however, they are slightly shifted to longer wavelengths (400, 659 and 738 nm).[24] The $[Ni(H_2O)_6]^{2+}$ d-d absorption band at 1100 nm was beyond the detection limit of the equipment, but its tail could also be visualized in spectra 2 - 4. The shift in the position of these bands suggested the exchange of water ligands by OH^- ligands or $Al\text{-}O^-$ from the alumina surface. The former ligands could come from the partial hydrolysis of this complex to form $[Ni(H_2O)_{6-x}(OH)_x]^{(2-x)+}$, due to adsorption of the protons on alumina surface, as discussed in Chapter 3. The latter ligands would form $[Ni(H_2O)_{6-x}(O\text{-}Al)_x]^{(2-x)+}$ due to replacement of one or more of the water ligands with the surface oxygen atoms from γ-alumina.[25]

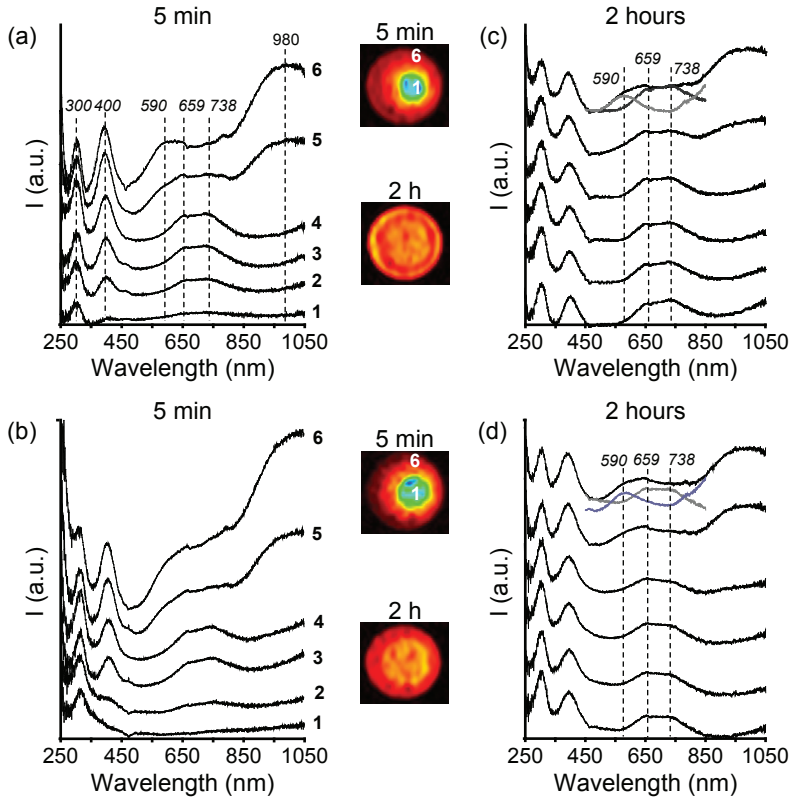

Figure 4.11. Space resolved UV-Vis-NIR spectra from the edge (6) to the center (1) of bisected catalyst bodies containing solutions (a, c) Ni*edta*6:1pH1 and (b, d) Ni*edta*6:1pH6, (a, b) 5 min and (c, d) 2 h after impregnation, together with the corresponding T_2-weighted images.

The transport rates of Ni^{2+}, deduced from the Ni^{2+} absorption bands, in both impregnated bodies were in agreement with those observed with MRI. In particular, the d-d transition bands of $[Ni(H_2O)_6]^{2+}$ indicated that 5 min after impregnation this complex was closer to the center in the extrudate impregnated with solution Ni*edta*6:1pH1. The spectra close to the edges (spectra 5 and 6), 5 min after impregnation, showed several bands. The 300-nm band indicative of NO_3^- was present, together with other three bands at around 400, 450-850 and 980 nm. These bands are assigned to the three d-d spin allowed transitions of six coordinate octahedral or pseudo-octahedral Ni^{2+}, and their positions depend on the type of

ligands.[24] The d-d transition bands for the complex $[Ni(edtaH_x)]^{(2-x)-}$ (x = 0 - 2) were observed at around 380, 590 and 980 nm.[22] The band at 400 nm is an indication of the presence of both $[Ni(H_2O)_6]^{2+}$ and/or $[Ni(edtaH_x)]^{(2-x)-}$ and the shape of the band at 450-850 nm also suggested the simultaneous presence of the complexes $[Ni(H_2O)_6]^{2+}$ (maximum absorption at around 659 and 738 nm) and $[Ni(edtaH_x)]^{(2-x)-}$ (maximum absorption at around 590 nm) regardless of the solution pH.[22, 24] Moreover, the band at 980 nm corroborated the presence of $[Ni(edtaH_x)]^{(2-x)-}$ in the outer rim of the catalyst bodies.[22] The UV-Vis-NIR spectra after impregnation of the same type of extrudates with the individual complexes $[Ni(H_2O)_6]^{2+}$and $[Ni(edtaH_x)]^{(2-x)-}$ are shown in Figure 4.8 as reference.

Figures 4.11 (c) and (d) show the space resolved UV-Vis-NIR spectra 2 h after impregnation. After this time, $[Ni(H_2O)_6]^{2+}$ was the only species in the core of the extrudate, regardless of the solution pH; as indicated by the Ni d-d transition bands at 400, 659 and 738 nm. Thus, $[Ni(H_2O)_6]^{2+}$ diffused faster than $[Ni(edtaH_x)]^{(2-x)-}$. However, it was also present in the edges of the catalyst bodies, as deduced from the shape of the band at 450-850 in the edge. Moreover, according to the MRI data shown in Figure 4.10 the concentration of $[Ni(H_2O)_6]^{2+}$ in the core is 0.52 M and equal to the concentration of this complex in the impregnation solution, taking into account the uncertainty of the MRI experiments. Thus, the concentration of $[Ni(H_2O)_6]^{2+}$ in the edges of the extrudates has to be also 0.5 M and this complex is uniformly distributed within the catalyst bodies. For this reason a deconvolution of the band at 450-850 nm in the edges of the catalyst body was done by simply subtracting the spectrum in the core (spectrum 1), which is that of pure $[Ni(H_2O)_6]^{2+}$, to the spectra in the edges (spectra 4 - 6). By doing this subtraction, the UV-Vis band of the $[Ni(edtaH_x)]^{(2-x)-}$ at 590 nm is derived. On the other hand, the deconvolution of the UV-Vis-NIR spectra measured after 5 min cannot be done reliably, since $[Ni(H_2O)_6]^{2+}$ was not uniformly distributed, and therefore, its concentration gradient is unknown. The bands at 590 and 960 nm indicated that, regardless of the pH and time after impregnation, $[Ni(edtaH_x)]^{(2-x)-}$ species remain in the outer rim of the extrudates. Still, it is difficult to assign these bands to a particular $[Ni(edtaH_x)]^{(2-x)-}$ complex due to the strong similarity in the UV-Vis-NIR spectra of the different $[Ni(edtaH_x)]^{(2-x)-}$ species (x = 0 - 2), as illustrated in Figure 4.8 .[22]

From the deconvolution, the areas under the bands at 590 nm ($[Ni(edtaH_x)]^{(2-x)-}$) and at 659 + 738 nm ($[Ni(H_2O)_6]^{2+}$) were calculated and their variation with position within the extrudates is shown in Figure 4.12.

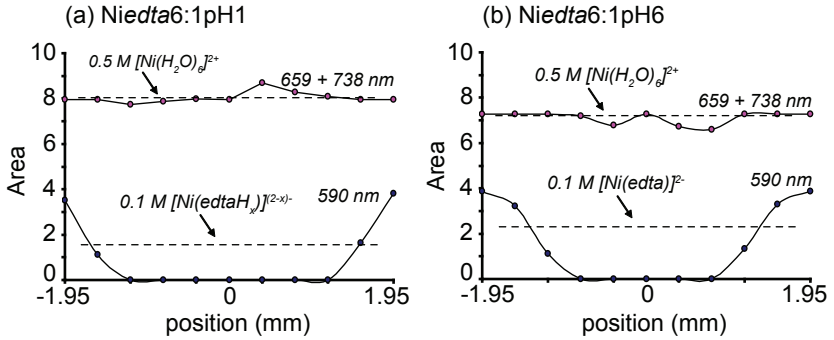

Figure 4.12. Area under the absorption bands at 590 nm and at 659 + 738 nm as a function of position in the catalyst bodies derived from the space resolved UV-Vis spectra obtained 2 h after impregnation of the extrudates with the solutions (a) Ni*edta*6:1pH1 and (b) Ni*edta*6:1pH6.

From these band areas, the concentration profiles of both complexes and of the total Ni^{2+} concentration as a function of position in the catalyst body, 2 h after impregnation, was estimated, as illustrated on Figure 4.13 (2).

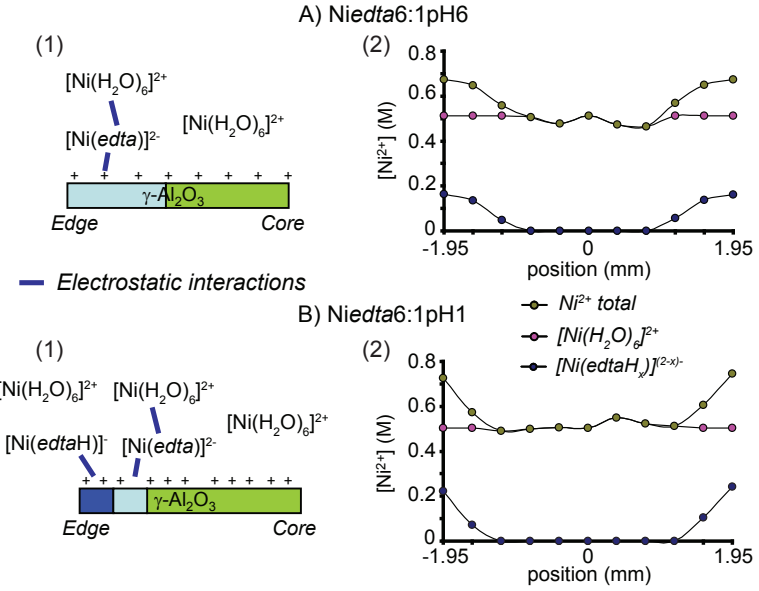

Figure 4.13. (1) Adsorption mechanism of $[Ni(H_2O)_6]^{2+}$ and $[Ni(edtaH_x)]^{(2-x)-}$ on γ-Al_2O_3 surface 2 h after impregnation of extrudates with the solutions (A) Ni*edta*6:1pH6 and (B) Ni*edta*6:1pH1; (2) Concentration distributions of these Ni^{2+} complexes and of the total Ni^{2+} concentration estimated from the deconvolution of the UV-Vis-NIR spectra shown in Figures 4.11 and 4.12.

5. Combined MRI and UV-Vis-NIR Micro-spectroscopic Study: Diffusion of Ni^{2+} Complexes and Their Interactions with the γ-Al_2O_3 Surface

A detailed analysis of the MRI and UV-Vis-NIR micro-spectroscopic results lead to propose a model for diffusion and adsorption/desorption on γ-Al_2O_3 surface of $[Ni(H_2O)_6]^{2+}$ and $[Ni(edtaH_x)]^{(2-x)-}$ as a function of pH, when these complexes are co-impregnated.

5.1. Impregnation of Solution Niedta6:1pH6

5 min after impregnating the extrudate with the solution Ni*edta*6:1pH6, alumina becomes slightly positively charged since its pzc is 7.9.[26] For this reason, $[Ni(edta)]^{2-}$ interacts electrostatically with the γ-Al_2O_3 surface, while $[Ni(H_2O)_6]^{2+}$ does not. Therefore, the diffusion of $[Ni(edta)]^{2-}$ towards the core is slower than the transport of $[Ni(H_2O)_6]^{2+}$.

Besides, the protonation of the alumina surface brings about an increase of the solution pH inside the pores. This increase is determined by the pzc of alumina and, therefore, cannot be higher than 7.9. The pH increase in the pores will not affect the molecular structure of the $[Ni(edta)]^{2-}$ complex since it is stable in the pH region of interest. However, $[Ni(H_2O)_6]^{2+}$, in the edges of the extrudate, can partially hydrolyze or even precipitate (in solution or at the surface). The formation of e.g. $[Ni(H_2O)_4(OH)_2]$ will cause a decrease of the solution pH which in turn stops the precipitation or hydrolysis and the remaining $[Ni(H_2O)_6]^{2+}$ can move forward.

After 2 h, UV-Vis-NIR micro-spectroscopy indicated that $[Ni(H_2O)_6]^{2+}$ was present in the core and in the outer rim of the catalyst body, while $[Ni(edta)]^{2-}$ was only present in the outer rim. The $[Ni(H_2O)_6]^{2+}$ concentration in the core region, where this complex was unique, was evaluated from the MRI data as 0.52 M. Thus, its concentration in the edges should be approximately the same. The higher concentration values obtained in this region (0.6 - 0.8 M) using eq. (1) imply that this calibration is not valid when both $[Ni(edta)]^{2-}$ and $[Ni(H_2O)_6]^{2+}$ are present in solution. In other words, the local presence of both Ni^{2+} complexes in the edges of the extrudate leads to a stronger paramagnetic influence on the relaxation rate of water protons. This cannot be explained as a simple additive effect of the two

paramagnetic complexes, since, as demonstrated above, the effect of $[Ni(edta)]^{2-}$ is too small to be observed in the T_2-weighted images (Figure 4.6). Therefore, we have to conclude that the degree of paramagnetic influence of $[Ni(H_2O)_6]^{2+}$ on water protons changes in the presence of $[Ni(edta)]^{2-}$.

An adsorption mechanism, presented in Figure 4.13 (A1), is suggested as follows. When $[Ni(edta)]^{2-}$ is adsorbed on the positively charged alumina surface, the $[Ni(edta)]^{2-}$ negative charge is not totally compensated by the support surface charge. [23, 26, 27] Therefore, the adsorption of $[Ni(edta)]^{2-}$ on alumina creates a negative layer or charge reversal of alumina surface, which enhances the electrostatic interactions between the surface layer and $[Ni(H_2O)_6]^{2+}$ and, thus, changes the paramagnetic influence of $[Ni(H_2O)_6]^{2+}$ on the relaxation of water protons. Hence, the actual overall Ni concentration profile 2 h after impregnation was egg-shell like, with a uniform 0.5-M-$[Ni(H_2O)_6]^{2+}$ distribution and an egg-shell $[Ni(edta)]^{2-}$ profile, as illustrated in Figure 4.13 (A2). Moreover, electrostatic interactions are taking place between the $[Ni(H_2O)_6]^{2+}$ and the negative surface layer created by adsorption of $[Ni(edta)]^{2-}$ on alumina surface in the edges of the extrudate.

5.2. Impregnation of Solution Niedta6:1pH1

5 min after impregnating the extrudate with the solution Ni*edta*6:1pH1, a similar diffusion mechanism of $[Ni(edtaH_x)]^{(2-x)-}$ (x = 1 and 2) and $[Ni(H_2O)_6]^{2+}$ as at pH 6 takes place. At this pH value, γ-Al_2O_3 becomes even more positively charged. From the space resolved UV-Vis-NIR spectra and the MRI data after this time, it is possible to conclude that, again, $[Ni(edtaH)]^{-}$ adsorbs electrostatically at the edges of the extrudate. On the other hand, $[Ni(edtaH_2)]$ and $[Ni(H_2O)_6]^{2+}$ do not adsorb and move towards the core. $[Ni(H_2O)_6]^{2+}$, however, diffuses faster than $[Ni(edtaH_2)]$. The diffusion rate of $[Ni(H_2O)_6]^{2+}$ is faster at this pH than at pH 6. This occurs because the solution pH inside the pores of alumina, even though it increases, is more acidic than after impregnation of alumina with the solution at pH 6. Therefore, the hydrolysis of $[Ni(H_2O)_6]^{2+}$ occurs to a limited extent.

UV-Vis-NIR micro-spectroscopic data 2 h after impregnation indicated the only presence of $[Ni(H_2O)_6]^{2+}$ in the core of the extrudate, and the presence of both $[Ni(H_2O)_6]^{2+}$ and $[Ni(edtaH_x)]^{(2-x)-}$ towards the edges (Figure 4.11 (c)). From the concentration profile shown in Figure 4.10 (a), $[Ni(H_2O)_6]^{2+}$ concentration was calculated to be 0.52 M in the core of the catalyst body. Therefore, 0.52 M has to be also the concentration of $[Ni(H_2O)_6]^{2+}$ in the edges of the catalyst body. The T_2-

weighted images demonstrated the presence of an inner ring with the lowest NMR signal of the cross section of the catalyst body. The formation of this egg-white distribution at pH 1, compared to the egg-shell at pH 6, is linked to the presence of the two $[Ni(edtaH_x)]^{(2-x)-}$ (x = 1, 2) species instead of $[Ni(edta)]^{2-}$, present at pH 6. The different paramagnetic influence in the edges and in the inner ring (indicated by arrows in Figure 4.9 (b)) is most likely connected to the different interactions of $[Ni(edtaH)]^-$ and $[Ni(edtaH_2)]$ complexes with the alumina surface.

When an extrudate was impregnated with solution Ni*edta*6:1pH1, immediately after impregnation $[Ni(edtaH)]^-$ was adsorbed electrostatically at the edges of the extrudate on the positively charged alumina surface and its charge could be totally compensated by the positive alumina hydroxyl groups.[23] In this position, no charge reversal of the alumina surface took place and $[Ni(H_2O)_6]^{2+}$ that was present did not interact electrostatically with this species. Consequently, the paramagnetic influence of $[Ni(H_2O)_6]^{2+}$ on water protons was not enhanced. At the same time, the complex $[Ni(edtaH_2)]$ moved deeper in the extrudate since its neutral charge prevents it from interacting electrostatically with the alumina surface. However, the solution pH increases during its transport towards the core. Therefore, this complex underwent acid-base reactions with hydroxyls on alumina surface. $[Ni(edtaH_2)]$ could deprotonate, while moving towards the core, and formed $[Ni(edtaH)]^-$ and $[Ni(edta)]^{2-}$, with the latter being stable at pH above 2.5. Within an inner ring, the electrostatic adsorption of $[Ni(edta)]^{2-}$ on the alumina surface could result in charge reversal of the surface and promote the electrostatic adsorption of $[Ni(H_2O)_6]^{2+}$ on $[Ni(edta)]^{2-}$, as explained previously, and enhanced the relaxation rate of water protons. The higher relaxation rate of water protons in the inner ring resulted in the apparent egg-white concentration profile. The electrostatic interactions between the Ni^{2+} complexes due to charge reversal are depicted schematically in Figure 4.13 (B1). However, the actual Ni concentration profile estimated from the UV-Vis-NIR and MRI data was egg-shell with a 0.5-M uniform distribution of $[Ni(H_2O)_6]^{2+}$ and an egg-shell like distribution of Ni-*edta* species, similar to that obtained after impregnation with the solution Ni*edta*6:1pH6, Figure 4.13 (B2).

To summarize, the quantitative $[Ni(H_2O)_6]^{2+}$ concentration profiles calculated from the NMR images in the presence of $[Ni(edtaH_x)]^{(2-x)-}$ were only valid in the core of the catalyst bodies; i.e., in the region where this complex was unique. The overall Ni macro-distribution was egg-shell, regardless of the solution pH. In the outer rim of the catalyst body, the paramagnetic influence of $[Ni(H_2O)_6]^{2+}$ on the relaxation

of water protons was enhanced due to the presence of $[Ni(edta)]^{2-}$. The different signal intensity profiles obtained depending on the solution pH suggested that the relaxation rate of water protons depends on the type and strength of the interactions of the Ni^{2+} complexes with each other and with the support surface. In other words, the electrostatic interactions between $[Ni(edta)]^{2-}$ and $[Ni(H_2O)_6]^{2+}$ increase the relaxation rate of water protons. On the contrary, the presence of $[Ni(edtaH)]^{-}$ does not significantly change the paramagnetic influence of $[Ni(H_2O)_6]^{2+}$ on the water protons since no electrostatic interactions are present once $[Ni(edtaH)]^{-}$ is adsorbed on the alumina surface.

Conclusions

MRI is a powerful tool to monitor in a quantitative manner the impregnation of paramagnetic metal-ion complexes, such as $[Ni(H_2O)_6]^{2+}$, on mm-sized catalyst bodies. The dynamics of shielded paramagnetic metal-ion complexes, e.g. $[Ni(edta)]^{2-}$ chelated complexes, can also be monitored by means of ^{1}H-MRI, but a different imaging contrast is required that makes quantification of the paramagnetic metal-ion impossible. Furthermore, the combination of MRI with UV-Vis-NIR micro-spectroscopy provides complementary chemical information regarding the interactions between two co-impregnated species within support bodies, such as $[Ni(H_2O)_6]^{2+}$ and $[Ni(edtaH_x)]^{(2-x)-}$. In this particular case, it has been revealed charge reversal of the γ-Al_2O_3 surface due to the electrostatic interactions between $[Ni(edta)]^{2-}$ and the positively charged alumina surface without compensation of the anionic charge of the Ni^{2+} complex. This phenomenon yields the consequent electrostatic adsorption of $[Ni(H_2O)_6]^{2+}$ on $[Ni(edta)]^{2-}$. These interactions, which already occur in the first stage of catalyst preparation, are directly responsible for the final metal-concentration distributions in the extrudate and for its final metal phase(s) and dispersion. More specifically, the use of *edta* in a low *edta*:Ni^{2+} molar ratio suggests the formation of Ni^{2+} egg-shell distributions, when an acidic solution is used, with the *edta* ligand acting as a linker between Ni^{2+} and alumina surface. These profiles, which are not easy to achieve in the preparation of Ni catalyst bodies, are interesting profiles in chemical reactions with diffusional restrictions.

Acknowledgments

Dr. Anna A. Lysova and Prof. dr. Igor V. Koptyug of the International Tomography Center SB RAS in Novosibirsk (Russia) are kindly acknowledged for facilitating the MRI measurements and their help in the interpretation of the results. Thanks also to Peter de Peinder and Ad Mens (Inorganic Chemistry and Catalysis group, Utrecht University) for carrying out the MCR analysis of the impregnation solutions and N_2 physisorption on the γ-Al_2O_3 support, respectively.

References

[1] J. A. Bergwerff, A. A. Lysova, L. Espinosa Alonso, I. V. Koptyug, B. M. Weckhuysen, *Angew. Chem. Int. Ed.* **2007**, *46*, 7224.
[2] J. A. Bergwerff, A. A. Lysova, L. Espinosa-Alonso, I. V. Koptyug, B. M. Weckhuysen, *Chem. Eur. J.* **2008**, *14*, 2363.
[3] I. V. Koptyug, V. B. Fenelonov, L. Y. Khitrina, R. Z. Sagdeev, V. N. Parmon, *J. Phys. Chem. B* **1998**, *102*, 3090.
[4] I. V. Koptyug, A. V. Khomichev, A. A. Lysova, R. Z. Sagdeev, *J. Am. Chem. Soc.* **2008**, *130*, 10452.
[5] I. V. Koptyug, A. V. Kulikov, A. A. Lysova, V. A. Kirillov, V. N. Parmon, R. Z. Sagdeev, *J. Am. Chem. Soc.* **2002**, *124*, 9684.
[6] T. R. Bryar, C. J. Daughney, R. J. Knight, *J. Magn. Reson.* **2000**, *142*, 74.
[7] W. Kuhn, *Angew. Chem. Int. Ed.* **1990**, *29*, 1.
[8] R. B. Lauffer, *Chem. Rev.* **1987**, *87*, 901.
[9] G. Tomer, M. D. Mantle, L. F. Gladden, J. M. Newton, *Int. J. Pharm.* **1999**, *189*, 19.
[10] A. A. Lysova, I. V. Koptyug, R. Z. Sagdeev, V. N. Parmon, J. A. Bergwerff, B. M. Weckhuysen, *J. Am. Chem. Soc.* **2005**, *127*, 11916.
[11] M. W. Grant, H. W. Dodgen, J. P. Hunt, *J. Am. Chem. Soc.* **1971**, *93*, 6828.
[12] G. S. Smith, J. L. Hoard, *J. Am. Chem. Soc.* **1959**, *81*, 556.
[13] L. G. van de Water, J. A. Bergwerff, T. A. Nijhuis, K. P. de Jong, B. M. Weckhuysen, *J. Am. Chem. Soc.* **2005**, *127*, 5024.
[14] J. Park, J. R. Regalbuto, *J. Colloid Interface Sci.* **1995**, *175*, 239.
[15] P. T. Callaghan, *Principles of Nuclear Magnetic Resonance Microscopy*, Claredon Press, Oxford, **1991**.
[16] S. Lalith Talagala, I. J. Lowe, *Concepts Magn. Reson.* **1991**, *3*, 145.
[17] I. V. Koptyug, A. A. Lysova, R. Z. Sagdeev, V. N. Parmon, *Catal. Today* **2007**, *126*, 37.
[18] E. M. Assaf, L. C. Jesus, J. M. Assaf, *Chem. Eng. J.* **2003**, *94*, 93.
[19] A. V. Neimark, L. I. Kheifets, V. B. Fenelonov, *Ind. Eng. Chem. Prod. Res. Dev.* **1981**, *20*, 439.

[20] R. Takahashi, S. Sato, T. Sodesawa, Y. Kamomae, *Phys. Chem. Chem. Phys.* **2000**, *2*, 1199.
[21] J. Oakes, E. G. Smith, *J. Chem. Soc. Faraday Trans.* **1983**, *79*, 543.
[22] T. R. Bhat, M. Krishnamurthy, *J. Inorg. Nucl. Chem.* **1963**, *25*, 1147.
[23] A. R. Bowers, C. P. Huang, *J. Colloid Interface Sci.* **1986**, *110*, 575.
[24] A. B. P. Lever, *Inorganic Electronic Spectroscopy*, Elsevier Science B. V., Amsterdam, **1987**.
[25] L. Espinosa-Alonso, K. P. de Jong, B. M. Weckhuysen, *J. Phys. Chem. C* **2008**, *112*, 7201; *Chapter 3 in this PhD thesis*.
[26] K. Bourikas, C. Kordulis, A. Lycourghiotis, *Catal. Rev. Sci. Eng.* **2006**, *48*, 363.
[27] B. Nowack, J. Lutzenkirchen, P. Behra, L. Sigg, *Environ. Sci. Technol.* **1996**, *30*, 2397.

Chapter 5

Tomographic Energy Dispersive Diffraction Imaging to Study the Genesis of Ni Nanoparticles within γ-Al_2O_3 Catalyst Bodies

Abstract

Tomographic Energy Dispersive Diffraction Imaging (TEDDI) is a recently developed synchrotron-based characterization technique used to obtain spatially resolved X-ray diffraction and fluorescence information in a noninvasive manner. With the use of a synchrotron beam, three-dimensional (3D) information can be conveniently obtained on the elemental composition and related crystalline phases of the interior of a material. In this Chapter, we show its application to characterize the structure of a heterogeneous catalyst body in situ during thermal treatment. Ni/γ-Al_2O_3 hydrogenation catalyst bodies have been chosen as the system of study. As a first example, the heat treatment in N_2 of a [Ni(*en*)$_3$](NO$_3$)$_2$/γ-Al_2O_3 catalyst body has been studied. In this case, the crystalline [Ni(*en*)$_3$](NO$_3$)$_2$ precursor was detected in an egg-shell distribution, and its decomposition to form metallic Ni crystallites of around 5 nm was imaged. In the second example, the heat treatment in N_2 of a [Ni(*en*)(H_2O)$_4$]Cl_2/γ-Al_2O_3 catalyst body was followed. The initial [Ni(*en*)(H_2O)$_4$]Cl_2 precursor was uniformly distributed within the catalyst body as an amorphous material, and decomposed to form metallic Ni crystallites of around 30 nm with a uniform distribution. TEDDI also revealed that the decomposition of [Ni(*en*)(H_2O)$_4$]Cl_2 takes place via two intermediate crystalline structures. The first one, which appears at around 180 ^{o}C, is related to the restructuring of the Ni precursor on the alumina surface; while the second one, assigned to the formation of a limited amount of Ni_3C, is observed at 290 ^{o}C.

Introduction

In Chapter 4 the application of MRI as a noninvasive and in situ characterization method in the preparation of catalyst bodies has been presented and some of the possibilities to get insight into the impregnation step of different Ni^{2+} metal-ion complexes; i.e., dynamics and adsorption phenomena on the support surface, were illustrated. In this Chapter, another noninvasive method is introduced, namely Tomographic Energy Dispersive Diffraction Imaging (TEDDI). More specifically, the application of TEDDI under realistic preparation conditions; i.e., during the heat treatment or calcination step, of a heterogeneous catalyst is presented with the aim to obtain new insight into the changes on the molecular structure of the Ni^{2+} metal-ion precursor complex along the catalyst body as a function of temperature. For this purpose, the calcination of 10 wt% Ni/γ-Al_2O_3 hydrogenation catalyst bodies has been chosen as the system to investigate and two examples with different precursor complexes containing ethylenediamine (*en*) are discussed; i.e., [Ni(*en*)$(H_2O)_4$]Cl_2 and [Ni(*en*)$_3$]$(NO_3)_2$. These precursors are known to yield, under specific experimental conditions such as calcination under an inert atmosphere, highly dispersed metallic Ni particles on powdered catalysts.[1-7] The experiments described in this Chapter present TEDDI as a chemical imaging tool to monitor the genesis of Ni nanoparticles in 3D within γ-Al_2O_3 catalyst bodies.

Materials and Methods

1. Materials

The support material used in this study was γ-Al_2O_3 in the form of pellets (Engelhard, 3 mm length and diameter). The pore volume was 0.7 ml/g, the surface area 209 m^2/g and the pore size 13 nm, as determined by N_2 physisorption. The point of zero charge (pzc) was determined to be 7.8 by mass titration.[8]

Two different catalytic materials were prepared from the precursor complexes [Ni(*en*)$_3$]$(NO_3)_2$ and [Ni(*en*)$(H_2O)_4$]Cl_2, (*en* = ethylenediamine). The final metallic Ni content was 10 wt %, and the samples differed with respect to the Ni precursor salt (nitrate or chloride) and in the molar *en*:Ni ratio.

The nitrate sample, [Ni(*en*)$_3$]$(NO_3)_2$/γ-Al_2O_3, was prepared via pore volume

impregnation of a solution containing 1.9 M $Ni(NO_3)_2 \cdot 6\ H_2O$ (Acros, p.a.) and 5.7 M ethylenediamine (*en*, Acros, p.a.) of the γ-Al_2O_3 pellets. As the impregnation solution was not stable at 25 °C and crystallized after a short time forming $[Ni(en)_3](NO_3)_2$ crystals, it was warmed up to 60 °C for 30 min prior to impregnation. Pore volume impregnation was then carried out as follows: a 0.9-g batch of γ-Al_2O_3 pellets and a syringe containing the required volume of the impregnation solution were kept at 60 °C for 4 h. After that time, the pellets were impregnated drop-wise in 2 min and shaken manually for 2 min to ensure a homogeneous distribution of the solution on the pellets. Subsequently, the pellets were left to equilibrate in a closed vessel for 2 h in an oven at 60 °C to avoid crystallization of $[Ni(en)_3](NO_3)_2$. The vessel contained a wet tissue on top to avoid drying of the pellets. After that time, the pellets were dried at 20 °C (room temperature) overnight.

The chloride sample, $[Ni(en)(H_2O)_4]Cl_2/\gamma$-$Al_2O_3$, was prepared via pore volume impregnation of a solution containing 1.9 M $NiCl_2 \cdot 6\ H_2O$ (Acros, p.a.) and 1.9 M ethylenediamine (*en*, Acros, p.a.) on the γ-Al_2O_3 pellets. The solution was stable at 20 °C, and pore volume impregnation was performed at 20 °C by adding the solution drop-wise on the pellets. The addition was followed by manual shaking for 2 min and the pellets were subsequently equilibrated for 2 h in a closed vessel with a wet tissue to avoid drying. The pellets were then dried at 20 °C overnight.

2. In situ Calcination Experiments

Calcination of a single catalyst body of the prepared samples was carried out by heating from 25 °C to 500 °C (4 °C/min) under a flowing N_2 environment. This controlled atmosphere was realized using an environmental cell specifically designed to provide an oxygen-free environment while performing the TEDDI experiments. The cell is schematically depicted in Figure 5.1, while photographs of the set-up can be found in Appendix C.

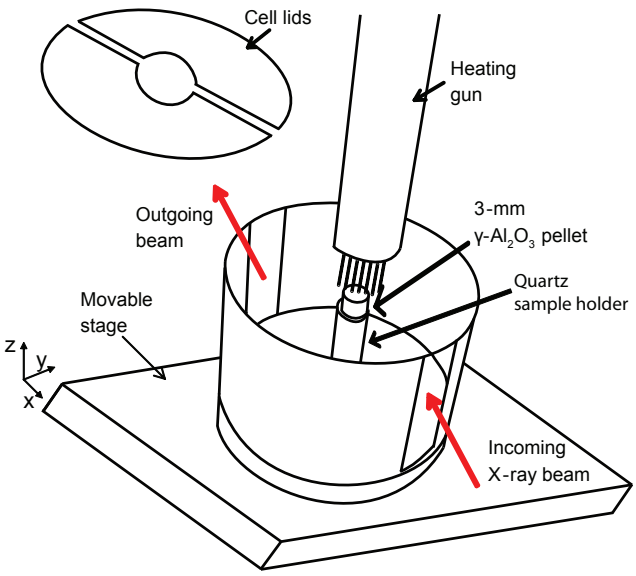

Figure 5.1. Schematic of the environmental cell designed for in situ calcination TEDDI experiments.

The environmental cell consists of a stainless steel cylinder (9.5 cm height and 10.5 cm diameter) located on a movable (*x, y, z*) stage, as depicted in Figure 5.1. The cylinder consists of a quartz sample holder upon which the catalyst body is mounted. A heating gun located 1 cm above the pellet provides the N_2 at a controlled temperature and flow. The cell contains two Kapton windows (0.25 mm thickness) through which the incident X-ray beam enters and the scattered/emitted signal leaves, respectively. Finally, the integrity of the environmental cell is maintained at the top with two removable stainless steel lids. Scanning of the catalyst body inside the environmental cell is then performed in a step-wise manner in the *x, y* and *z* directions, as indicated in Figure 5.1.

3. TEDDI Measurements

Measurements were performed at the Daresbury SRS synchrotron station 16.4, which utilises a slitted white wiggler beam and three energy discriminating MCA detectors to collect the data. The rectangular cross-sectioned beam gives a minimum diffracting lozenge (scanning volume) length of ca. 2.47 x 0.1 x 0.2 mm^3 (*x* x *y* x *z*). Figure 5.2 shows an schematic of the TEDDI set-up.

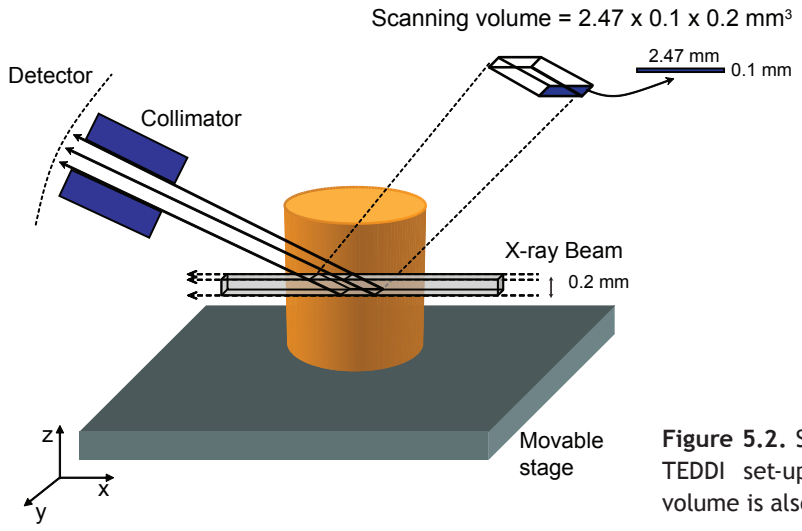

Figure 5.2. Schematic of the TEDDI set-up, the scanning volume is also indicated.

According to this set-up, the scanning volume comes from the cross section between the incoming X-ray beam and the scattered X-ray beam at a fixed angle (6.97°). This cross section is fixed during the TEDDI experiments, and by means of the movable (*x*, *y*, *z*) stage, the sample is moved towards or away from it. Therefore, the signal collected at each position of the pellet depends on the amount of the scanning volume that is within the pellet. In this way, when the center of the scanning volume is at the center of the pellet, then, 100 % of the former is contained within the pellet (position 1 in Figure 5.3 (a)).

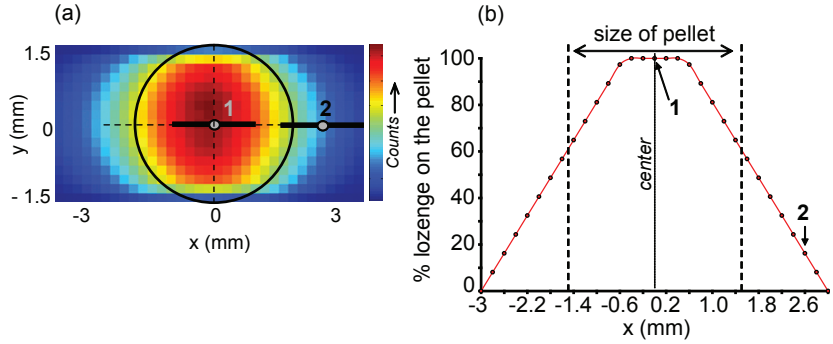

Figure 5.3. (a) Raw XY TEDDI intensity image obtained from the XY scanning experiment on the $[Ni(en)_3](NO_3)_2/\gamma$-$Al_2O_3$ pellet after calcination at 500°C. The black circumference represents the real size of the catalyst body and the black bars represent the scanning volume in the center of the pellet (1) and 2.6 mm from the center (2); (b) Amount of scanning volume or lozenge (% of its length in the *x* direction) inside the pellet as a function of the position in the pellet along the same direction. This variation was calculated when $y = 0$.

Thus, the number of counts reaching the detector is at a maximum, as can be deduced from the red color (greatest signal intensity) in the center of the XY TEDDI image in Figure 5.3 (a). On the other hand, because of the length of the scanning volume in the x direction, if the center of the pellet is moved, for example, 2.6 mm in the same direction, from the center of the scanning volume (position 2 in Figure 5.3 (a)), the signal reaching the detector contains less counts, since only 16 % of the scanning volume is still within the pellet. The amount of scanning volume that is within the pellet as a function of the position on the pellet in the x direction (at $y = 0$) is represented in Figure 5.3 (b).

Three different scanning experiments were conducted and a schematic of these with regard to the catalyst body is depicted in Figure 5.4.

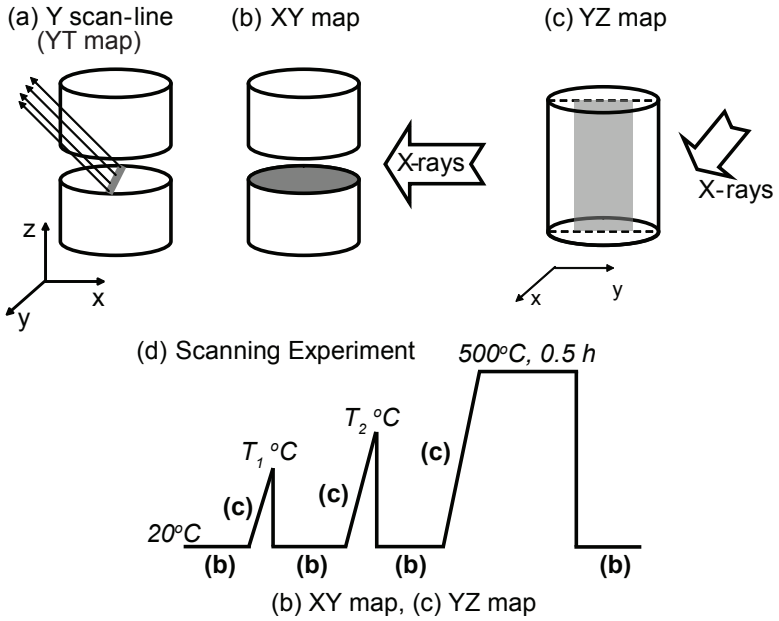

Figure 5.4. Scanning experiments performed (a-c) during calcination (d): (a) 1D Y scan-line with temperature (YT map), (b) 2D XY map and (c) 2D YZ map. The grey areas represent the scanning regions during the calcination process. In order to collect the XY maps the samples were quenched according to the temperature profiles depicted in (d).

Firstly, a Y scan-line in the center of the catalyst body (1D scan where x = z = 0 mm = center of the pellet) was measured continuously on a pellet during the calcination and will be referred to as YT map, as depicted in Figure 5.4 (a). The step size was 0.2 mm and the time needed to measure one scan-line was 5.5 min. Secondly, a high quality XY map (2D scan with z = 0 mm) was acquired on a new pellet at several temperatures during the calcination process (Figure 5.4 (b)). The step size was 0.2 mm in the x and y directions and the time required to obtain one XY map was 3.7 h. As illustrated in Figure 5.4 (d), due to the long scanning times of the XY maps, in order to relate these maps to specific temperature points in the calcination process, the samples were quenched to 25 °C after calcination for acquisition of the XY maps. Previous experiments have demonstrated that this quenching did not cause significant differences in the final Ni phase. Finally, YZ maps were collected (2D scans with x = 0 mm) in situ during the calcination; thus, between 25 °C and the selected temperature to measure an XY map, see Figures 5.4 (c) and (d). The step size

was 1.3 mm in the *x* direction and 0.2 mm in the *z* direction; 6.8 min were required to collect an YZ map.

Figure 5.5 shows the typical raw TEDDI images obtained from a YT and a XY map of a catalyst body.

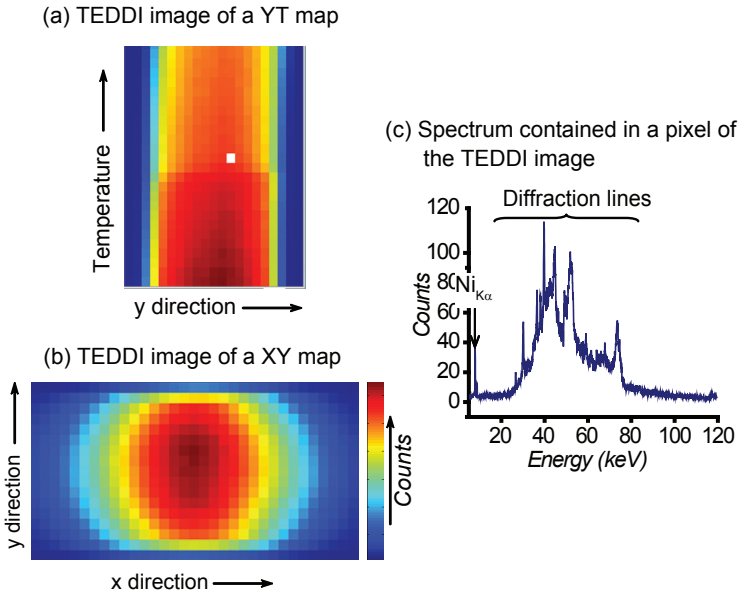

Figure 5.5. Raw TEDDI images of a (a) YT map, and a (b) XY map on the pellet after the selected temperature and quenching; and (c) typical total spectrum contained in a pixel of a TEDDI image. The blue pixels represent patterns with a low number of total counts and the red pixels represent regions with a high number of counts.

Each pixel in the TEDDI images pertains to an associated energy dispersive spectrum, as illustrated in Figure 5.5 (c), and a scanning volume of 2.47 x 0.1 x 0.2 mm^3 (*x* x *y* x *z*). Such a spectrum contains two types of information: namely, the fluorescence signal from the Ni ($Ni_{K\alpha}$ at 7.5 keV) and Bragg reflections from the crystalline catalytic material; i.e., the γ-Al_2O_3 support body and other Ni crystalline phases. Concentration maps can be constructed of selected phases, related to the appropriate diffraction or fluorescence peaks, based on the area (or intensity) of the fitted peak(s) above the background level. Batch multiple data processing of the TEDDI images were performed using the EasyEDD software developed by Sochi *et al.*[9]

It should be noted that the XY maps of the pellet appear slightly elongated (i.e.

not truly circular) in the *x* direction due to the asymmetric shape of the scanning volume with a significantly longer *x*-dimension (2.47 mm). In order to construct 2D maps of the Ni fluorescence or diffraction signals (YT, XY and YZ maps), the spectra obtained had to be corrected for the fraction of lozenge (scanning volume) that is within the pellet. To do this correction, two different approaches were used depending on the peak of interest (diffraction or fluorescence) which are explained in detail in Appendix C.

Results and Discussion

1. TEDDI During the Calcination of the $[Ni(en)_3](NO_3)_2/\gamma$-$Al_2O_3$ Pellet

Figure 5.6 (a) shows an optical micrograph of a bisected $[Ni(en)_3](NO_3)_2/\gamma$-$Al_2O_3$ pellet after drying. A crust of 160 μm $[Ni(en)_3](NO_3)_2$ crystallites is clearly seen close to the edges of the catalyst body (egg-shell distribution of Ni). These crystallites formed during drying, the nucleation points probably being the pore mouths on the outer surface of the catalyst body. Figure 5.6 (b) shows the energy dispersive spectrum near the edges of the catalyst body prior to calcination. This spectrum contains several peaks between 20 to 68 keV in addition to the expected $Ni_{K\alpha}$ fluorescence line. By comparison with a high quality angular dispersive pattern (standard lab-based XRD pattern) of unsupported $[Ni(en)_3](NO_3)_2$ crystals (Figure 5.7 (a)) it was possible to assign the peaks at 26.1, 29.6, 36.2, 37.5, 39.3, 44.2, 58.6, 61.0, 63.4 and 67.2 keV to the $[Ni(en)_3](NO_3)_2$ phase. In addition, two peaks due to the γ-Al_2O_3 support were identified at 51.9 and 73.1 keV, which corresponded to the reflections (400) and (440).[10]

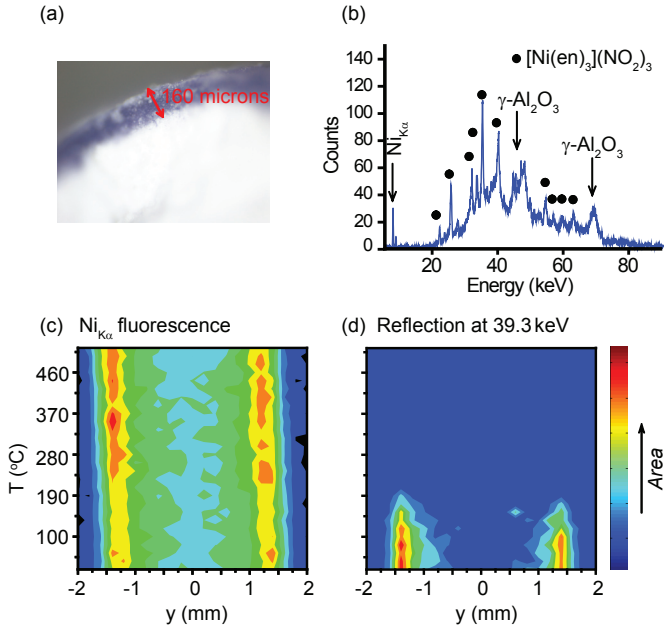

Figure 5.6. (a) Optical micrograph of the dried and bisected $[Ni(en)_3](NO_3)_2/\gamma$-$Al_2O_3$ pellet, (b) Energy dispersive spectrum collected by TEDDI from the edge of the pellet before calcination. The $Ni_{K\alpha}$ fluorescence signal is indicated together with the diffraction peaks of the $[Ni(en)_3](NO_3)_2$ crystals and of γ-Al_2O_3. (c) and (d) YT maps in the $[Ni(en)_3](NO_3)_2/\gamma$-$Al_2O_3$ pellet for (c) the $Ni_{K\alpha}$ fluorescence and (d) the diffraction peak at 39.3 keV of the $[Ni(en)_3](NO_3)_2$ crystalline phase. The y = 0 point corresponds to the center of the pellet.

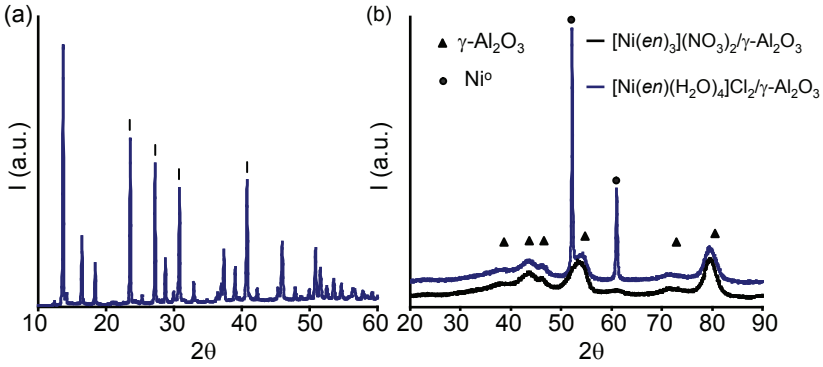

Figure 5.7. XRD patterns of (a) unsupported $[Ni(en)_3](NO_3)_2$ crystallites, the diffraction lines that are observed in the TEDDI experiments are marked with black lines; and of (b) crushed $[Ni(en)_3](NO_3)_2/\gamma$-$Al_2O_3$ pellets (black) and crushed $[Ni(en)(H_2O)_4]Cl_2/\gamma$-$Al_2O_3$ pellets (blue) after calcination. The diffraction lines of the γ-Al_2O_3 support and of metallic Ni are also indicated.

The YT maps in Figures 5.6 (c) and (d) illustrate the distribution of Ni (amorphous and crystalline) and of crystalline $[Ni(en)_3](NO_3)_2$ with calcination temperature, respectively. From these maps an initial Ni egg-shell distribution was deduced, corresponding with the optically observed distribution in Figure 5.6 (a). The fluorescence map indicates that Ni, regardless its crystalline structure, was mainly concentrated at the edges of the pellet, although some was present in the core. However, as the map of the crystalline $[Ni(en)_3](NO_3)_2$ indicated a sharp egg-shell profile of about 200 μm, (c.f. 160 μm observed optically) we can conclude that the core Ni was amorphous in structure. Moreover, the $[Ni(en)_3](NO_3)_2$ crystals disappeared rapidly when the sample was heated above 190 °C, indicating its decomposition to primarily an amorphous state. Still, by using the fluorescence data it was determined that the Ni remained at the edges of the pellet and did not migrate towards the core.

Furthermore, a detailed examination of the energy dispersive spectra indicated the presence of very small metallic Ni particles forming at higher temperatures. As an example, the spectra measured at the edge of the pellet during the calcination are given in Figure 5.8. In them, a very weak diffraction peak appears at 57.6 keV at around 400 °C together with a shoulder on the low energy side (49.8 keV) of the Al_2O_3 diffraction peak at 51.9 keV. These two peaks, at 49.8 keV and 57.6 keV, are consistent with the (111) and (200) reflections of fcc (face-centered cubic) Ni.[11] It must be noted that from the TEDDI experiments it cannot be deduced which fraction of the Ni species are present as metallic nanoparticles. From literature we estimate that approximately 20 % of the Ni was present as metallic nanoparticles.[5] For comparison purposes, Figure 5.8 (c) shows the energy dispersive spectrum at the edge of the pellet at 500 °C (1) together with other reference patterns: an energy dispersive spectrum on a γ-Al_2O_3 pellet without impregnation (the peak at 57.6 keV is not observed), the XRD pattern (in energy units) of a crushed post-calcined pellet which also contains a small peak at 57.6 keV, and the energy dispersive spectrum at the edge of a sample which contains large metallic Ni particles on γ-Al_2O_3.

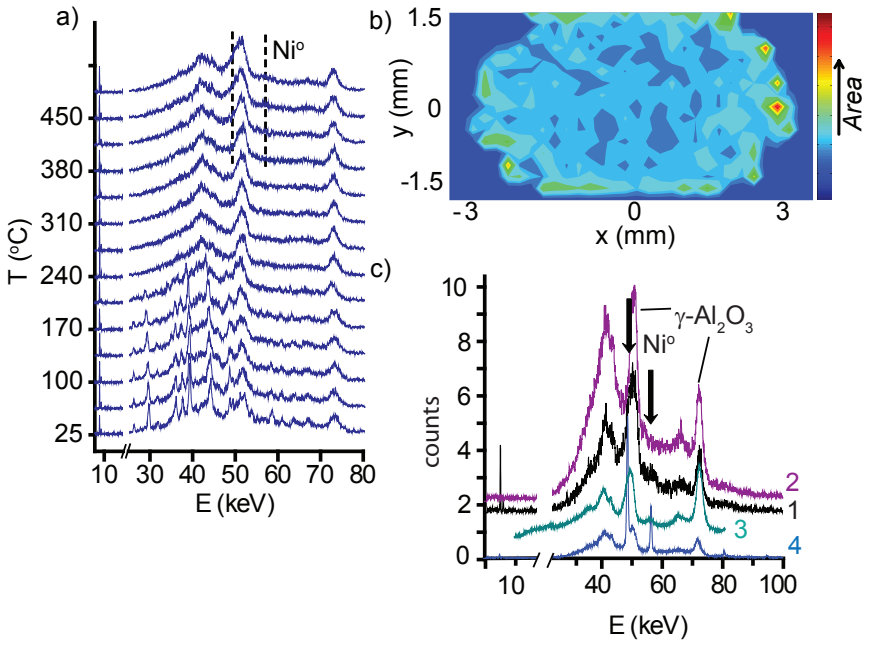

Figure 5.8. (a) Energy dispersive spectra collected at the edge of the $[Ni(en)_3](NO_3)_2$/γ-Al_2O_3 pellet during the YT scanning experiment. The weak diffraction peaks of metallic Ni are marked with dashed lines. It is noted that the patterns at low temperatures (< 190 °C) also show the diffraction peaks of the $[Ni(en)_3](NO_3)_2$ precursor salt. (b) XY concentration map of metallic Ni after calcination, constructed from the (200) reflection. (c) Spectrum at 500 °C at the edge of the $[Ni(en)_3](NO_3)_2$/γ-Al_2O_3 pellet (1) together with other reference patterns: γ-Al_2O_3 (2), XRD on the crushed $[Ni(en)_3](NO_3)_2$/γ-Al_2O_3 pellet after calcination at 500 °C (3), large particles of Ni° on γ-Al_2O_3 ($[Ni(en)(H_2O)_4]Cl_2$/γ-Al_2O_3 pellet) (4).

Figure 5.8 (b) shows the XY map of the metallic Ni distribution after calcination at 500 °C derived from the fit of the (200) reflection, and indicates that the metal is also present in an egg-shell distribution. From a Debye-Scherrer analysis on the crushed post-calcination pellet (standard XRD) the size of these particles was determined to be 5 nm on average, which was also confirmed by TEM measurements, as illustrated in Figure 5.9 (b).[12]

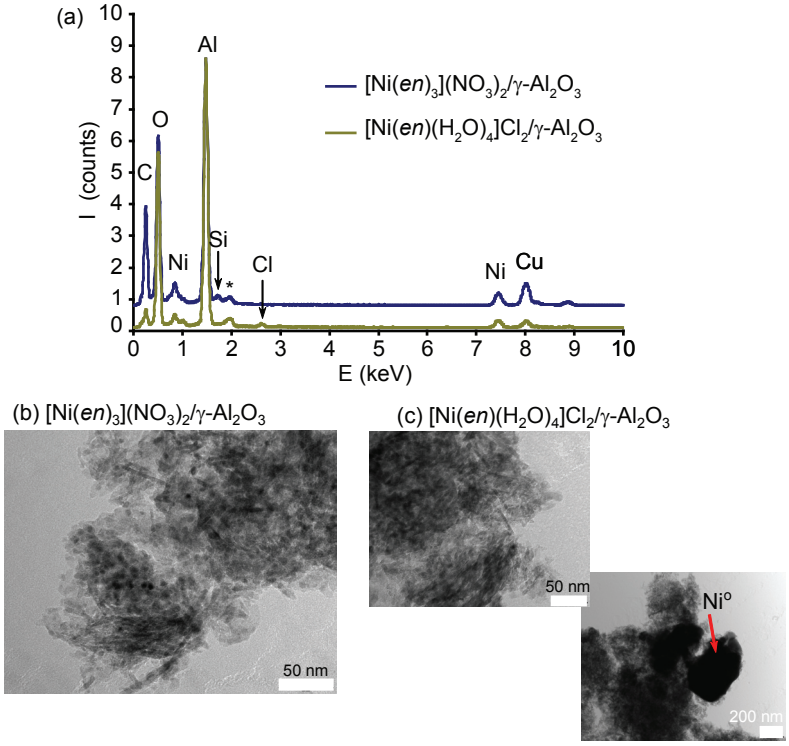

Figure 5.9. (a) EDX spectra obtained on a crushed $[Ni(en)_3](NO_3)_2/\gamma\text{-}Al_2O_3$ pellet (blue) and on a crushed $[Ni(en)(H_2O)_4]Cl_2/\gamma\text{-}Al_2O_3$ pellet (green) after calcination. The peak labeled with * is a satellite peak of Al; and TEM images collected on (b) a crushed $[Ni(en)_3](NO_3)_2/\gamma\text{-}Al_2O_3$ pellet and on (c) a crushed $[Ni(en)(H_2O)_4]Cl_2/\gamma\text{-}Al_2O_3$ pellet.

Formation of metallic Ni particles during the preparation of powdered Ni catalysts from nickel-ethylenediamine precursors by calcination in an inert atmosphere has been previously reported.[1-4] This phase formation has been assigned to the generation of H_2 as a decomposition product of ethylenediamine. Similarly, other chelating agents have been studied that yield nickel nanoparticles, since the decomposition mechanism of the chelating ligand is similar.[13] With these experiments, we demonstrate that this method yields small metallic particles also in the preparation of industrial-like catalysts based on mm-sized bodies.

In addition to this, after calcination the pellet was observed to be entirely black, suggestive of the presence of carbon on the catalyst body. This was confirmed by ex situ EDX analysis on the crushed pellets, as presented in Figure 5.9 (a). The

Cu detected comes from the sample grid. Besides Al, O and Ni, which are the main components in both samples, Si was also detected. This element was probably an impurity of the alumina support. On the other hand, part of the carbon detected came from the sample holder. However, the intensity of the carbon peak was very high on the $[Ni(en)_3](NO_3)_2/\gamma$-$Al_2O_3$ pellet, suggesting that this sample contained more C. The presence of carbon on this type of catalysts originates from the incomplete decomposition of the ethylenediamine ligand under an inert atmosphere due to the low amount of oxidizing agent (nitrates from the nickel precursor).[4, 5] Most likely, this carbon then surrounded the nickel particles preventing their oxidation to NiO. Therefore, to obtain a usable catalyst containing Ni, the pellets must be further activated by a reduction or calcination (in air) step to remove the carbonaceous compounds.

The various YZ distribution maps of the $[Ni(en)_3](NO_3)_2$ precursor recorded during calcination are presented in Figure 5.10 and represent the interior of the γ-Al_2O_3 catalyst body.

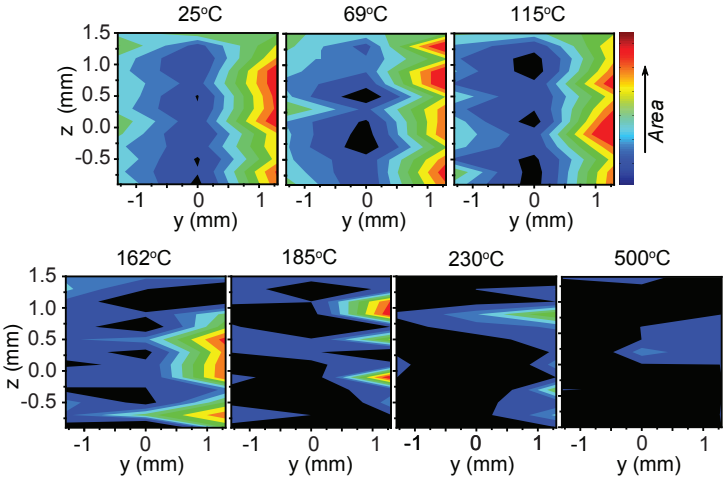

Figure 5.10. YZ maps of the $Ni(en)_3(NO_3)_2$ diffraction peak at 39.3 keV during the calcination process of the dried $[Ni(en)_3](NO_3)_2/\gamma$-$Al_2O_3$ pellet. The black regions indicate the absence of this peak, while the red regions indicate high concentrations.

As expected, these maps also show the breakdown of the complex as the temperature was increased during calcination. The YZ map at 25 °C confirms the $[Ni(en)_3](NO_3)_2$ crystalline egg-shell distribution throughout the whole pellet indicated by the YT map (Figure 5.6 (d)). Interestingly, the distribution was not completely symmetrical at 25 °C, as concluded from the red-coded regions only present on one side of the catalyst body. These irregularities may occur for a number of reasons, such as inhomogeneities in the support structure, or manipulation of the catalyst during its preparation.[14, 15] The YZ maps indicate that the precursor starts decomposing at around 70 °C, and by 190 °C it has decomposed into a non-crystalline phase. The complex breakdown appears to occur at a much lower temperature than observed in some previous studies performed by Negrier *et al*.[5] who reported, from mass spectrometry (MS), that the decomposition of $[Ni(en)_3](NO_3)_2/\gamma\text{-}Al_2O_3$ under argon takes place at 350 °C. This temperature difference suggests that even though the $[Ni(en)_3](NO_3)_2$ precursor looses its crystallinity at low temperatures, possibly due to melting or amorphization, the decomposition products are not released until higher temperatures. The YZ maps also demonstrate that the decomposition actually takes place unevenly over the pellet, occurring first in the core and then spreading towards the edges.

In summary, the calcination under N_2 of a $[Ni(en)_3](NO_3)_2/\gamma\text{-}Al_2O_3$ pellet leads to approximately 20 % of Ni as 5-nm metallic Ni crystallites. The precursor salt, which appears in an egg-shell distribution before calcination, decomposes at 190 °C; and this Ni profile is retained after calcination in the form of metallic Ni particles (at around 400 °C) protected with a carbon layer.

2. TEDDI During the Calcination of the $[Ni(en)(H_2O)_4]Cl_2/\gamma\text{-}Al_2O_3$ Pellet

Figure 5.11 shows the YT maps of the Ni distribution (both fluorescence and diffraction) constructed from various peaks observed in the energy dispersive spectra during the calcination of the $[Ni(en)(H_2O)_4]Cl_2/\gamma\text{-}Al_2O_3$ pellet.

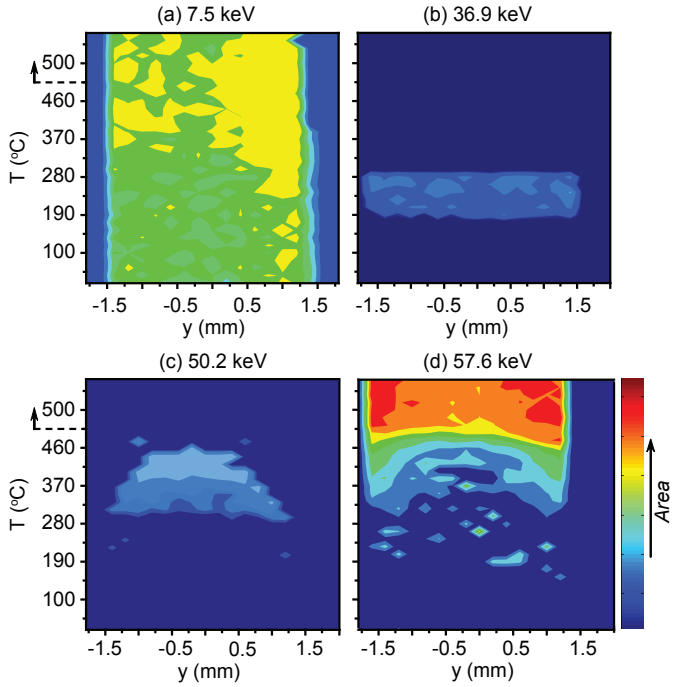

Figure 5.11. YT maps of (a) Ni fluorescence at 7.5 keV ($Ni_{K\alpha}$); (b) the diffraction peak at 36.9 keV (unknown Ni-containing crystalline phase), (c) the 50.2 keV (101) reflection of Ni_3C; and (d) the 57.6 keV (200) reflection of metallic fcc Ni, all in the $[Ni(en)(H_2O)_4]Cl_2/\gamma$-$Al_2O_3$ pellet. The red color represents regions where the concentration of the corresponding Ni species is the highest.

Prior to calcination the $[Ni(en)(H_2O)_4]Cl_2/\gamma$-$Al_2O_3$ showed no Ni-related crystalline peaks, whilst the Ni fluorescence YT map revealed an even distribution of Ni throughout the body of the pellet, as illustrated in Figure 5.11 (a). Additionally, UV-Vis-NIR micro-spectroscopy confirmed this rather homogeneous distribution, as shown in Figure 5.12. This technique is explained in detail in Chapters 1 - 3.

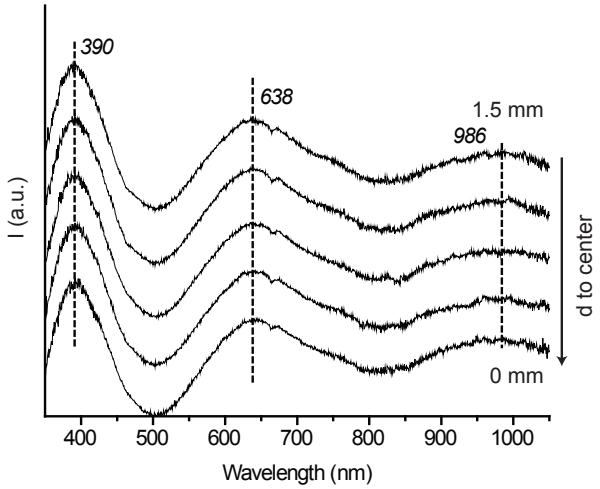

Figure 5.12. Space resolved UV-Vis-NIR spectra from the edge to center of a bisected $[Ni(en)(H_2O)_4]Cl_2/\gamma\text{-}Al_2O_3$ catalyst body after drying at 25°C.

The space resolved UV-Vis spectra in Figure 5.12 show a uniform distribution of the three bands centered at 390, 638 and above 900 nm. These bands are assigned to the three spin allowed d-d transitions of Ni^{2+} in an octahedral environment and correspond to the complex $[Ni(en)(H_2O)_4]^{2+}$ grafted to the alumina surface, with the consequent formation of a structure similar to $[Ni(en)(H_2O)_2(Al\text{-}O)_2]$, where Al-O represent oxygen atoms from the alumina surface.[4, 16] More details on the interactions of this metal-ion complex with the alumina surface during the impregnation and drying steps can be found in Chapter 3.

Figure 5.11 (a) illustrates that, as the sample was heated, an increase in the Ni fluorescence intensity occurred with temperature. This can be accounted for by changes in the density of the sample as the precursor decomposed. Still, this map indicates a rather uniform distribution of Ni along the *y* direction of the catalyst body regardless of its molecular structure.

Interestingly, and unlike the $[Ni(en)_3](NO_3)_2/\gamma\text{-}Al_2O_3$ pellet, the calcination of the $[Ni(en)(H_2O)_4]Cl_2/\gamma\text{-}Al_2O_3$ pellet lead to the formation of two intermediate crystalline phases before the formation of metallic Ni, as illustrated in Figures 5.11 (b) – (d). The energy dispersive spectra measured at the edge of the pellet during the calcination can be found Figure 5.13.

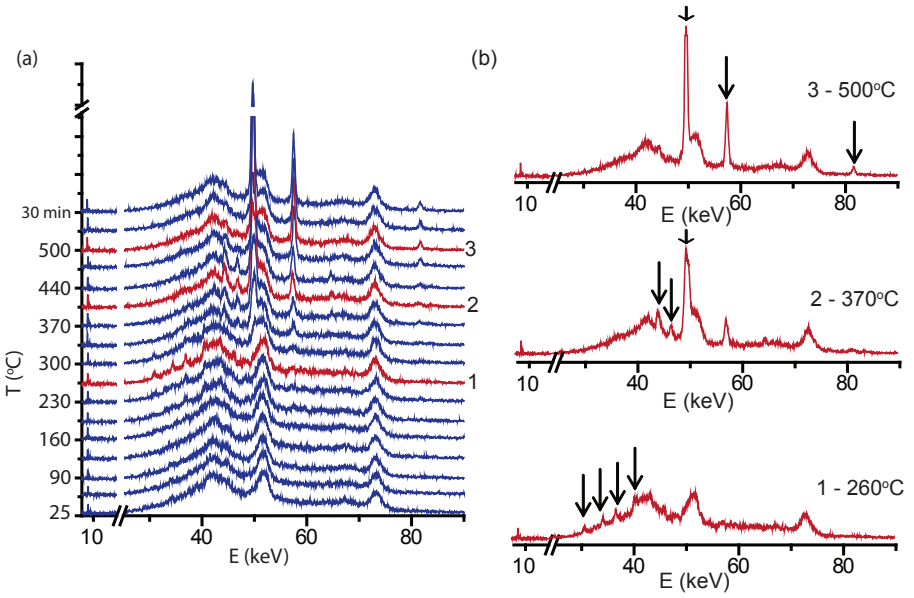

Figure 5.13. (a) Energy dispersive spectra collected at the edge of the [Ni(*en*)$(H_2O)_4$]Cl_2/γ-Al_2O_3 pellet during the YT experiment. The spectra in red contain the strongest diffraction lines of the crystalline phases formed during the calcination process. (b) Individual spectra of the different crystalline phases formed during the calcination. The diffraction lines of interest are indicated with arrows.

Several diffraction peaks were detected between 180 – 270 °C at 30.9, 33.3, 34.3, 36.9, 40.5, 53.5, 44.3 and 46.1 keV, with the most intense at 36.9 and 40.5 keV. Since these peaks could not be assigned to a particular phase we propose that a restructuring of the Ni species on the alumina surface is responsible for the changes in the energy dispersive spectra, which yielded an ordered and unknown Ni phase. The essentially uniform blue color in the YT map of the peak at 36.9 keV (Figure 5.11 (b)) indicates a rather uniform distribution along the catalyst body of this unknown Ni-containing crystalline phase. Moreover, this temperature range was in line with the release of NH_3 and H_2O followed with MS on a similar sample (3 wt% Ni as [Ni(*en*)$(H_2O)_4$]Cl_2/γ-Al_2O_3), as illustrated in Figure 5.14.

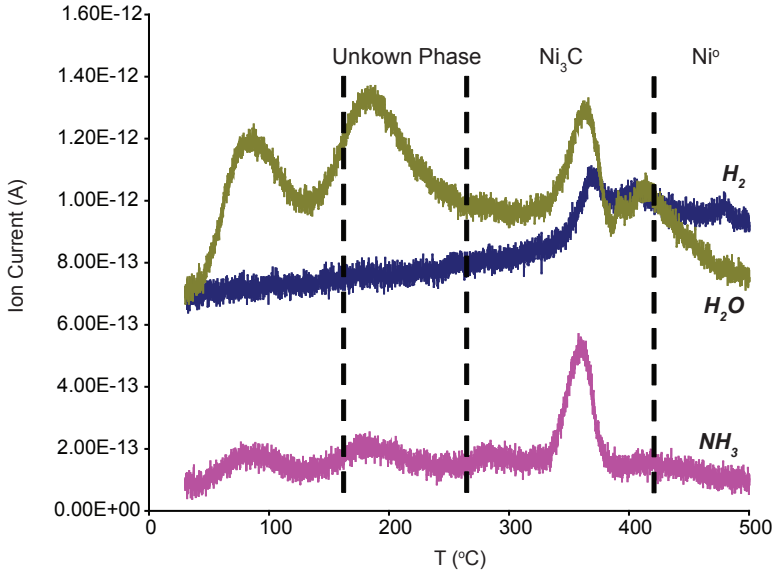

Figure 5.14. MS thermogram during the calcination in Ar of crushed 3 wt% [Ni(*en*)$(H_2O)_4$] Cl_2/γ-Al_2O_3 pellets. The temperature regions in which crystalline phases were detected with TEDDI on the 10 wt% pellet are indicated.

Above 270 °C, the first Ni crystalline phase transforms into a second crystalline phase which is stable from 270 °C to approximately 430 °C. Several diffraction peaks were measured at 44.3, 46.8, 50.2 and 64.7 keV. These peaks were assigned, respectively, to the reflections (100), (002), (101) and (102) of hexagonal Ni_3C.[17] The low intensity of these peaks suggests that this phase is present as a maximum of 40 % of the Ni species in the core of the pellet, while in the edges less than 20 % of Ni appears as Ni_3C. Figure 5.11 (c) shows the YT map of the peak at 50.2 keV and reveals that the stability of Ni_3C with temperature is dependent on its location in the catalyst body, with a decomposition front moving towards the core with increasing temperature. At the edges of the pellet, Ni_3C decomposes almost immediately after being formed, whilst in the core it is stable up to 430 °C and corresponds well with the known decomposition temperature of Ni_3C in an inert atmosphere, eq. (1):[18]

$$Ni_3C \longrightarrow 3\ Ni^{o} + C\ (s, amorphous) \qquad (1)$$

Finally, Figure 5.11 (d) shows the formation of fcc metallic Ni, XY map of the (200) reflection. Similarly as in the $[Ni(en)_3](NO_3)_2/\gamma$-$Al_2O_3$ pellet, the appearance of the reflections (111), (200) and (222) of fcc metallic Ni at high temperatures is observed. However, the $[Ni(en)(H_2O)_4]Cl_2/\gamma$-$Al_2O_3$ pellet shows very narrow and intense peaks, which suggests a large amount of Ni species converted into relatively large metallic Ni particles. This phase was initially observed at around 300 °C, only at the edges of the catalyst and became uniform throughout the body at 435 °C. At 500 °C, the sample was held at temperature for 30 min, during which time the concentration of Ni increased at the edges of the pellet, indicating that sintering occurred.

Figure 5.15 (a) shows the XY map of metallic Ni immediately after calcination, and indicates a rather uniform distribution of this phase (regions in green color), although there was some higher concentrations at the edge of the sample (yellow/orange regions).

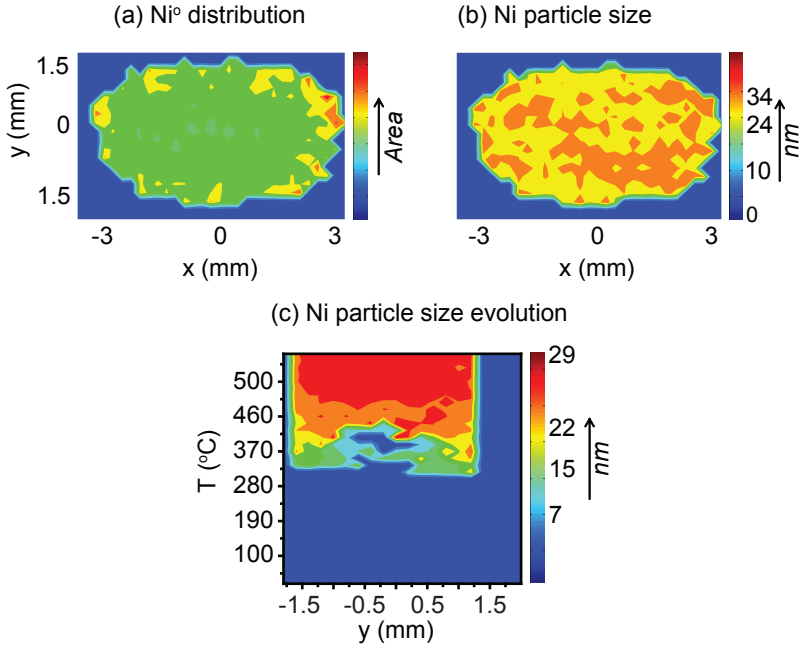

Figure 5.15. XY maps of (a) metallic Ni distribution in the $[Ni(en)(H_2O)_4]Cl_2/\gamma$-$Al_2O_3$ pellet after calcination at 500 °C, (b) particle size distribution of metallic Ni in the same slice of the pellet after calcination at 500 °C, and (c) evolution of metallic Ni crystallites as a function of the *y* direction of the catalyst body. The red color indicates regions of (a) higher concentration of metallic Ni, or (b, c) larger particle size. The blue color indicates the absence of metallic Ni.

Using the full-width-at-half-maximum (FWHM) of the metallic Ni (200) reflection and a Debye-Scherrer analysis, the particle size was estimated to be on average 24-34 nm, as illustrated in Figure 5.15 (b). This value compared closely with that calculated from the ex situ XRD pattern, shown in Figure 5.7 (b), measured on a crushed pellet (39 nm). Thus, relatively large nanoparticles of metallic Ni are formed when the Ni chloride precursor salt is used in equimolar concentrations of Ni and ethylenediamine.

Figure 5.15 (c) illustrates the YT map of the evolution of metallic Ni crystallites with calcination temperature. The particle size growth was estimated assuming that at 500 °C the average particle size was 29 nm (average between 24 - 34 nm). The map indicates that metallic Ni particles appear readily at 300 °C, preferentially towards the edge of the pellet, whilst they are not observed in the core until 370 °C. Thus, between 370 – 430 °C, both Ni_3C and metallic Ni coexist in the pellet, as can be deduced from Figures 5.11 (c) and (d). At around 435 °C, there is a uniform distribution of metallic Ni particles, which sinter to form larger particles at around 480 °C. Furthermore, unlike the $[Ni(en)_3](NO_3)_2/\gamma\text{-}Al_2O_3$ pellet, the $[Ni(en)(H_2O)_4]Cl_2/\gamma\text{-}Al_2O_3$ pellet was observed to be grey rather than black after calcination, indicating the deposition of less carbon, which was confirmed ex situ using EDX analysis (Figure 5.9 (a)).

To summarize, the use of $[Ni(en)(H_2O)_4]Cl_2$ as a precursor in the preparation of metallic Ni catalysts results in the formation of relatively large metallic Ni particles with a high degree of reduction when compared to $[Ni(en)_3](NO_3)_2$ (c.f. 30 - 40 nm vs. 5 nm). This makes the $[Ni(en)(H_2O)_4]Cl_2/\gamma\text{-}Al_2O_3$ catalyst less interesting for industrial applications. The formation of larger particles indicates that Ni-oxy-chloride species must become mobile during the calcination process. Moreover, the mobility of Ni species starts at around 180 °C, the temperature at which the first intermediate crystalline phase was detected, which suggests that this phase is implicit in the aggregation of the metal particles in this material. Moreover, large nanoparticles and a high heterogeneity in the particle size distribution of metallic Ni was confirmed by TEM measurements (Figure 5.9 (c)). Even though TEDDI enables to visualize the structural changes of Ni during the calcination process in a space resolved manner, the mechanism by which large metallic Ni particles formed could not be deduced. With the knowledge gained by the TEDDI technique, a schematic of the preparation of metallic Ni catalyst bodies when the precursor salts $[Ni(en)(H_2O)_4]Cl_2$ and $[Ni(en)_3](NO_3)_2$ are used can be proposed, as illustrated in Figure 5.16.

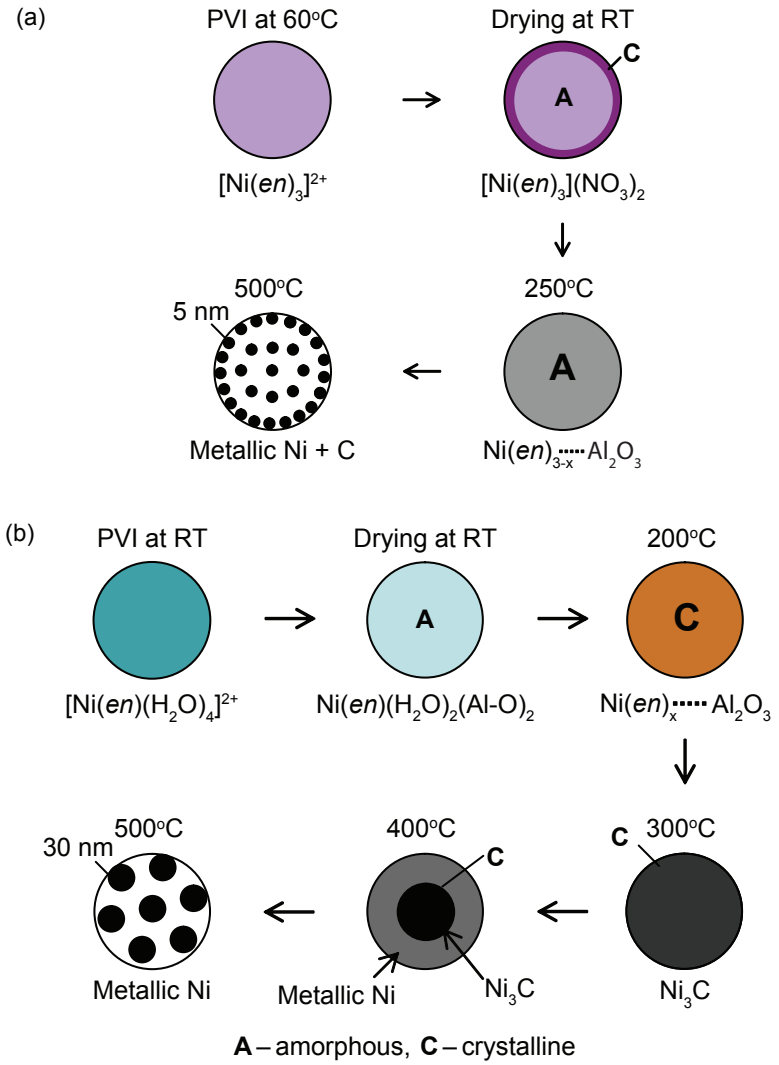

Figure 5.16. Phase transformation of (a) the $[Ni(en)_3](NO_3)_2/\gamma$-$Al_2O_3$ pellet and (b) the $[Ni(en)(H_2O)_4]Cl_2/\gamma$-$Al_2O_3$ pellet during catalyst preparation from pore volume impregnation (PVI) up to calcination at 500 °C in an N_2 gas atmosphere. The different colors represent the different phases present. After calcination at 500 °C, the particle size of metallic Ni is also indicated.

As illustrated in Figure 5.16 (a), pore volume impregnation of $[Ni(en)_3](NO_3)_2$ on γ-Al_2O_3 pellets yields a uniform profile of this Ni^{2+} complex along the catalyst body before drying. Drying at 20 °C induces the crystallization of large $[Ni(en)_3](NO_3)_2$ particles towards the outer rim of the catalyst bodies, as inferred from the sharp diffraction peaks measured at low temperatures. During the calcination of this sample, the precursor $[Ni(en)_3](NO_3)_2$ decomposes at 190 °C forming an amorphous intermediate phase which remains in an egg-shell profile. Above 385 °C, small metallic Ni crystallites of around 5 nm size are formed (~ 20 % of the Ni present), in the same egg-shell distribution, covered by carbonaceous species.

On the other hand, pore volume impregnation of $[Ni(en)(H_2O)_4]Cl_2$ yields a uniform macro-distribution of Ni before drying, that remains unchanged during the subsequent preparation steps. Drying at 25 °C creates ligand-exchange reactions of the precursor complex with the hydroxylated surface of the γ-Al_2O_3 support, forming $[Ni(en)(H_2O_2)(Al\text{-}O)_2]$ species. At 180 °C, the precursor complex undergoes decomposition as well as restructuring on the γ-Al_2O_3 surface and transforms into an intermediate crystalline phase, which is stable up to 270 °C. At this temperature, Ni restructures again partly forming Ni_3C species, and its stability depends on the location within the catalyst bodies. In this way, Ni_3C at the outer rim of the catalyst body decomposes readily forming metallic Ni at around 300 °C, whilst at the edges it is stable up to 430 °C. This preparation method yields a large amount of Ni species converted into metallic Ni particles of sizes around 30 - 40 nm, which are less-desired for catalytic applications due to their low activity.

Conclusions

TEDDI has been successfully employed to study the calcination process of a heterogeneous catalyst body and detailed insight into the changes in the structural composition at the macroscopic level in a non-invasive manner was obtained. This technique has demonstrated that the formation of an active component is a multi-step evolution process and that this process shows significant spatial variation. It was revealed that, if $[Ni(en)(H_2O)_4]Cl_2$ is used as a precursor for Ni/Al_2O_3 catalysts, this precursor forms an amorphous structure evenly distributed on the support surface before thermal treatment. Moreover, its decomposition during the thermal treatment undergoes through two intermediate crystalline phases among other less ordered ones. Furthermore, metallic Ni nanoparticles (heterogeneous particle size

distribution with an average of 30 nm) with high degree of reducibility appear at the edges already at 280 °C, whilst in the core they are formed at around 450 °C. On the other hand, if the catalyst is prepared from the $[Ni(en)_3](NO_3)_2$ precursor, an egg-shell distribution of large $[Ni(en)_3](NO_3)_2$ crystals is measured before thermal treatment. Still, the breakdown of the precursor, which starts at around 70 °C and finishes at 190 °C as an amorphous structure, occurs forming partly a very narrow particle size distribution centered at 5 nm of metallic Ni crystallites (20 % of the total Ni species). These particles appear at around 400 °C in an egg-shell distribution.

Acknowledgments

Dr. Matthew G. O'Brien (Inorganic Chemistry and Catalysis group, Utrecht University) and Dr. Simon D. M. Jacques (University College London, UK) are kindly acknowledged for their help during the experiments. The EPSRC/CCLRC is acknowledged for beamtime on station 16.4 and Dave Taylor for technical assistance at the beam line. Taha Sochi (University College London, UK) is thanked for the development of the software used to analyze the data, and Cor van der Spek and Marjan Versluijs-Helder (Inorganic Chemistry and Catalysis group, Utrecht University) for TEM measurements and MS experiments, respectively. Prof. dr. Paul Barnes (Department of Chemistry, University College London, UK) is thanked for valuable discussions.

References

[1] J.-F. Lambert, M. Hoogland, M. Che, *J. Phys. Chem. B* **1997**, *101*, 10347.
[2] F. Negrier, E. Marceau, M. Che, *Chem. Comm.* **2002**, 1194.
[3] F. Negrier, É. Marceau, M. Che, D. de Caro, *C. R. Chimie* **2003**, *6*, 231.
[4] F. Negrier, E. Marceau, M. Che, J. M. Giraudon, L. Gengembre, A. Lofberg, *J. Phys. Chem. B* **2005**, *109*, 2836.
[5] F. Négrier, E. Marceau, M. Che, J.-M. Giraudon, L. Gengembre, A. Löfberg, *Catal. Lett.* **2008**, *124*, 18.
[6] S. Schimpf, C. Louis, P. Claus, *Appl. Catal. A: General* **2007**, *318*, 45.
[7] K.-Q. Sun, E. Marceau, M. Che, *Phys. Chem. Chem. Phys.* **2006**, *8*, 1731.
[8] J. Park, J. R. Regalbuto, *J. Colloid Interface Sci.* **1995**, *175*, 239.
[9] O. Lazzari, S. Jacques, T. Sochi, P. Barnes, *The Analyst* **2009**.
[10] G. Gutiérrez, A. Taga, B. Johansson, *Phys. Rev. B* **2001**, *65*, 012101.
[11] E. A. Owen, E. L. Yates, *Philos. Mag.* **1936**, 809.

[12] A. D. Krawitz, *Introduction to Diffraction in Materials Science and Engineering*, John Wiley & Sons, New York, **2001**.
[13] P. Afanasiev, S. Chouzier, T. Czeri, G. Pilet, C. Pichon, M. Roy, M. Vrinat, *Inorg. Chem.* **2008**, *47*, 2303.
[14] A. M. Beale, S. D. M. Jacques, J. A. Bergwerff, P. Barnes, B. M. Weckhuysen, *Angew. Chem. Int. Ed.* **2007**, *46*, 8832.
[15] L. Ruffino, R. Mann, R. Oldman, E. H. Stitt, E. Boller, P. Cloetens, M. DiMichiel, J. Merino, *Can. J. Chem. Eng.* **2005**, *83*, 132.
[16] L. Espinosa-Alonso, K. P. de Jong, B. M. Weckhuysen, *J. Phys. Chem. C* **2008**, *112*, 7201; *Chapter 3 in this PhD thesis.*
[17] S. Nagakura, *J. Phys. Soc. Jpn.* **1958**, *13*, 1005.
[18] Y. Leng, L. Xie, F. Liao, J. Zheng, X. Li, *Thermochim. Acta* **2008**, *473*, 14.

Chapter 6

Summary

The goal of this PhD thesis was the development of new space and time resolved spectroscopic techniques to be applied in the characterization of mm-sized catalyst preparation processes, including impregnation, drying and thermal treatment. Hence, with these techniques in hand new insight into the physicochemical processes involved during these catalyst preparation processes is obtained which will help to underpin the rational design of heterogeneous catalysts.

Ni and Pd/ γ-Al_2O_3 hydrogenation catalysts were chosen as model systems to explore the possibilities of two invasive (UV-Vis-NIR and IR micro-spectroscopies) and two noninvasive (MRI and TEDDI) characterization methods. Different experimental conditions were tuned in order to investigate the role of the metal-support interface in the preparation of these catalysts, and the capabilities and limitations of the different space and time resolved spectroscopic techniques have been evaluated.

Chapters 2 and 3 focus on the uses of UV-Vis-NIR and IR micro-spectroscopies to investigate the impregnation, drying and calcination steps during the preparation of Ni and Pd/ γ-Al_2O_3 hydrogenation catalysts. In **Chapter 2**, UV-Vis-NIR micro-spectroscopy is employed to assess the dynamics and speciation of $[PdCl_4]^{2-}$ within γ-Al_2O_3 pellets. To do so, the solution pH and equilibration time were tuned, and the addition of different amounts of Cl^- (aq) ions was investigated. From the results obtained, a protocol to prepare 0.2 wt % Pd/γ-Al_2O_3 catalysts with different Pd macro-distributions was designed. This technique also revealed that the $[PdCl_4]^{2-}$ or $[PdCl_3(H_2O)]^-$ complexes in the impregnation solutions hydrolyzed to form $[PdCl_2(OH)_2]^{2-}$ upon impregnation, and that depending on the solution pH, equilibration time and concentration of Cl^- (aq) ions, the Pd molecular structure

further changed to form $[PdCl(OH)_3]^{2-}$ or $[Pd(OH)_4]^{2-}$. A UV-Vis micro-spectroscopic study on dried and calcined pellets revealed that grafting of these complexes occurred upon drying and ligand exchange reactions with the γ-Al_2O_3 surface took place. Furthermore, during this step Cl^- ions entered again the 1st coordination sphere of Pd^{II} and structures similar to $[PdCl_4]^{2-}$ and $[PdCl_3(OH)]^{2-}$ were regenerated. Upon calcination no redistribution of Pd was measured, and the presence of Cl^- ions closely attached to the Pd phase was deduced, proving the poisonous effect that Cl^- ions is known to have in Pd catalysts.

Chapter 3 elaborates on the influence of ethylenediamine ligands on the Ni^{2+} molecular structure and dynamics upon impregnation and after drying. This study was performed by means of UV-Vis-NIR and IR micro-spectroscopies and revealed the complementary effect that the different hydroxyl surface sites of the alumina support have on the stability of the precursor Ni^{2+} complexes inside the pores of the support. Ligand exchange reactions between the water ligands in $[Ni(en)_x(H_2O)_{6-2x}]^{2+}$ (x = 0 - 3) and the alumina surface hydroxyl groups upon impregnation were disclosed, which yielded a trend on the strength of adsorption of the different complexes as follows: $[Ni(en)(H_2O)_4]^{2+} > [Ni(en)(H_2O)_2]^{2+} \sim [Ni(H_2O)_6]^{2+} > [Ni(en)_3]^{2+}$, the latter did not interact with the surface upon impregnation. It was also revealed that most likely the hydroxyl groups involved are the basic ones. This study also put forward that these interactions were responsible for the Ni and *en* profiles achieved after drying. The weaker the adsorption of the Ni^{2+} complex, the more egg-shell-like the Ni^{2+} and *en* profiles after drying, as obtained from both UV-Vis-NIR and IR micro-spectroscopies. The former provided insight in the Ni^{2+} coordination sphere in a space resolved manner, while the latter provided the macro-distribution of the *en* ligand.

Chapter 4 and 5 describe the applicability of the two noninvasive methods under study to characterize the preparation of Ni/γ-Al_2O_3 hydrogenation catalysts. ^{1}H-MRI is introduced in **Chapter 4** as an indirect characterization method for the impregnation step of paramagnetic metal-ions, such as Ni^{2+}. This method uses the influence that paramagnetic metal-ions have on the relaxation times of protons to deduce and monitor the dynamics of the metal-ion: the contrast in an NMR image is a direct measure of the NMR signal intensity of water protons. Since the NMR signal is dependent on the proton relaxation times, and these decrease in the presence of paramagnetic metal-ions, the metal-ion can be perfectly located in the catalyst body due to the different NMR signal intensities along the body. There are two

image contrast methods: T_1 and T_2. By using the T_2 image contrast, the dynamics of aqueous metal-ion complexes can be monitored quantitatively, as illustrated for the particular case of the $[Ni(H_2O)_6]^{2+}$ complex within γ-Al_2O_3 extrudates. The quantification can be done thanks to the construction of a calibration line between NMR signal intensities and $[Ni(H_2O)_6]^{2+}$ concentrations. It must be noted, however, that new calibration lines must be constructed for each system metal-ion - support since the NMR signal inside the pores of a support body is not only dependent on the concentration of the paramagnetic metal-ion precursor, but also on the impurities both in the impregnation solution and in the support and on the textural properties of the latter (pore size and structure). The potential of MRI to characterize the impregnation step of other systems was also investigated, and the two other systems described in this Chapter are the impregnation of $[Ni(\textit{edta}H_x)]^{(2-x)-}$ complexes and the co-impregnation of $[Ni(H_2O)_6]^{2+}$ and $[Ni(\textit{edta}H_x)]^{(2-x)-}$. The ^{1}H-MRI method can also be applied to monitor the dynamics of chelated complexes, such as $[Ni(\textit{edta}H_x)]^{(2-x)-}$. However, due to the large size of the *edta* ligand, the paramagnetic influence of the Ni^{2+} ions on the relaxation times of water protons is shielded and a different imaging method has to be used; namely, T_1 image contrast. This imaging method also gives contrast between regions with and without Ni^{2+} complexes, but it is not able to distinguish regions with different concentration of Ni^{2+}. Hence, it cannot be used quantitatively. Regarding the possibilities to visualize the dynamics of $[Ni(H_2O)_6]^{2+}$ and $[Ni(\textit{edta}H_x)]^{(2-x)-}$ when they are co-impregnated, the information obtained from the ^{1}H-MRI method by itself is difficult to evaluate. Nevertheless, the combination of this technique with others, such as UV-Vis-NIR micro-spectroscopy, provides a very powerful approach since the two of them together provide semi-quantitative insight in the location of the two metal-ion complexes. More specifically, $[Ni(\textit{edta}H_x)]^{(2-x)-}$ appears in an egg-shell distribution, while the $[Ni(H_2O)_6]^{2+}$ complex is present in a uniform manner. Furthermore, they provide input on the adsorption processes that each of them undergo on the alumina surface, but also between them. More specifically, electrostatic interactions between the two complexes were revealed, which could not be disclosed by each of the techniques if they were applied on their own.

Finally, **Chapter 5** introduces the potential of a synchrotron-based method to characterize the preparation of mm-sized catalyst bodies. In this chapter, the TEDDI technique is used to characterize in situ the thermal treatment of Ni/γ-Al_2O_3 pellets. To do so, an environmental cell was built which enabled to collect energy dispersive

spectra while performing the calcination treatment of two different samples. The systems chosen to investigate were $[Ni(en)_3](NO_3)_2$ and $[Ni(en)(H_2O)_4]Cl_2$ on Al_2O_3 pellets, and the thermal treatment performed was a calcination under N_2. This thermal treatment applied on Ni-*en* precursor catalysts yielded, depending on the molar Ni^{2+}:*en* ratio and the Ni precursor salt, small metallic Ni nanoparticles, and the formation of Ni aluminates could be partly avoided. The goal of these experiments was to visualize in 3D or 4D (*x*, *y*, *z* and/or time/temperature) the breakdown of the precursor complex and the genesis of final active phase. This technique provides fluorescence and diffraction data, thus, Ni^{2+} can be located and any crystalline phase can also be visualized within the catalyst body. From the results obtained, it can be concluded that the thermal treatment of a $[Ni(en)_3](NO_3)_2/\gamma\text{-}Al_2O_3$ pellet yield 5-nm metallic Ni nanoparticles in an egg-shell distribution, whilst in the case of $[Ni(en)(H_2O)_4]Cl_2/\gamma\text{-}Al_2O_3$ a very heterogeneous particle size distribution of metallic Ni nanoparticles centered at around 30 nm in a uniform profile is obtained.

Chapter 7

Outlook and Perspectives

Insight into the physicochemical processes involved during the preparation of catalyst bodies and, thus, a control on the preparation of catalyst bodies yields more efficient catalysts in chemical processes, and, hence, assists the improvement of chemical and technological development with the ultimate goal of sustainable development. The term "efficiency" is usually measured by two parameters: reactant conversion and product selectivity. The reactant conversion indicates the amount of reactant molecules that transform into products (regardless the product), whilst the product selectivity addresses the fraction of reactant molecules that have transformed into a specific product. Thus, higher conversions and selectivities mean less generated wastes, less resources (raw materials) needed and more economical efficiency, which results in a more sustainable society.

As described in this work, a large number of physicochemical parameters play an important role in the preparation of mm-sized catalyst bodies, and in order to obtain the optimum catalyst material a careful selection of all the ingredients in the impregnation solution containing the precursor of the active component, and of the support material must be made. Once the impregnation solution has been selected, other experimental conditions have to be chosen, such as equilibration times after impregnation, or the drying and thermal treatment conditions. All these factors will determine the final phase (metal or metal oxide) and dispersion of the active particles and their macro-distribution within the support body; and, thus, they will determine the efficiency of the catalyst in a chemical process.

As described in Chapter 1, the final macro-distribution and dispersion of the active material is affected by the interactions that take place between the metal-ion precursor and the support surface already during the impregnation step. The

adsorption process of a metal-ion (Ni and Pd) precursor on the support surface (γ-Al_2O_3) during this wet step of catalyst preparation has been dealt in Chapters 2 – 4, and different experimental conditions have been investigated. Important findings that could only be obtained thanks to space and time resolved spectroscopic characterization techniques have been reported along these chapters. For instance, Chapters 2 and 3 explore the speciation that different metal-ion precursors ($[PdCl_{4-x}(OH)_x]^{2-}$ and $[Ni(en)_x(H_2O)_{6-2x}]^{2+}$) undergo during their dynamics towards the core of γ-Al_2O_3 catalyst bodies, which is intrinsic to the mm length of catalyst bodies and which would not occur in the preparation of powdered catalysts. Hence, it can only be monitored by space resolved techniques, such as UV-Vis-NIR micro-spectroscopy. Additionally, the experiments described in Chapter 2 demonstrate the combined effect that the solution pH, the presence of Cl^- (aq) and the equilibration time have on the macro-distribution (and coordination sphere) of the initial $[PdCl_4]^{2-}$ on γ-Al_2O_3 catalyst bodies. In this way, it has been shown that $[PdCl_4]^{2-}$ is not stable in the presence of γ-Al_2O_3 and it hydrolyzes forming $[PdCl_{4-x}(HO)_x]^{2-}$. Moreover, the competitive adsorption between free Cl^- (aq) ions and $[PdCl_{4-x}(HO)_x]^{2-}$, which yields non-uniform Pd macro-distributions, has been clearly monitored with time; and the important role of the solution pH on the formation of one or another type of non-uniform Pd macro-distribution has been proven. Furthermore, the experiments explained in Chapter 3 serve as an example of how the hydroxyl groups of the alumina surface cannot be treated as a unique reactive species and shows how different hydroxyl groups with different acid-base properties and, thus, different reactivities can disturb the 1st coordination sphere of the metal-ion precursor complex upon impregnation. This Chapter also illustrates that the interactions between the metal-ion precursor complex and the support surface can determine the metal-ion profile, as concluded from the application of UV-Vis-NIR and IR micro-spectroscopies. In particular, the drying of impregnated $[Ni(en)_3]^{2+}$/γ-Al_2O_3 yields an egg-shell-like Ni profile thanks to the lack of interactions between this complex and the alumina surface during the impregnation step; whilst the same drying conditions of $[Ni(en)(H_2O)_4]^{2+}$/γ-Al_2O_3 pellets lead to uniform Ni profiles due to ligand exchange reactions during impregnation.

A major asset of MRI and TEDDI is their application to characterize catalyst bodies in a noninvasive manner, as presented in Chapters 4 and 5. As illustrated in Chapter 4, ^{1}H-MRI can be used in a very straightforward manner to monitor the impregnation process of paramagnetic metal-ion complexes and, when the ligands

surrounding the metal-ion are water molecules, the impregnation process can be monitored quantitatively. The possibility of quantifying impregnation processes is of great importance in catalyst design since understanding the molecular-transport kinetics is crucial to control the preparation of mm-sized catalysts. In this regard, these quantitative MRI experiments serve as an input to measure diffusion coefficients of different precursors inside the pores of support bodies, and for the development of kinetic models for the impregnation process. These models would be very useful to the industrial community for a faster design of new catalysts. Furthermore, a step forward in the applications of MRI is its application to study the co-impregnation of two metal-ion complexes. Even though, MRI by itself could not be used to monitor and discriminate between the two $[Ni(H_2O)_6]^{2+}$ and $[Ni(edtaH_x)]^{(2-x)-}$ co-impregnated complexes, this technique in combination with UV-Vis-NIR micro-spectroscopy did unravel additional adsorption processes between the two complexes depending on the solution pH.

Finally, Chapter 5 is focused on the TEDDI technique and its applications on catalyst preparation processes. Fairly important is the fact that this synchrotron-based technique is, for the moment, the only one that can be used in situ during the drying and thermal treatment steps of mm-sized catalyst bodies preparation processes. Thanks to this advantage, the genesis of Ni nanoparticles within γ-Al_2O_3 pellets has been visualized for the first time together with the breakdown of the precursor phase and the formation of, until now, unknown intermediate phases. Thus, this method can provide relevant input regarding the shape and size of the active particles in a catalytic material. Moreover, possible gradients of the shape and size of the active component along the catalyst body can be disclosed, which would provide enormous benefits when understanding the performance of the catalyst. This technique has, therefore, a great potential as a characterization method of mm-sized catalytic materials involved in a large number of thermal treatments in different conditions of temperature, pressure and ambients; which are sometimes required for catalyst activation, or which correspond to real conditions in relevant industrial processes.

In summary, the development of space and time resolved spectroscopic techniques to be applied in the field of, among others, mm-sized catalyst bodies preparation processes is of prime importance not only for the academic community but also for the chemical industry due to the current need in our society for sustainable development. These techniques will underpin the requirements to

prepare optimum and specific catalysts for specific applications. The possibility of utilizing these techniques in a quantitative and time resolved manner set the bases for modeling the kinetics of all time dependent processes. An example, mentioned above, is the possibility to model the diffusion kinetics of metal precursors within support bodied thanks to MRI, but another example could be to model the particle growth of the active component. One important issue that cannot be neglected in the design of efficient catalyst bodies and has not been discussed in this PhD thesis is the influence that the 3D network of the pore structure of a support body has on the dynamics of the precursor complex and growth and formation of the active component. These three are not only determined by the number and type of surface adsorption sites but also on the pore structure; namely, tortuosity of the pores, pore diameter and pore size distribution. Thus, the shaping of support bodies is also important. In this regard, not much attention has been paid for the moment on the effect that the 3D pore structure of the support body has on the genesis of the active component, and only few studies on the characterization of pre-shaped supports have been published.[1, 2] A technique that shows a great potential to characterize the pore structure of support and catalyst bodies is absorption tomography. Moreover, its combination with TEDDI would yield large input on the architecture of catalyst bodies since it would provide a picture of the pore network of the support and the active material in addition to space resolved input on the crystallinity of the sample. Figure 7.1 illustrates a reconstructed image obtained with absorption tomography on a XY slice of a calcined γ-Al_2O_3 pellet containing Na_2PdCl_4 (Pd 1 wt%) and NaCl (1.4 M). This sample which was prepared according to the protocol developed in Chapter 2 contains Pd in the core of the body, as deduced from the white spots in the image at positions close to the center of the pellet (x = y = 0 mm). The image shows the pore network of the core of the body. As illustrated in the Figure, this specific γ-Al_2O_3 pellet contains some voids in its pore structure of around 50-100 μm size (black circles). Additionally, two large Pd particles (white spots) can also be distinguished.

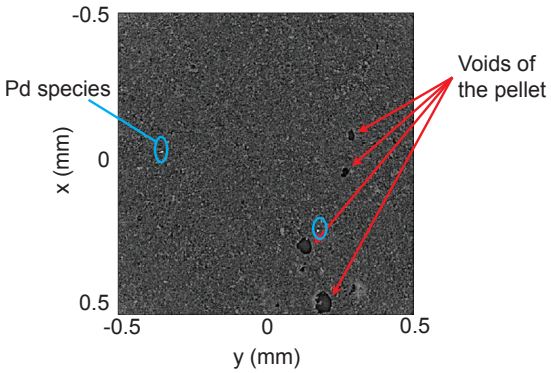

Figure 7.1. Reconstructed image obtained with absorption tomography (local tomography) of a calcined γ-Al_2O_3 pellet containing Na_2PdCl_4 (Pd 1 wt%) and NaCl (1.4 M) with a 1.6 x 1.0 mm beam in 40 s on beamline ID 15 A (ESRF, Grenoble). Dark grey spots show low absorbing elements (voids in alumina structure) and white spots show high absorbing elements (Pd).

Ackowledgments

Marco Di Michiel (ESRF) is kindly thanked for performing the absorption tomography experiments.

References

[1] J.-D. Grunwaldt, B. Kimmerle, A. Baiker, P. Boye, C. G. Schroer, P. Glatzel, C. N. Borca, F. Beckmann, *Catal. Today* **2009**, *145*, 267.

[2] L. Ruffino, R. Mann, R. Oldman, E. H. Stitt, E. Boller, P. Cloetens, M. DiMichiel, J. Merino, *Can. J. Chem. Eng.* **2005**, *83*, 132.

Samenvatting

Onderzoek is uitgevoerd naar de ontwikkeling van spectroscopische technieken voor het karakteriseren van katalysatorlichamen met een afmeting van enkele millimeteers tijdens het afzetten van de actieve component. Het doel daarbij was om plaats- en tijdsafhankelijke te verkrijgen. De bereiding van de katalysatordeeltjes kan worden opgedeeld in drie stappen: impregnatie, drogen en calcinatie. Deze stappen zijn bestudeerd met vier verschillende spectroscopische technieken; 1) UV-Vis-NIR micro-spectroscopie, 2) IR micro-spectroscopie, 3) Magnetic Resonance Imaging (MRI) en 4) Tomographic Energy Dispersive Diffraction Imaging (TEDDI). Deze technieken maken het mogelijk om meer inzicht te verkrijgen in de fysisch-chemische processen die plaats vinden tijdens de bereiding van katalysatoren. De aldus verkregen informatie kan vervolgens worden gebruikt voor de ontwikkeling van nieuweof verbeterde katalysatoren.

De genoemde spectroscopische technieken zijn toegepast bij de bereiding van Ni/γ-Al_2O_3 en Pd/γ-Al_2O_3 hydrogeneringskatalysatoren. De mogelijkheden en beperkingen van deze methodieken voor de karakterisering zijn bestudeerd. Verschillende experimentele condities werden gevarieerd om de rol van metaalionen en het drageroppervlak tijdens de bereiding van de katalysatoren te onderzoeken.

Hoofdstuk 2 en 3 richten zich op de toepassing van UV-Vis-NIR en IR micro-spectroscopie tijdens de impregnatie en de droog- en calcinatie stappen voor de bereiding van Ni/γ-Al_2O_3 en Pd/γ-Al_2O_3 hydrogeneringskatalysatoren. In hoofdstuk 2 is UV-Vis-NIR micro-spectroscopie gebruikt om de vorming en het transport van $[PdCl_4]^{2-}$-ionen binnen de γ-Al_2O_3 pellets vast te stellen. In dit onderzoek werden de pH van de oplossing en de tijd na impregnatie gevarieerd. Tevens is het effect van toevoeging van verschillende hoeveelheden Cl^- (aq) ondergezocht. Met de verkregen resultaten is een protocol ontwikkeld om 0.2 wt % Pd/γ-Al_2O_3 katalysatoren te bereiden met verschillende Pd macro-distributies. Verder kon worden vastgesteld dat de $[PdCl_4]^{2-}$- of $[PdCl_3(H_2O)]^-$- complexen in waterige oplossingen tijdens de impregnatie hydroliseren tot $[PdCl_2(OH)_2]^{2-}$en dat de moleculaire structuur van het complex verandert tot $[PdCl(OH)_3]^{2-}$ of $[Pd(OH)_4]^{2-}$, afhankelijk van de pH van de

oplossing, de evenwichtstijd en de concentratie van de Cl^--ionen. De UV-Vis-NIR micro-spectroscopische studie op de gedroogde katalysatoren wees uit dat de Cl^--ionen tijdens het drogen opnieuw in de eerste coordinatie schil van Pd^{II} komen en dat $[PdCl_4]^{2-}$ en $[PdCl_3(OH)]^{2-}$ worden gevormd. Tijdens de calcinatie is geen herverdeling van Pd waargenomen. Wel is vastgesteld dat nog steeds Cl^--ionen in idrect contact zijn met de Pd-fase. Dit toont het bekende 'vergiftigings' effect van deze ionen op Pd-katalysatoren aan.

Hoofdstuk 3 beschrijft de invloed van ethyleendiamine (*en*) liganden op de moleculaire structuur en het transport van Ni^{2+} tijdens de impregnatie en na het drogen. Deze studie is uitgevoerd met UV-Vis-NIR en IR micro-spectroscopie. De resultaten tonen het complementaire effect aan dat de verschillende hydroxyl groepen op het oppervlak van de alumina drager hebben op de stabiliteit van de Ni^{2+} uitgangscomplexen in de poriën van de drager. Uitwisselingsreacties tussen de water liganden in $[Ni(en)_x(H_2O)_{6-2x}]^{2+}$ (x = 0 – 3) en de hydroxylgroepen op het oppervlak van alumina tijdens impregnatie werden aangetoond. Dit levert een trend op in de sterkte van adsorptie van de verschillende complexen: $[Ni(en)(H_2O)_4]^{2+}$ < $[Ni(en)_2(H_2O)_2]^{2+}$ ~ $[Ni(H_2O)_6]^{2+}$ < $[Ni(en)_3]^{2+}$, waarbij de laatste geen interactie vertoonde met het oppervlak tijdens impregnatie. De studie laat ook zien dat deze interacties verantwoordelijk zijn voor de verdeling van Ni en ethyleendiamine na het drogen. Hoe zwakker de adsorptie van het Ni^{2+} complex, hoe meer "egg-shell" de verdelingen van Ni^{2+} en ethyleendiamine waren. UV-Vis-NIR micro-spectroscopie gaf inzicht in de lokale omgeving van Ni^{2+} en IR micro-spectroscopie liet de macro-distributie van het ethylenediamine ligand zien, beide als functie van de plaats in het extrudaat.

Hoofdstuk 4 en 5 beschrijven het gebruik van twee niet-invasieve methodes voor het karakteriseren van Ni/γ-Al_2O_3 hydrogeneringskatalysatoren tijdens de bereiding. ^{1}H-MRI wordt in Hoofstuk 4 geïntroduceerd als een indirecte karakteriseringsmethode voor de impregnatie van paramagnetische metaalionen, zoals Ni^{2+}. Deze methode is gebaseerd op de invloed van paramagnetische metaalionen op de relaxietijden van protonen. Op deze manier kan het transport van metaalionen binnen dragerlichamen worden gevolgd omdat het contrast in het NMR beeld een directe afspiegeling is van het NMR signaal van waterprotonen. Omdat het NMR signaal afhankelijk is van de relaxatietijden van protonen, en deze afnemen met de aanwezigheid van paramagnetische metaalionen, kan het metaalion worden gelokaliseerd in een katalysatorextrudaat aan de hand van de verschillende

NMR signalen. Er zijn twee contrastbeeld methoden: T_1 en T_2. Met de T_2 methode kan het transport van waterige metaalionen complexen kwantitatief worden gemeten, zoals voor $[Ni(H_2O)_6]^{2+}$ binnen γ-Al_2O_3 extrudaten. De kwantitatieve analyse van het transport van $[Ni(H_2O)_6]^{2+}$ in een γ-Al_2O_3 extrudaat kan vervolgens worden uitgevoerd met behulp van een ijklijn van de NMR signalen binnen de poriën en verschillende concentraties van $[Ni(H_2O)_6]^{2+}$. Echter, voor elk metaalion-drager systeem moet een nieuwe ijklijn worden opgesteld omdat het NMR signaal in de poriën van het dragerlichaam niet alleen afhankelijk is van de concentratie van het paramagnetische metaalion uitgangscomplex. Het signaal hangt tevens af van de onzuiverheden in de impregnatieoplossing en in de drager, en van de textuureigenschappen van de drager (poriegrootte en structuur). De mogelijkheden van MRI om de impregnatiestap van andere systemen te karakteriseren is eveneens bestudeerd. Dit onderzoek is uitgevoerd aan de hand van de impregnatie van $[Ni(\textit{edta}H_x)]^{2-}$ en de co-impregnatie van $[Ni(\textit{edta}H_x)]^{(2-x)-}$ en $[Ni(H_2O)_6]^{2+}$.

De ^{1}H-MRI methode kan ook worden toegepast om het transport van chelaatcomplexen zoals $[Ni(\textit{edta}H_x)]^{(2-x)-}$ te monitoren. Echter, vanwege de grootte van het *edta*-ligand wordt de paramagnetische invloed van de Ni^{2+}-ionen op de relaxatietijden van waterprotonen afgeschermd. Om die reden moet een andere contrastbeeld methode worden gebruikt, namelijk T_1. Deze afbeeldingsmethode geeft eveneens een contrast tussen de gebieden met en zonder Ni^{2+} complexen, maar gebieden met verschillende concentraties van Ni^{2+} kunnen niet worden onderscheiden. Deze methode kan derhalve niet kwantitatief gebruikt worden. De mogelijkheden van de ^{1}H-MRI methode om het transport van co-geimpregneerd $[Ni(\textit{edta}H_x)]^{(2-x)-}$ en $[Ni(H_2O)_6]^{2+}$ te visualiseren is beperkt. In combinatie met UV-Vis-NIR micro-spectroscopie verschaft deze methode echter zeer bruikbare informatie omdat ze samen een semi-kwantitatief inzicht in de lokatie van de twee metaalion-complexen verschaffen. Op deze wijze is aangetoond dat $[Ni(edtaH_x)]^{(2-x)-}$ een "egg-shell" verdeling heeft en $[Ni(H_2O)_6]^{2+}$ een uniforme macro-distributie. Bovendien verschaft de combinatie van technieken inzicht over de adsorptieprocessen die de complexen ondergaan op het alumina-oppervlak en onderling. Op deze wijze zijn elektrostatische interacties tussen de twee complexen aangetoond welke niet gedemonstreerd hadden kunnen worden met één van deze technieken afzonderlijk.

Tenslotte introduceert Hoofdstuk 5 de mogelijkheden van een synchrotron-gebaseerde techniek om katalysatordeeltjes met een afmeting van enkel millimeters

te karakteriseren tijdens de bereiding. Deze methode, TEDDI genaamd, is toegepast voor de in situ karakterisering van de calcinatiestap van Ni/γ-Al_2O_3 pellets. Hiertoe is een reactiecel gebouwd die het mogelijk maakte om energie dispersieve spectra te meten tijdens de calcinatiestap. Twee verschillende systemen zijn onderzocht, [Ni(*en*)$_3$]$(NO_3)_2$ en [Ni(*en*)$(H_2O)_4$]Cl_2 op γ-Al_2O_3 katalysatorlichamen. Daarbij is de calcinatie uitgevoerd in N_2. Deze calcinatiemethode levert metallische Ni-nanodeeltjes op waarvan de grootte afhankelijk is van de Ni:*en* verhouding en het gebruikte Ni^{2+} uitgangszout. Daarbij kon de vorming van nikkel-aluminaten gedeeltelijk worden vermeden. Het doel van deze experimenten was om de ontleding van de uitgangscomplexen en de vorming van de uiteindelijke actieve fase weer te geven in 3D of 4D (*x*, *y*, *z* en/of tijd/temperatuur). Deze techniek geeft fluorescentie en diffractie data, waardoor Ni^{2+} kan worden gelocaliseerd samen met andere mogelijke kristallijne fasen in het katalysatorlichaam. Uit de verkregen resultaten is geconcludeerd dat de calcinatie van [Ni(en)$_3$]$(NO_3)_2$/γ-Al_2O_3 metallische Ni-nanodeeltjes van 5 nanometer oplevert in een egg-shell macro-distributie. Tevens is vastgesteld dat de calcinatie van [Ni(*en*)$(H_2O)_4$]Cl_2/γ-Al_2O_3 een brede deeltjesgrootte verdeling geeft van Ni nanodeeltjes van gemiddeld ongeveer 30 nm met een uniforme macro-distributie.

Appendix A

UV-Vis Micro-spectroscopy Set-up

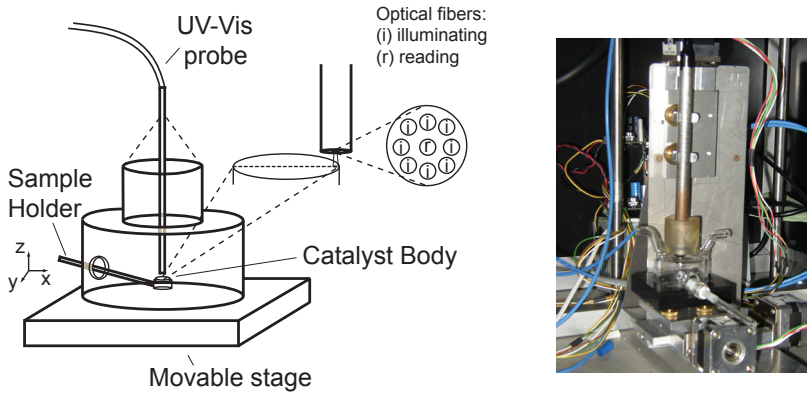

Figure A1. Scheme and photograph of the environmental cell used in UV-Vis-NIR micro-spectroscopy.

Appendix B

UV-Vis Spectroscopic Investigation of the Molecular Structure of Ni^{2+} in Aqueous Solutions in the Presence of *Edta*

1. Niedta1:1 Solutions

Several 1:1 Ni-*edta* complexes have been reported in literature as a function of the pH:[1-6]

1. Acidic pH: $[Ni(edtaH)(H_2O)]^-$ and $[Ni(edtaH_2)(H_2O)]$ with one and two protonated carboxyl groups, respectively.
2. Neutral pH: equilibrium between $[Ni(edta)]^{2-}$ and pentacoordinated $[Ni(edta)(H_2O)]^{2-}$.
3. Basic pH: $[Ni(edta)(OH)]^{3-}$.

In order to determine the Ni-*edta* complexes present in the Ni*edta*1:1pH1 and Ni*edta*1:1pH7 impregnation solutions, two different pH titration experiments were performed, and UV-Vis spectra of all the pH solutions were collected. Multivariate curve resolution (MCR) analysis was then carried out with the UV-Vis spectra measured in order to construct a speciation plot of Ni-*edta* complexes (molar 1:1ratio) as a function of pH.

The first pH titration was conducted by addition of known amounts of 1 M NaOH to a solution containing 0.05 M $Ni(NO_3)_2$ + 0.05 M Na_2edtaH_2 (and 0.7 M $NaNO_3$). The initial pH of the Ni-*edta* solution was 0.5 (acidified by addition of HNO_3). UV-Vis spectra were recorded after each NaOH addition. Figure A2 shows the pH titration curve as a function of the molar OH:Ni ratio. At pH values above the equivalence point, it can be assumed that only the complex $[Ni(edta)(OH)]^{3-}$ is present.

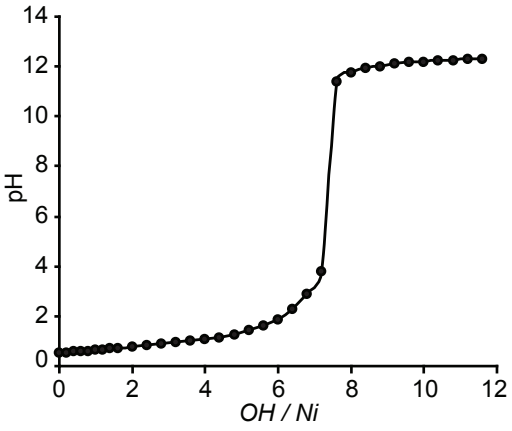

Figure A2. pH titration curve showing the effect of the addition of NaOH to a solution containing 0.05 M $Ni(NO_3)_2$ + 0.05 M Na_2edtaH_2 (and 0.7 M $NaNO_3$) with initial pH 0.5.

Figure A3 shows the UV-Vis spectra collected in the acidic pH range of the first titration curve. The spectra indicated substantial changes in the molecular structure of Ni^{2+}, which were due to the different protonation states of the *edta* ligand. The Ni^{2+} d-d transition band at around 600 nm, depicted in Figure A3, shows an isosbestic point at 689 nm and an increase of the absorption coefficient until pH 1.9. Janjic *et al*.[5] suggested that this isosbestic point corresponded to an equilibrium between di-protonated and mono-protonated Ni-*edta* complexes: $[Ni(edtaH)(H_2O)]^-$ and $[Ni(edtaH_2)(H_2O)]$. From pH 1.9 to pH 3.8, the absorption coefficient is constant but the maximum absorption shifts to shorter wavelengths. In this range of pH values, another isosbestic point is observed at 580 nm (and 685 nm), which has been attributed to the equilibrium between $[Ni(edtaH)(H_2O)]^-$ and $[Ni(edta)]^{2-}$.[5]

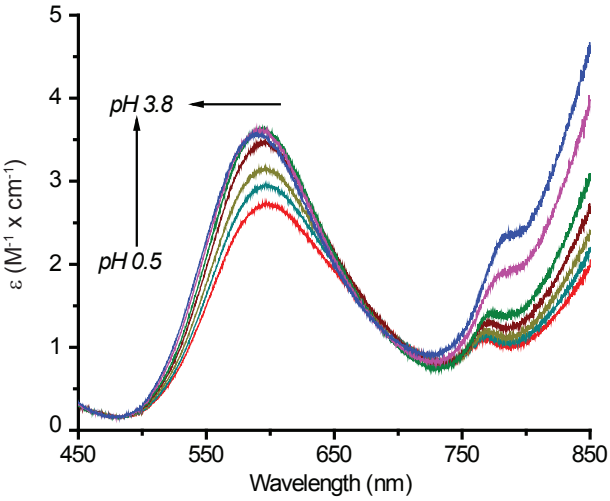

Figure A3. UV-Vis spectra recorded on selected solutions containing $Ni(NO_3)_2$ and Na_2edtaH_2 in the pH range between 0.5 and 3.8.

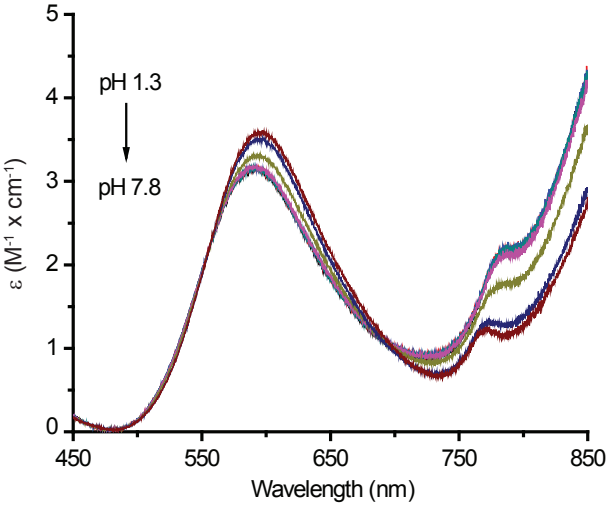

Figure A4. Selected UV-Vis spectra of solutions containing 0.1 M $Ni(NO_3)_2$ and *edta*, in the pH range between 1.3 and 7.8.

The second pH titration was performed by mixing two solutions containing 0.1 M $Ni(NO_3)_2$ + Na_2H_2*edta*, one with pH 1.3 and another with pH 7.8, to pH values between 1.3 and 7.8, in steps of 0.5 pH units. In this experiment, the Ni^{2+} concentration was constant in the whole range of pH. Figure A4 shows selected UV-Vis spectra in this pH range. The absorption coefficient remains constant up to pH 3 and then decreases with increasing the solution pH. An isosbestic point is observed at around 560 nm which indicated the equilibrium between $[Ni(edtaH)(H_2O)]^-$ and $[Ni(edta)]^{2-}$.

Even though the presence of $[Ni(edta)]^{2-}$ and $[Ni(edta)(H_2O)]^{2-}$ in equilibrium at neutral pH has been reported in literature, these two species cannot be distinguished by UV-Vis spectroscopy. The latter will be neglected for this analysis. With the UV-Vis data obtained from the pH-titration experiments, three main Ni-*edta* species were assumed to be present in the Ni*edta*1:1 solutions: $[Ni(edtaH_2)]$, $[Ni(edtaH)]^-$ and $[Ni(edta)]^{2-}$ with increasing pH.

To conduct the MCR analysis of the UV-Vis spectra measured during the two pH titrations, several assumptions were made: the pH region to study was between 0.5 and 8, since the basic region was not interesting for this study; the number of components was based on trial and error, using as little components as possible; and, finally, the non-negativity constraint was applied. Moreover, spectra were first offset corrected and the number of data points was reduced by smoothing. The MCR analysis resulted in three main components, as predicted from the analysis of the isosbestic points in the UV-Vis spectra.

Figure A5 shows the speciation plot of the Ni-*edta* complexes, as a function of pH, derived from the MCR analysis of the UV-Vis spectra measured.

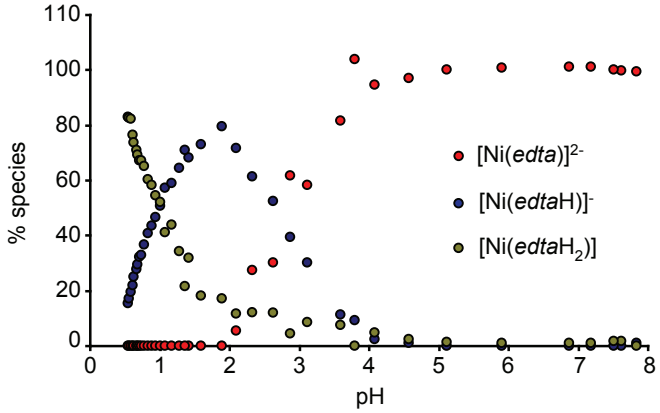

Figure A5. Speciation plot of the Ni-*edta* complexes as a function of the solution pH, derived from an MCR analysis of the UV-Vis spectroscopic data.

2. Niedta6:1 Solutions

Figure A6 shows the UV-Vis spectra of the Ni*edta*6:1 (pH1 and pH6) solutions in the region between 450-850 nm. MCR analysis was used to deconvolute the UV-Vis band in this region. To do so, the UV-Vis spectra obtained for the three main components, namely [Ni(*edta*H_2)], [Ni(*edta*H)]$^-$ and [Ni(*edta*)]$^{2-}$, in the MCR analysis of the Ni*edta*1:1 solutions were considered. Moreover, a fourth component was introduced; i.e. the complex $[Ni(H_2O)_6]^{2+}$. At pH 1, the deconvoluted band showed the presence of 0.50 M $[Ni(H_2O)_6]^{2+}$ (Ni^{2+} d-d doublet at 654 and 720 nm), 0.07 M [Ni(*edta*H)]$^-$ and 0.03 M [Ni(*edta*H_2)] (band at 590 nm). At pH 6, the species present were 0.49 M $[Ni(H_2O)_6]^{2+}$ and 0.11 M [Ni(*edta*)]$^{2-}$. The maximum concentration of [Ni(*edta*)]$^{2-}$complex must be 0.1 M, since this is the concentration used of the *edta* salt. This means that there is an uncertainty in the calculated Ni^{2+} concentration of 10 %.

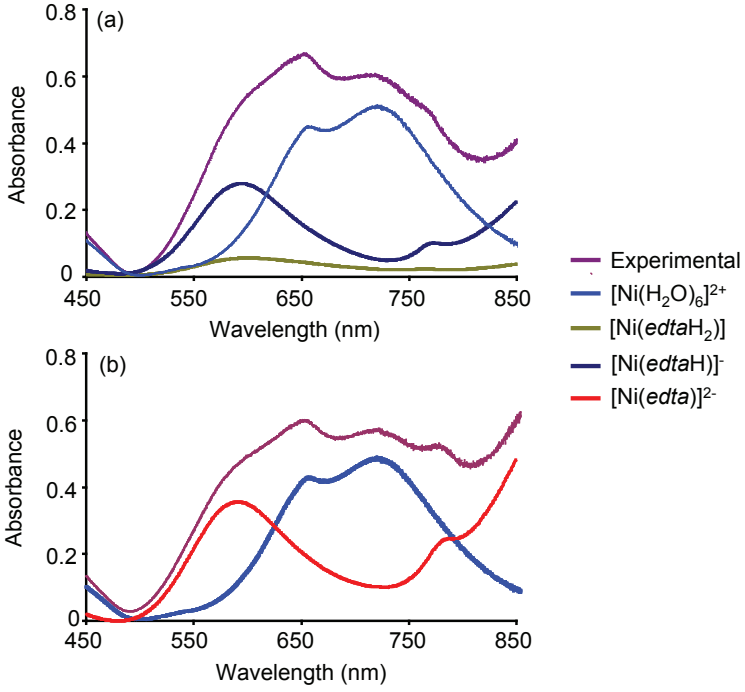

Figure A6. Visible spectra in the range of 450-850 nm of the solutions (a) Ni*edta*6:1pH1, and (b) Ni*edta*6:1pH6. The spectra from the individual components are also shown.

3. References

[1] T. R. Bhat, M. Krishnamurthy, *J. Inorg. Nucl. Chem.* **1963**, *25*, 1147.
[2] A. R. Bowers, C. P. Huang, *J. Colloid Interface Sci.* **1986**, *110*, 575.
[3] A. R. Felmy, O. Qafoku, *J. Solution Chem.* **2004**, *33*, 1161.
[4] M. W. Grant, H. W. Dodgen, J. P. Hunt, *J. Am. Chem. Soc.* **1971**, *93*, 6828.
[5] T. J. Janjic, L. B. Pfendt, V. Popov, *J. Inorg. Nucl. Chem.* **1979**, *41*, 63.
[6] G. S. Smith, J. L. Hoard, *J. Am. Chem. Soc.* **1959**, *81*, 556.

Appendix C

TEDDI Environmental Cell

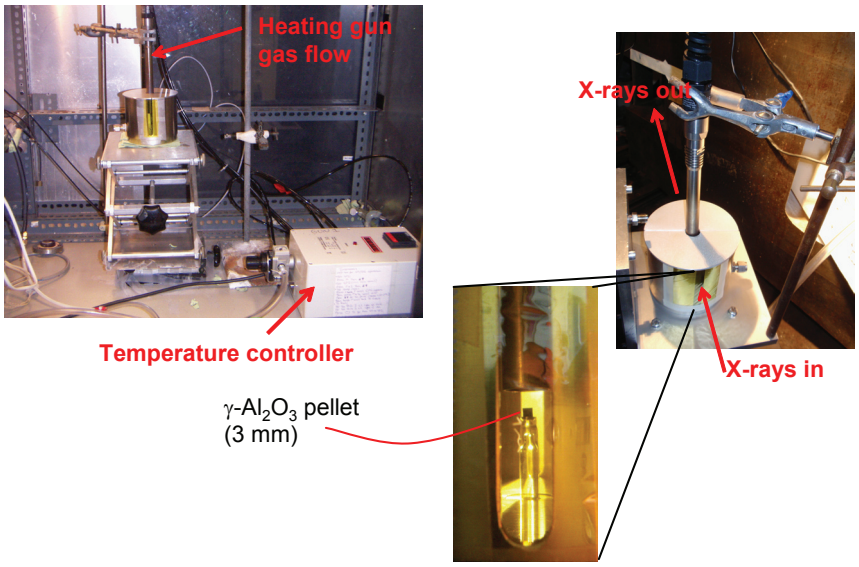

Figure A7. Photographs of the environmental cell used to perform in situ TEDDI experiments.

Corrections of the Scanning Volume

In order to construct 2D maps of the Ni fluorescence or diffraction signals (YT, XY and YZ maps), the spectra obtained had to be corrected for the fraction of lozenge that is within the pellet (scanning volume). To do this correction, two different approaches were used depending on the peak of interest (diffraction or fluorescence).

1. Correction of the Diffraction Data

The diffraction peaks of the Ni phases were corrected by normalization to the area of the (440) reflection of γ-Al_2O_3 (at 73.1 keV). This correction can be done since the scanning volume is equivalent to the amount of support material scanned. In this way, the diffraction peak of interest and the diffraction peak of γ-Al_2O_3 were fitted using gaussian curves (Figures A8b-d), and the area under the diffraction peak of interest was normalized to the area under the diffraction peak at 73.1 keV (reflection (440) of γ-Al_2O_3). As a result of this correction, the TEDDI images were transformed into corrected 2D maps as depicted in Figure A8e. This figure illustrates the correction process followed in the case of an XY map of the [Ni(*en*)$(H_2O)_4$]Cl_2/γ-Al_2O_3 pellet. The same procedure was followed to construct the YZ or the YT maps.

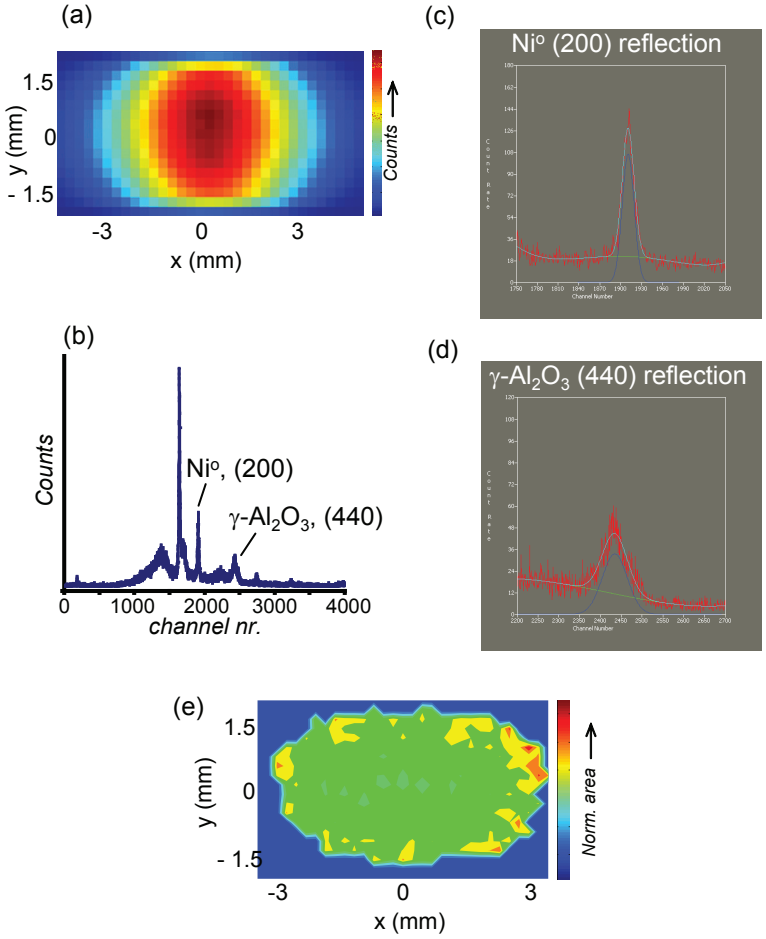

Figure A8. (a) TEDDI image obtained from the XY scanning experiment on $[Ni(en)(H_2O)_4]Cl_2/\gamma\text{-}Al_2O_3$ pellet after calcination at 500 ˚C. (b) Energy spectrum contained in a pixel of the TEDDI image in (a). The diffraction peaks of metallic Ni at 58.0 keV and of $\gamma\text{-}Al_2O_3$ at 73.1 keV are indicated. (c) and (d) are the fitted peaks at 58.0 (Ni^o) and 73.1 keV($\gamma\text{-}Al_2O_3$), respectively. Peak fitting was performed using EasyEDD software. (a) XY map of the metallic Ni peak after normalization to the diffraction line of $\gamma\text{-}Al_2O_3$. A rather uniform macro-distribution of Ni was obtained.

2. Correction of the Fluorescence Data

The fluorescence data, however, could not be corrected by making use of the diffraction line at 73.1 keV of γ-Al_2O_3, since the latter is affected by temperature whilst the fluorescence signal is not. Moreover, the fluorescence signal is not only dependent on the amount of scanning volume within the pellet, but it is also dependent on the mass attenuation coefficient; i.e., on the mass thickness and density of the sample (ignoring self-(re)absorption based on the assumption that the amount of Ni present in the sample is much less than the amount of alumina). Therefore, to get reliable fluorescence information, the X-ray fluorescence data should be corrected for the fraction of scanning volume within the pellet and also for the thickness of the sample. The loss of fluorescence signal due to the attenuation from the sample thickness can clearly be visualized in Figure A9.

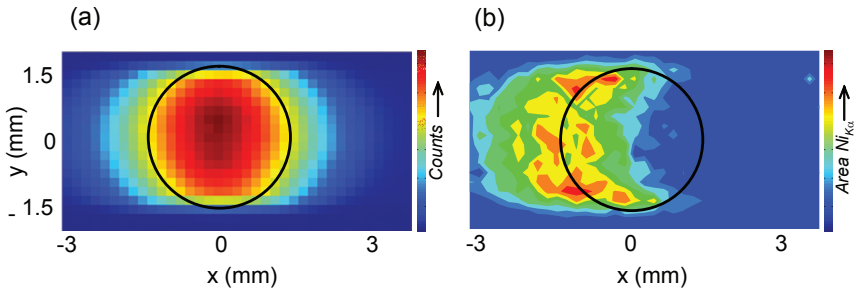

Figure A9. (a) TEDDI image obtained from the XY scanning experiment on [Ni(*en*)$(H_2O)_4$]Cl_2/γ-Al_2O_3 pellet at 25°C. (b) XY map of the fluorescence at 7.5 keV ($Ni_{Kα}$) without correction. The black circumference represents the pellet.

This figure illustrates an XY TEDDI image collected on the [Ni(*en*)$(H_2O)_4$]Cl_2/γ-Al_2O_3 pellet at 25 °C, and the XY map constructed from the fitting of the fluorescence peak of Ni at 7.5 keV, without correction for the scanning volume. The XY fluorescence map shows the center of the pellet in red color; i.e., more intense fluorescence is detected in these areas compared to the outer rim. The higher signal in the core of the pellet is, as explained above, due to the larger scanning volume on the sample which is bigger in the core than at the edges, as explained in Chapter 5 (Figure 5.3). Furthermore, the signal detected outside the pellet (green to orange regions on the left side of the black circumference in Figure A9b) is, as explained

previously, an effect of the fraction of scanning volume (or lozenge) that is within the pellets when the pellet is already outside the center of this scanning volume. In addition to this, the XY maps constructed from the fluorescence signal show hardly any signal from the right side of the pellet (blue area inside the black circumference). Thus, the XY map looks like a half moon, the lost signal comes from the part of the pellet opposite to the detector; namely, the emitted X-rays in that positions are lost on their way to reach the detector due to mass attenuation.

2.1. Method Developed to Correct the Fluorescence Data

The method to correct the fluorescence signal was developed for the Y scan-line experiments (YT maps). Still, the same principle is applicable to correct the XY and YZ maps. In order to correct the fluorescence data, the amount of scanning volume on the pellet as a function of the y position was calculated, as illustrated in Figure A10c. To correct for the attenuation of the signal due to the material thickness, it was assumed that the outgoing X-rays should travel a distance x labeled as "d. to detector" which corresponded to the distance between the furthest point from the detector of the scanning volume and the edge of the pellet close to the detector, as represented in Figure A10a. These two parameters; namely, d. to detector and scanning volume on the sample, were calculated taking into account the shape of the pellet (cylinder), the shape of the scanning volume (lozenge), and the angle at which the detector was located with respect to the X-ray beam (Figures A10a and b).

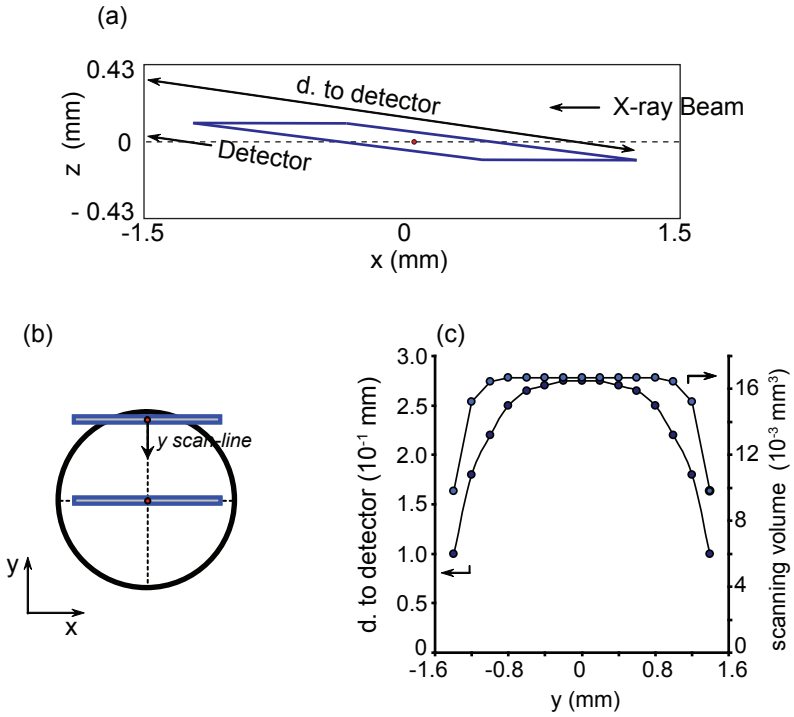

Figure A10. (a) Front view of an XZ slice of a pellet with the scanning volume depicted in the center (*x* = *z* = 0 mm). The scanning volume is represented as the blue diamond-like shape with the red dot indicating its center. The distance that the outgoing X-rays should travel through is also indicated as "d. to the detector"; (b) top view of a pellet and the scanning volume as a function of the *y* position. (c) d. to detector and amount of scanning volume on the pellet as a function of the *y* position.

A correction factor, C_T, was calculated for each *y* position on the pellet, which took into account both the amount of scanning volume within the pellet, $C_{s.v.}$, and the attenuation coefficient, $C_{a.c.}$, as $C_T = C_{s.v.} \times C_{a.c.}$. The values of the correction factors $C_{s.v.}$, $C_{a.c.}$ and C_T as a function of the *y* position within the pellet are illustrated in Figure A11a. $C_{s.v.}$ was determined form the variation of the amount of scanning volume on the pellet as a function of the *y* position (Figure A10c). To determine it, it was taken into account that the scanning volume, 0.0167 mm^3, at the core of the pellet is completely on the pellet, as depicted in Figure A10b. The scanning volumes in each *y* position were, then, normalized to this value. To calculate $C_{a.c.}$, it was assumed that

at the edges of the pellet, where the d. to the detector was the minimum; i.e. 0.1 mm, as illustrated in Figure A10c, this distance was equivalent to 100 % transmission (0 % attenuation). Then, the d. to the detector for each *y* position was normalized to this value. Finally, C_T was calculated as $C_T = C_{s.v.} \times C_{a.c}$ for each *y* position.

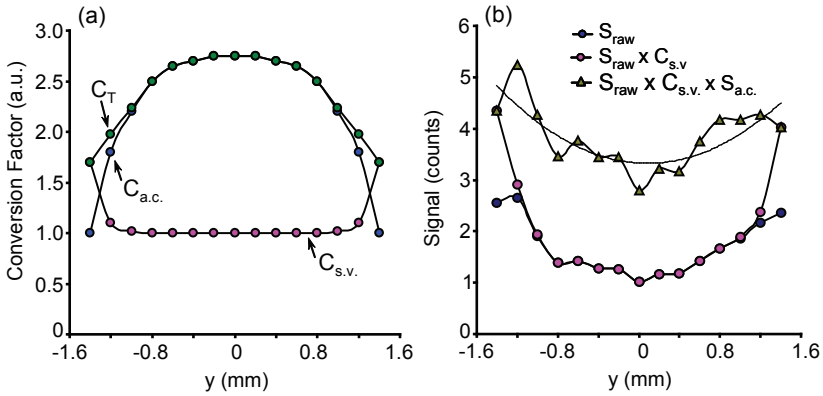

Figure A11. (a) Correction factors $C_{s.v.}$, $C_{a.c.}$ and C_T as a function of the *y* position within the pellet; (b) Raw fluorescence signal (S_{raw}) at 7.5 keV of Ni ($Ni_{K\alpha}$) of the $[Ni(en)_3](NO_3)_2/\gamma\text{-}Al_2O_3$ pellet at 500ºC as a function the *y* position (*x* = 0 mm); and after applying the correction factors $C_{s.v.}$ (S_{raw} x $C_{s.v.}$) and C_T (S_{raw} x $C_{s.v.}$ x $C_{a.c.}$).

Once the correction factor (C_T) as a function of the *y* position was determined (Figure A11a), the raw fluorescence signal of Ni at 7.5 keV ($Ni_{K\alpha}$) in the YT experiments was corrected. The 2D maps of the fluorescence signal as a function of T and *y* position presented in Chapter 5 were constructed in this way. Figure A11b illustrates the procedure applied. This figure shows the raw fluorescence signal at 7.5 keV (area under the fitted curve) as a function of the *y* position (S_{raw}) when *x* = 0 mm. The signal is the strongest at the edge because the distance to the detector (d. to detector) is the shortest, as depicted in Figure A10c. Moreover, at the edge, the scanning volume on the sample is also the smallest. Firstly, if S_{raw} is corrected for the scanning volume ($C_{s.v.}$), the signal remains the same in the core of the pellet whilst it became stronger at the edges (S_{raw} x $C_{s.v.}$ in Figure A11b). If the correction factor for the attenuation coefficient is applied, the values S_{raw} x $C_{s.v.}$ x $C_{a.c.}$ are obtained. This signal represents the signal that would be measured assuming that there would be no attenuation due to the mass thickness. The raw signal profile as a function of *y* position suggested a false Ni egg-shell distribution. Yet, after applying this correction factor C_T a less

sharp Ni egg-shell distribution is obtained, which is in agreement with the optical micrograph of the pellet (Figure 5.6 in Chapter 5).

Appendix D

Table of Contents Illustrations

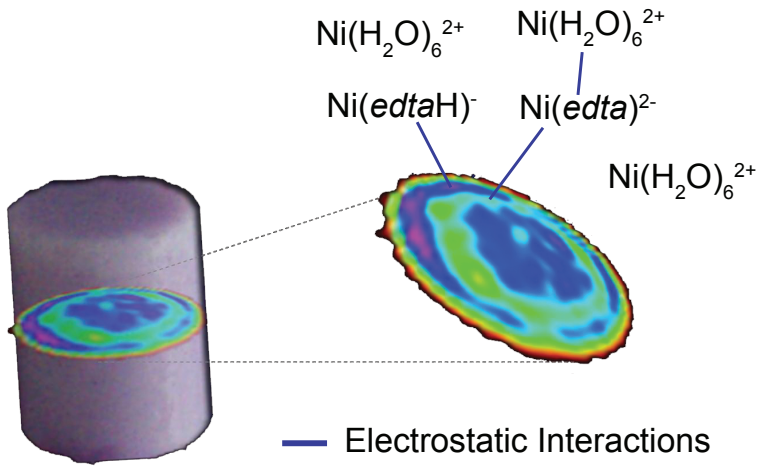

Figure A12. TOC illustration from L. Espinosa-Alonso, A. A. Lysova, P. de Peinder, K. P. de Jong, I. V. Koptyug, B. M. Weckhuysen, *Magnetic Resonance Imaging Studies on Catalyst Impregnation Processes: Discriminating Metal Ion Complexes within Millimeter-Sized γ-Al_2O_3 Catalyst Bodies*, J. Am. Chem. Soc. **2009**, *131*, 6525-6234.

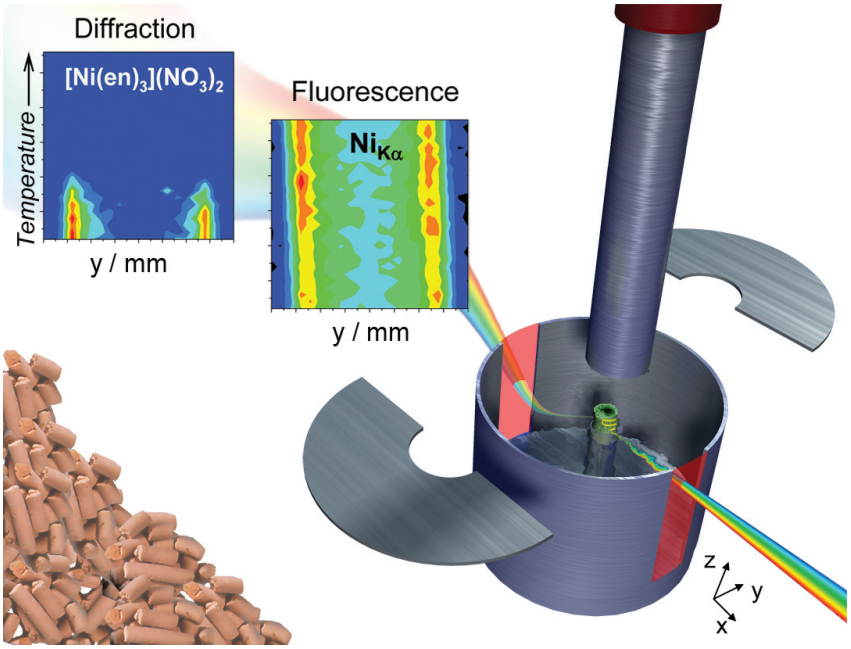

Figure A13. TOC illustration from L. Espinosa-Alonso, M. G. O'Brien, S. D. M. Jacques, A. M. Beale, K. P. de Jong, P. Barnes, B. M. Weckhuysen, *Tomographic Energy Dispersive Diffraction Imaging to Study the Genesis of Ni Nanoparticles in 3D within γ-Al_2O_3 Catalyst Bodies*, J. Am. Chem. Soc. **2009**, *submitted*.

List of Publications

MRI as an Emerging Tool for Studying the Preparation of Supported Catalysts
A.A. Lysova, J.A. Bergwerff, L. Espinosa-Alonso, B.M. Weckhuysen and I.V. Koptyug, Appl. Catal. A: General ***2009****, submitted*.

Tomographic Energy Dispersive Diffraction Imaging to Study the Genesis of Ni Nanoparticles in 3D within γ-Al_2O_3 Catalyst Bodies
L. Espinosa-Alonso, M. G. O'Brien, S. D. M. Jacques, A. M. Beale, K. P. de Jong, P. Barnes and B. M. Weckhuysen, J. Am. Chem. Soc. ***2009****, submitted .*

A UV-Vis Micro-spectroscopic Study to Rationalize the Influence of Cl^- (aq) on the Formation of Different Pd Macro-Distributions on γ-Al_2O_3 Catalyst Bodies
L. Espinosa-Alonso, K. P. de Jong and B. M. Weckhuysen, Phys. Chem. Chem. Phys. ***2009****,* doi: 10.1039/B915753K.

Magnetic Resonance Imaging Studies on Catalyst Impregnation Processes: Discriminating Metal Ion Complexes within mm-sized g-Al2O3 Catalyst Bodies
L. Espinosa-Alonso, A. A. Lysova, P. de Peinder, K. P. de Jong, I. V. Koptyug and B. M. Weckhuysen, J. Am. Chem. Soc. ***2009****, 131,* 6525.

Effect of the Nickel Precursor on the Impregnation and Drying of γ-Al_2O_3 Catalyst Bodies: A UV−Vis and IR Microspectroscopic Study
L. Espinosa-Alonso, K. P. de Jong and B. M. Weckhuysen, J. Phys. Chem. C ***2008****, 112,* 7201.

Monitoring Transport Phenomena of Paramagnetic Metal-Ion Complexes inside Catalyst Bodies with Magnetic Resonance Imaging
J. A. Bergwerff, A. A. Lysova, L. Espinosa Alonso, I. V. Koptyug and B. M. Weckhuysen, Chem. Eur. J. ***2008****, 14,* 2363.

Probing the Transport of Paramagnetic Complexes inside Catalyst Bodies in a Quantitative Manner by Magnetic Resonance Imaging
J. A. Bergwerff, A. A. Lysova, L. Espinosa Alonso, I. V. Koptyug and B. M. Weckhuysen, Angew. Chem. Int. Ed. ***2007****, 46,* 7224*.*

Oral Communications

Magnetic Resonance Imaging to Study Impregnation Processes on γ-Al_2O_3 Support Bodies
L. Espinosa-Alonso, A. A. Lysova, K. P. de Jong, I. V. Koptyug, B. M. Weckhuysen – 21st North American Meeting – June 2009 – San Francisco, USA

Spatially Resolved UV-Vis Micro-spectroscopy: A Physicochemical Study on the Preparation of Metal-ion Supported Catalysts
L. Espinosa Alonso, K. P. de Jong, B. M. Weckhuysen –Europacat VIII – August 2007 – Turku, Finland

Spatially Resolved UV-Vis Micro-spectroscopy: A Physicochemical Study on the Preparation of Metal-ion Supported Catalysts
L. Espinosa Alonso, K. P. de Jong, B. M. Weckhuysen – 20th North American Meeting – June 2007 – Houston, USA

Spatially Resolved Micro-spectroscopy: Gaining Physicochemical Insight in Hydrogenation Catalyst Preparation
L. Espinosa Alonso, K. P. de Jong, B. M. Weckhuysen – VIIIth Netherlands Catalysis and Chemistry Conference – March 2007 – Noordwijkerhout, The Netherlands

Posters

Tomographic Energy Dispersive Diffraction Imaging to Profile in situ the Calcination of Ni/g-Al_2O_3 Catalyst Bodies
L. Espinosa-Alonso, M. G. O'Brien, S. D. M. Jacques, A. M. Beale, K. P. de Jong, P. Barnes, B. M. Weckhuysen – EuropaCat IX – September 2009 – Salamanca, Spain

Magnetic Resonance Imaging to Study Impregnation Processes on γ-Al_2O_3 Support Bodies

L. Espinosa-Alonso, A .A. Lysova, K. P. de Jong, I. V. Koptyug, B. M. Weckhuysen - VIIIth Netherlands Catalysis and Chemistry Conference – March 2009 – Noordwijkerhout, The Netherlands

Spatially Resolved UV-Vis Micro-spectroscopy to Study the Preparation of Metal-ion Supported Catalysts

L. Espinosa Alonso, K. P. de Jong, B. M. Weckhuysen – III International Conference CATALYSIS: FUNDAMENTALS AND APPLICATION – July 2007- Novosibirsk, Russia

MRI as a Noninvasive Technique to Study the Preparation of Supported Catalyst Bodies

J. A. Bergwerff, A. A. Lysova, L. Espinosa Alonso, I. V. Koptyug, B. M. Weckhuysen - 20th North American Meeting – June 2007 – Houston, USA

Acknowledgments

I think the first people that made me decide to do a PhD were Virginie Bellière and Alwies van der Heijden, my supervisors during my Master's internship in this group. With you I had my first initiation in scientific research and the things related: data analysis and discussions, preparing presentations, writing reports... I really enjoyed my time working with you, and I definitely have to thank you because without your support I probably wouldn't have chosen to stay in the Netherlands as a PhD student.

The next people I have to thank are my promotors Bert Weckhuysen and Krijn de Jong. First of all, I have to thank you for trusting in me and giving me the opportunity to work with you. It has been a pleasure working under your supervision, and I am also very grateful that every time I needed to discuss about something or I had any doubts, you both were always there to help me.

I would also like to thank the people I met abroad during this time. Going to Novosibirsk to work with Igor Koptyug and Anna Lysova has been a very nice experience. Also my trips to the Synchrotron where I met Simon Jacques, Paul Barnes and Marco Di Michiel were very intense but also very fruitful.

Matto, Ana and Andy you three have being rather close to me and my project. During the time as a PhD student, I knew that every time I had a problem I could come to you and you would be there to help me. We also had very good times together at the synchrotron where I learned a lot: how to work 18 h a day for several days in a row, how to deal with you without sleeping … and other more interesting things such as playing cricket or golf. Thanks for your help and good times!

Johan and Philipp, my officemates, what can I say… thank you for supporting me and thank me for supporting you!

Marianne! My conference partner! I wish you good luck and hope everything goes very well!

Thanks also to Jaap and Gerbrand, previous PhD students. Gerbrand, thanks for your help the first months as a PhD student and, Jaap, thanks for the good times in Novosibirsk. With you two I learned a lot as a researcher and I think we also had

very good moments together.

Of course, there have been more people involved in this project. Maybe not directly involved in the research but involved in my personal life. I guess that all the foreigners in the group have realized that it is sometimes difficult to be so far away from your family and friends. Only if you are happy in your personal life, which can only happen if you have good people around you, then you will feel comfortable and confident about your professional life. This was definitely my case, and it has only been possible thanks to you guys Heiner, Lukasz, Philipp, Ana, Andy, Matto, Nadia… and to the old and new PhD and post-doc generation.

I definitely have to acknowledge all the permanent staff for their support and help. Thanks Tom for your advices and your help, especially with the blue envelopes. I also should thank Fouad for that Latin roots that make him smile 24/7, and Ad^{M} for keeping me up-to-date with Spanish gossips. Monique and Dymph, thanks for helping me with all the administrative issues.

Finally, these last paragraphs go to my family and friends. Papá, mamá y Chiki, muchas gracias por el apoyo que me habéis dado desde siempre. Papá y mamá, habéis hecho de mi una persona independiente y luchadora, sin esto hubiese sido muy difícil estar aquí. A ti Chiki también muchas gracias por preocuparte por mi. A toda la family: Muchísimas gracias por vuestro apoyo y vuestra fuerza. Os deseo lo mejor!

Marta, Helen, Eva, Luci, Marina y Gema! Espero que os vaya todo genial. Gracias por acordaros de mi de vez en cuando y por nuestros pequeños pero intensos momentos y conversaciones cuando nos vemos!.

As últimas palabras são para meu amorzinho. Muito obrigado por estares comigo sempre, pelo teu sorriso e pelo teu apoio. Desejo-te tudo de bom para acabares o doutoramento... e já sabes ainda faltam 200 anos! Um beijão muito grande para ti! Amo-te!

Leti

Curriculum Vitae

I was born in León (Spain) on November 3rd, 1981. In September 2005 I graduated in Chemistry (equivalent to a MSc degree) at the Universidad Complutense de Madrid with the specialty in Material Sciences. During my last year of studies I performed a 10-month research internship at Utrecht University thanks to the Erasmus Programme. The project, under supervision of Prof. Bert Weckhuysen, was entitled: "Destructive adsorption of chlorinated hydrocarbons on lanthanum-oxide based materials". In October 2005, Prof. Bert Weckhuysen and Prof. Krijn de Jong offered me the chance to start as a PhD student under their supervision. The PhD project, which is described in this thesis, was financed by ACTS/ASPECT and gave me the opportunity to work in an academic atmosphere in close contact with the chemical industry. The results obtained during my PhD have been published in relevant international journals.